Study of Cross-Polarization Scattering Diagnostics for Internal Magnetic Fluctuation Measurement

Doctoral Program in Engineering
University of Tsukuba

March, 2001

Yuichiro KOGI

Abstract

A cross-polarization scattering (CPS) diagnostic method was applied to the GAMMA10 tandem mirror in order to develop a measurement system diagnosing internal magnetic fluctuations. In the CPS process, an incident-electromagnetic wave in ordinary mode is converted to an extraordinary-mode wave by the magnetic fluctuations in a plasma. In the same way, an incident-electromagnetic wave in extraordinary mode is converted to an ordinary-mode wave by the magnetic fluctuations in the plasma.

We have applied the CPS measurement utilizing homodyne system along with a reflectometer to the central-cell plasma. We found that the frequency spectrum of the CPS signal is broader than that of the reflectometer signal. This phenomenon is considered to be observed due to the wave-number matching condition in the CPS process.

Then we have applied the homodyne-CPS measurement utilizing movable receivers in order to observe the dispersion relation of the magnetic fluctuations. From theoretical analysis of the CPS process, it is expected that an observed wave number relates to a scattering angle. As a result, we found that the frequency spectrum broadens with an increase in the scattering angle. This is also considered to be due to the satisfaction of the wave-number matching condition in the CPS process, and we obtained the relation between the wave number and the frequency of the fluctuation, i.e., dispersion relation of the fluctuation, from geometrical analysis of the scattering angle. This fluctuation is considered to be electromagnetic drift-wave Doppler shifted by $\boldsymbol{E} \times \boldsymbol{B}$ rotation velocity.

Next, the CPS system with an ultrashort-pulse microwave as a source has been applied to the central-cell plasma. Since the pulse height of the scattered wave is expected to be proportional to the level of the magnetic fluctuation, this system has an advantage of

measuring the absolute level of the magnetic fluctuations.

In order to relate the pulse-height of the scattered wave to the level of the magnetic fluctuation numerically, we have applied numerical simulation of the electromagnetic propagation including the CPS process with the frequency-dependent finite-difference time-domain ($(FD)^2TD$) method. And we have confirmed that the pulse-height of the scattered wave was accurately proportional to the level of the magnetic fluctuation. Moreover, we have obtained the numerical relation between these values.

In the experiment, we confirmed that the CPS signal can be observed when the 10 or 11 GHz impulse is injected into the plasma, since these impulses, which is mode-converted by the magnetic fluctuations, can pass through the plasma. From the deviation of the pulse height of the received impulse, the averaged fluctuation amplitude is estimated to be 0.016% by comparing with the simulation results.

Consequently, we confirmed that the mode-converted scattered wave is observed properly , and the magnetic fluctuation can be measured with these systems.

Contents

Chapter 1

Introduction

Thermonuclear fusion is considered to be an eternal energy-source instead of fossil fuels. Mass of deuterium (D) contained in the sea water amounts to 4×10^{16} kg, and it corresponds to energy of 10^{22} GJ by the deuterium-tritium fusion reaction. In order to achieve the thermonuclear reactor, high value of the triple product of plasma temperature, density and confinement time is needed. Recently, the break-even condition has been attained by tokamak plasmas, that is, total output power by the fusion reaction is equal to plasma-heating power.

Systems for confinement of high energy plasmas are mainly categorized into two types of experimental devices as shown in Fig. 1. One type of the systems is an inertia confinement system. In this system, isotropic injection of high-energy lasers or particle beams induces implosion of a fuel-pellet. High density and pressure plasma is sustained by ablation of the outer region of the pellet, however, steady state operation is difficult for this system. Another type is a system which uses an external magnetic field, and charged particles are confined by the magnetic field. This magnetic confinement system is further categorized into a torus and an open-ended system according to magnetic configuration of the system. GAMMA10 belongs to the open-ended system. This system has several advantages, that is, it can achieve high-beta plasma, steady state operation, and is simple geometry. However, the improvement of axial confinement, which is a main problem of the open-ended system, is important since the plasma dropped into the loss-cone region can run away along the magnetic

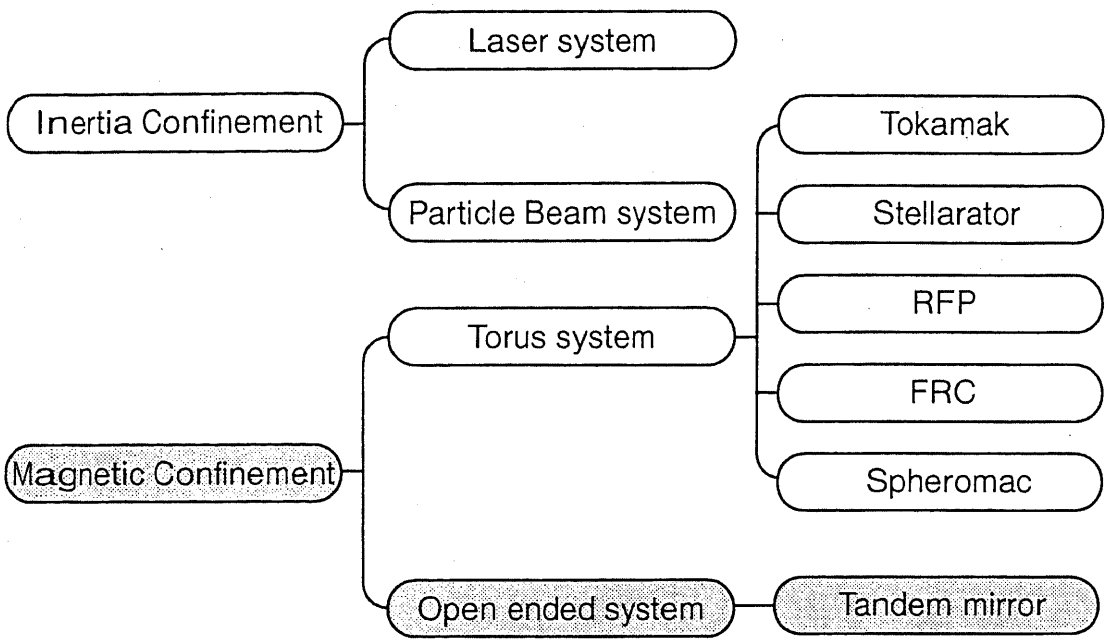

Figure 1.1 Various experimental devices for fusion experiment

field line. In 1976, an idea of tandem mirror was proposed [1,2], and the problem has been broken through. The principle of the tandem mirror is based on the improvement of the axial confinement by formation of confining potentials in addition to the magnetic confinement. In GAMMA10, the formation of the confining potentials and the improvement of the axial confinement are confirmed, although the mechanism of confining potential formation has been studied by theoretical and experimental approaches [3], the distribution of the ion confining potential (plug potential) has not been clearly understood yet. Then radial transports across the magnetic field line have become a next topic of diffusion.

The radial diffusion across the magnetic field line depends on the collisional effect of charged particles, i.e., the charged particles can diffuse across the magnetic field due to collisions between electrons and ions. In an axisymmetric magnetic-field configuration, the step size of the diffusion is Lamor radius of the electron, which is too small compared to the minor radius of the plasma. This is called classical diffu-

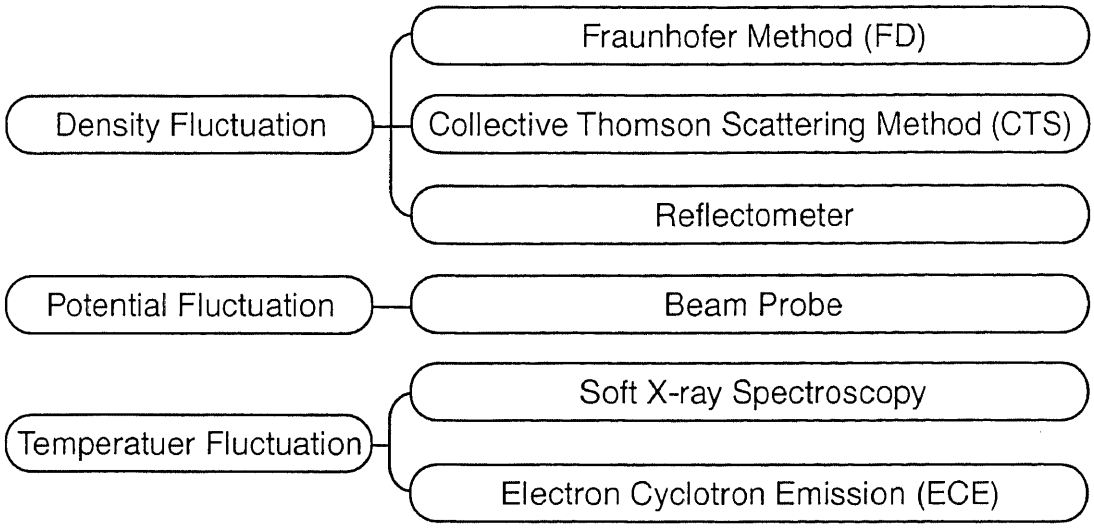

Figure 1.2 Systems for measure various fluctuations

sion. In a non-axisymmetric magnetic-field configuration, such that minimum-B field, torus system and so on, the ions drift radially due to grad-B drift at the geodesic curvature of the magnetic field [4-6]. That is, orbits of the ions are distored elliptically. In this case, the step size of the diffusion is defined as difference of the semimajor axis and the semiminor axis of the elliptical orbit. This is called neoclassical (resonant) diffusion, which diffusivity is extremely larger than that of the classical diffusion.

While, several instabilities of plasma parameters, such as density, temperature, magnetic field, and potential, also play a critical role in radial transport [7]. In the case that amplitude of the instabilities across the magnetic field line increase, the charged particles are fluctuated by the instabilities, and they can diffuse radially. The step size of the diffusion is defined as amplitude of the fluctuations.

So, many types of diagnostic systems have been developed in order to measure and stabilize several types of fluctuations as shown in Fig 1.2. However, direct measurement of magnetic fluctuation in core plasmas still remains a major issue in plasma

diagnostics. Recently, a new technique to measure the internal magnetic fluctuations was proposed. This technique called cross-polarization scattering (CPS) method is based on the mode conversion effect of incident electromagnetic wave by magnetic fluctuations. The purpose of this study is the development and verification of measurement system for the magnetic fluctuations with the CPS method.

In this chapter, a brief history of the CPS diagnostics is described in Sec. 1-1, and the organization of the thesis is presented in Sec. 1-2.

1-1 Magnetic Fluctuation Measurement

The magnetic fluctuations are at present measured only at the edge by magnetic coils. It is important to measure the magnetic fluctuations in the core plasma without perturbing plasma. The CPS has been intensively investigated by different researchers [8-10]. The principle of this diagnostics is based on the polarization change of the electromagnetic wave scattered by magnetic fluctuations.

Experimentally, the CPS experiment was performed by X. L. Zou *et al.* in the Tore Supra tokamak in 1993 [11]. His group confirmed the CPS process in the range of several-hundred kHz-fluctuations by comparing with the data obtained by conventional collective Thomson scattering (CTS). The member of GAMMA10 group also applied the CPS measurement in 1994, and confirmed the CPS process in the ion cyclotron range of frequencies by comparing with the data of reflectometry [12]. In 1996, the author successfully applied the CPS to the low-frequency region with the frequency of less than 200 kHz [13].

The simulation works relates to the CPS as well as CTS and reflectometry have been performed by many researchers with full wave equations in 1-D or 2-D model [14, 15]. The trajectory of incident and scattered waves, and scattering cross-section

by the magnetic fluctuations were calculated.

1-2 Organization of the Thesis

In the chapter 2, we will describe principles of the CPS. The propagation way of modes in a dielectric medium will be presented briefly. In the following section, an induced current and an electric field of the scattered wave by the magnetic-field and the density fluctuations will be derived numerically. These derivations introduce principles of the CPS and the CTS measurements, and the relations between magnetic fluctuations and the CPS will be clarified. Addition to that, temporal and spatial resolution of several diagnostics will be described along with comparison with other diagnostic systems for density fluctuations.

In the chapter 3, the GAMMA10 device along with heating systems and diagnostics for the measurement of basic plasma parameters will be presented. Then, the fluctuations excited in the GAMMA10 plasma will be introduced numerically.

The chapter 4 describes at first experimental setups with a continuous-wave system. Homodyne systems for the CPS and the reflectometer measurement are applied in order to confirm the CPS process. Addition to that, movable receivers with the homodyne system will be presented in the following section. It is applied in order to obtain the dispersion relation of the fluctuation.

In the chapter 5, simulations and experiment with an ultrashort-pulse system will be described. First of all, the simulation model of frequency dependent finite difference time domain ($(FD)^2TD$) method, which is a simulation method for calculations of electromagnetic fields in an anisotropic and dispersive medium, will be presented. Then the simulation results and discussions will be described in the following section. In the discussion, relations between magnetic fluctuations and scattered

wave in various plasma parameters will be clarified. After the section of the simulation, the CPS measurement system with ultrashort-pulse microwaves will be described. And the absolute value of the magnetic fluctuations estimated by the measurement will be discussed.

In chapter 6, the results of the thesis research will be summarized.

In the appendix, we will present details of the derivation of the $(FD)^2TD$ method.

Chapter 2

Principles of Cross-Polarization Scattering

It is considered that plasma fluctuations play an important role to anomalous transport in magnetically confined plasmas. In order to improve the performance of the confinement systems, it is necessary to identify the type of the fluctuation, i.e., potential, magnetic field, density, and temperature, and clarify the relations between these fluctuations and the anomalous transport of the plasma. Several types of probes are used to measure these fluctuations in low density and temperature plasmas, however, these are restricted into the edge of the plasma in high density and temperature device such as GAMMA10. Thus, an unperturbing diagnostic method is essential to measure the fluctuations in the core region. The diagnostics using an electromagnetic wave and a heavy ion beam have been developed and improved since early in the 1980s.

In this chapter, we will describe the propagation of the electromagnetic wave in the dielectric medium in the Sec. 2-1, and the process of the cross-polarization scattering in the Sec. 2-2. And in the Sec. 2-3, the comparison with other diagnostics using electromagnetic waves is described.

2-1 Propagation of Electromagnetic Waves in a Magnetized Plasma [16, 17]

Maxwell's equations and constitutive equations in a magnetized plasma are

$$\nabla \times \boldsymbol{E} = -\frac{\partial \boldsymbol{B}}{\partial t} \tag{2.1}$$

$$\nabla \times \boldsymbol{H} = \frac{\partial \boldsymbol{D}}{\partial t} + \boldsymbol{J} \tag{2.2}$$

$$\boldsymbol{B} = \mu_0 \boldsymbol{H} \tag{2.3}$$

$$\boldsymbol{D} = \varepsilon_0 \boldsymbol{E} \tag{2.4}$$

$$\boldsymbol{J} = \hat{\sigma} \boldsymbol{E} \tag{2.5}$$

where, $\boldsymbol{E}$ and $\boldsymbol{B}$ are the electric field and magnetic field respectively, $\boldsymbol{J}$ is the induced current density, ε_0 and μ_0 are the dielectric constant and magnetic permeability respectively, and $\hat{\sigma}$ is the conductivity tensor. In order to eliminate $\boldsymbol{B}$, Eqs. (2.2) - (2.5) are substituted into Eq. (2.1), then homogeneous plasma wave equation is obtained as

$$\nabla \times (\nabla \times \boldsymbol{E}) + \frac{\partial}{\partial t}\left(\mu_0 \hat{\sigma} \boldsymbol{E} + \varepsilon_0 \mu_0 \frac{\partial \boldsymbol{E}}{\partial t} \right) = 0. \tag{2.6}$$

Using quasi-linear approximation, which technique replaces $\nabla \times$ and $\partial/\partial t$ with $j\boldsymbol{k}$ and $-j\omega$ respectively, Eq. (2.6) is written by

$$\boldsymbol{k} \times (\boldsymbol{k} \times \boldsymbol{E}) + \frac{\omega^2}{c^2} \hat{\varepsilon} \cdot \boldsymbol{E} = 0 \tag{2.7}$$

where, $\boldsymbol{k}$ and ω are the wave vector and angular frequency respectively, and $\hat{\varepsilon}$ is the complex dielectric constant indicated as follows.

$$\hat{\varepsilon} = 1 + \frac{\hat{\sigma}}{j\omega\varepsilon_0} = \begin{bmatrix} 1 - \dfrac{\omega_{pe}^2}{\omega^2 - \omega_{ce}^2} & -j\dfrac{\omega_{pe}^2\omega_{ce}}{\omega\left(\omega^2 - \omega_{ce}^2\right)} & 0 \\ j\dfrac{\omega_{pe}^2\omega_{ce}}{\omega\left(\omega^2 - \omega_{ce}^2\right)} & 1 - \dfrac{\omega_{pe}^2}{\omega^2 - \omega_{ce}^2} & 0 \\ 0 & 0 & 1 - \dfrac{\omega_{pe}^2}{\omega^2} \end{bmatrix} \tag{2.8}$$

Where ω_{pe}, ω_{ce} are the electron plasma frequency and electron cyclotron frequency respectively, and the magnetic field is in the z direction. Now we consider that the frequency of the mode is much higher than a typical frequency of the ion motion, ion motion-related terms are neglected in the expression of Eq. (2.8). Introducing a non-dimensional parameter $\boldsymbol{n} \equiv \boldsymbol{kc}/\omega$ which has the magnitude of refractive index, Eq. (2.7) is written as

$$\boldsymbol{n} \times (\boldsymbol{n} \times \boldsymbol{E}) + \hat{\varepsilon} \cdot \boldsymbol{E} = 0. \tag{2.9}$$

Defining an angle between the external magnetic field vector and the refractive index vector as θ, and assuming the refractive index vector to be in the x-z plane, i.e., $\boldsymbol{k} = k \cdot (\sin\theta, 0, \cos\theta)$, Eq. (2.9) can be expanded explicitly as

$$\begin{pmatrix} 1 - \dfrac{\omega_{pe}^2}{\omega^2 - \omega_{ce}^2} - n^2\cos^2\theta & -j\dfrac{\omega_{pe}^2\omega_{ce}}{\omega\left(\omega^2 - \omega_{ce}^2\right)} & n^2\cos\theta\sin\theta \\ j\dfrac{\omega_{pe}^2\omega_{ce}}{\omega\left(\omega^2 - \omega_{ce}^2\right)} & 1 - \dfrac{\omega_{pe}^2}{\omega^2 - \omega_{ce}^2} - n^2 & 0 \\ n^2\cos\theta\sin\theta & 0 & 1 - \dfrac{\omega_{pe}^2}{\omega^2} - n^2\sin^2\theta \end{pmatrix} \begin{pmatrix} E_x \\ E_y \\ E_z \end{pmatrix} = 0 \tag{2.10}$$

This equation represents simultaneous equations for three elements of $\boldsymbol{E}$ ($\neq 0$). In order for these elements to have a nontrivial solution, the determinant of the matrix must be zero. This condition gives several dispersion relation of the modes. From the

condition, we obtain a quadratic equation for n as

$$An^4 - Bn^2 + C = 0. \tag{2.11}$$

Here,

$$A = \left(1 - \frac{\omega_{pe}^2}{\omega^2 - \omega_{ce}^2}\right)\sin^2\theta + \left(1 - \frac{\omega_{pe}^2}{\omega^2}\right)\cos^2\theta \tag{2.12}$$

$$\begin{aligned} B = &\left(1 - \frac{\omega_{pe}^2}{\omega(\omega + \omega_{ce})}\right)\left(1 - \frac{\omega_{pe}^2}{\omega(\omega - \omega_{ce})}\right)\sin^2\theta \\ &+ \left(1 - \frac{\omega_{pe}^2}{\omega^2}\right)\left(1 - \frac{\omega_{pe}^2}{\omega^2 - \omega_{ce}^2}\right)\left(1 + \cos^2\theta\right) \end{aligned} \tag{2.13}$$

$$C = \left(1 - \frac{\omega_{pe}^2}{\omega^2}\right)\left(1 - \frac{\omega_{pe}^2}{\omega(\omega + \omega_{ce})}\right)\left(1 - \frac{\omega_{pe}^2}{\omega(\omega - \omega_{ce})}\right). \tag{2.14}$$

By solving Eq. (2.11) for n^2, we can get

$$n^2 = 1 - \frac{2(A - B + C)}{2A - B \pm \left(B^2 - 4AC\right)^{1/2}}. \tag{2.15}$$

Equation (2.15) is written as follows by substituting Eqs. (2.12)-(2.14) into Eq. (2.15).

$$n^2 = 1 - \frac{2\omega_{pe}^2\left(\omega^2 - \omega_{pe}^2\right)/\omega^2}{2\left(\omega^2 - \omega_{pe}^2\right) - \omega_{ce}^2\sin^2\theta \pm \omega_{ce}\Delta} \tag{2.16}$$

Where,

$$\Delta = \left\{\omega_{ce}^2\sin^4\theta + 4\omega^{-2}\left(\omega^2 - \omega_{pe}^2\right)^2\cos^2\theta\right\}^{1/2}. \tag{2.17}$$

Equation (2.16) is the Altar-Appleton-Hartree dispersion relation for cold plasma electromagnetic electron modes. A convenient factoring of Eq. (2.16) is obtained with approximations based on the relative size of the two terms in Δ. The two possibilities are

$$\omega_{ce}^2 \sin^4\theta >> 4\omega^{-2}\left(\omega^2-\omega_{pe}^2\right)^2\cos^2\theta \tag{2.18}$$

$$\omega_{ce}^2 \sin^4\theta << 4\omega^{-2}\left(\omega^2-\omega_{pe}^2\right)^2\cos^2\theta . \tag{2.19}$$

With the first of these approximations, we have the ordinary (O) and extraordinary (X) modes according to the ± choice of sign in Eq. (2.16).

$$n^2 = \frac{\omega^2-\omega_{pe}^2}{\omega^2-\omega_{pe}^2\cos^2\theta} \qquad \text{O MODE} \tag{2.20}$$

$$n^2 = \frac{\left(\omega^2-\omega_{pe}^2\right)^2-\omega^2\omega_{ce}^2\sin^2\theta}{\omega^2\left(\omega^2-\omega_{pe}^2\right)-\omega^2\omega_{ce}^2\sin^2\theta} \qquad \text{X MODE} \tag{2.21}$$

Now we consider the wave propagates perpendicular to external magnetic field ($\theta=\pi/2$), which is the same situation as the experiment we performed in this study. Then, the refractive indices of each mode are given by

$$n^2 = 1-\omega_{pe}^2/\omega^2 \tag{2.22}$$

$$n^2 = 1-\frac{\omega_{pe}^2}{\omega^2}\frac{\omega^2-\omega_{pe}^2}{\omega^2-\omega_{pe}^2-\omega_{ce}^2} . \tag{2.23}$$

The polarization of the electric field of each mode is obtained from comparison between Eq. (2.10) and Eq. (2.22) or (2.23). In the case of O mode,

$$E_x=0,\ E_y=0,\ E_z\neq 0. \tag{2.24}$$

While, in the case of X mode,

$$\frac{jE_x}{E_y} = \frac{-\omega_{pe}^2\omega_{ce}}{\omega\left(\omega^2-\omega_{pe}^2-\omega_{ce}^2\right)},\ E_z=0. \tag{2.25}$$

\That is, the electric field of the wave polarized in O mode is parallel to the external magnetic field, and that in X mode is perpendicular to the external magnetic field.

2-2 Cross-Polarization Scattering by Magnetic Fluctuations

In this section, we will describe electromagnetic wave scattering mechanism due to magnetic and density fluctuations. Propagating electromagnetic wave in the dielectric medium induces current due to electric field of the source wave. This current can not induce electromagnetic waves except for the source wave in the static medium, however, it can induce electromagnetic scattering waves due to deviation of the induced current by the several fluctuations.

In subsection 2-2-1, the induced current by the magnetic and density fluctuations is described numerically in order to clarify relation between magnitude of the scattering waves and that of the fluctuations.

In subsection 2-2-2, the relation between the electric field of the scattered wave and frequencies and wave numbers of the magnetic and density fluctuations is described numerically.

2-2-1 Induced Current by Magnetic and Density Fluctuations [9]

A wave equation of the scattered wave in the dielectric medium is derived by considering Maxwell's equation and constitutive equations. The wave equation is

$$\nabla\times(\nabla\times\boldsymbol{E}_s)-\left(\frac{\omega}{c}\right)^2\left(1+\frac{\sigma}{j\omega\varepsilon_0}\right)\frac{\partial^2\boldsymbol{E}_s}{\partial t^2}=-\mu_0\frac{\partial\boldsymbol{J}}{\partial t}, \tag{2.26}$$

where $\boldsymbol{E}_s$ is the electric field of the scattered wave, and ε_0 and μ_0 are the dielectric constant and magnetic permeability in the vacuum respectively. And $\boldsymbol{J}$ is the induced

current by the magnetic and density fluctuations that induces scattering of the electromagnetic wave. The induced current by the fluctuations is derived as follows by taking account of fluid equation of electrons in equilibrium state.

$$nm_e \frac{d\boldsymbol{v}}{dt} = -en(\boldsymbol{E} + \boldsymbol{v} \times \boldsymbol{B}) + \boldsymbol{P}_{ei} = -en(\boldsymbol{E} + \boldsymbol{v} \times \boldsymbol{B}) + \eta e^2 n^2 \boldsymbol{v}$$
$$= -en(\boldsymbol{E} + \boldsymbol{v} \times \boldsymbol{B}) + \frac{e^2 n^2 \boldsymbol{v}}{\sigma} = 0 \tag{2.27}$$

Where m_e and e are the electron mass and elementary charge respectively. And $\boldsymbol{P}_{ei}$ denotes frictional force between electrons and ions, and η is the resistivity of the plasma. Now, we consider perturbation fields, i.e., $\boldsymbol{E} = \boldsymbol{E}_i + \boldsymbol{E}_s$, $\boldsymbol{B} = \boldsymbol{B}_0 + \tilde{\boldsymbol{B}}$, $n = n + \tilde{n}$, $\sigma = \sigma + \tilde{\sigma}$, where $\boldsymbol{E}_i$ and $\boldsymbol{E}_s$ are the electric field of the incident and scattered wave, and $\boldsymbol{B}_0$ and $\tilde{\boldsymbol{B}}$ are the external magnetic field and magnetic fluctuation respectively. And n and $\tilde{n}$ are the static component and fluctuation component of the electron density, and σ and $\tilde{\sigma}$ are the static and perturbed component of the conductivity, respectively. By substituting these perturbation fields into Eq. (2.27), we have

$$-e(n+\tilde{n})(\boldsymbol{E}_i + \boldsymbol{E}_s) - (\sigma + \tilde{\sigma})(\boldsymbol{E}_i + \boldsymbol{E}_s) \times (\boldsymbol{B}_0 + \tilde{\boldsymbol{B}}) + \frac{en}{\sigma}(\sigma + \tilde{\sigma})(\boldsymbol{E}_i + \boldsymbol{E}_s) = 0. \tag{2.28}$$

While, electric fields of the incident wave and the scattered wave satisfy following fluid equations with the static field.

$$-enE_i - \sigma E_i \times B_0 + \frac{en}{\sigma}\sigma E_i = 0 \tag{2.29 a}$$

$$-enE_s - \sigma E_s \times B_0 + \frac{en}{\sigma}\sigma E_s = 0 \tag{2.29 b}$$

By substituting Eqs. (2.29) into Eq. (2.28) and neglecting secondary components of the perturbation in Eq. (2.28), equation (2.28) becomes

$$-e\tilde{n}(\boldsymbol{E}_i + \boldsymbol{E}_s) - \sigma(\boldsymbol{E}_i + \boldsymbol{E}_s) \times \tilde{\boldsymbol{B}} - \tilde{\sigma}\boldsymbol{E}_s \times \boldsymbol{B}_0 + \frac{\tilde{\sigma}}{\sigma} en(\boldsymbol{E}_i + \boldsymbol{E}_s) = 0. \tag{2.30}$$

Here, induced current in Eq. (2.26) is induced from interaction between electric field

of the incident wave and $\tilde{\sigma}$, $\tilde{n}$, $\tilde{B}$, so that, terms that relate to electric field of the scattered wave are negligible in Eq (2.30). Consequently, we obtain the induced current by the magnetic and the density fluctuations, that is,

$$J = \tilde{\sigma}E_i = \sigma\frac{\tilde{n}}{n}E_i + \frac{1}{en}\sigma\left[\sigma E_i \times \tilde{B}\right]. \tag{2.31}$$

Where, coefficients in Eq. (2.31) are written as $\sigma = -j\varepsilon_0\omega_{pe}^2/\omega$, $1/en = \omega_{ce}/\varepsilon_0\omega_{pe}^2 B_0$. By substituting these coefficients into Eq. (2.31), it is rewritten as

$$J = -\frac{j\varepsilon_0\omega_{pe}^2}{\omega}\frac{\tilde{n}}{n}E_i + \frac{\omega_{ce}}{\varepsilon_0\omega_{pe}^2}\sigma\left[\sigma E_i \times \frac{\tilde{B}}{B_0}\right]. \tag{2.32}$$

The first and second term of the right hand of Eq. (2.32) indicate component of induced current due to density and magnetic fluctuation respectively. Polarization of the scattering wave due to density fluctuation is same to that of the incident wave. While, the electric field of the scattering wave by magnetic fluctuation is perpendicular to that of the incident wave, i.e., the incident wave in O (X) mode is converted into X (O) mode due to magnetic fluctuation. This effect is called cross-polarization scattering.

In order to correspond the induced current to physical image, the scattering process by density (a) and magnetic (b) fluctuations based on Eq. (2.32) are shown in Fig. 2.1. In the existence of density fluctuation (a), the induced current parallel to the electric field of the incident wave is induced due to the incident wave. Thus, the magnitude of the induced current is proportional to the magnitude of the density fluctuation. On the other hand, in the existence of magnetic fluctuation (b), reradiation source is induced by the cross product of magnetic fluctuation vector with induced current by the electric field vector of the incident wave. Thus, the electric field of the scattered wave is perpendicular to that of the incident wave, and the magnitude of the induced current is proportional to the magnitude of the magnetic fluctuation.

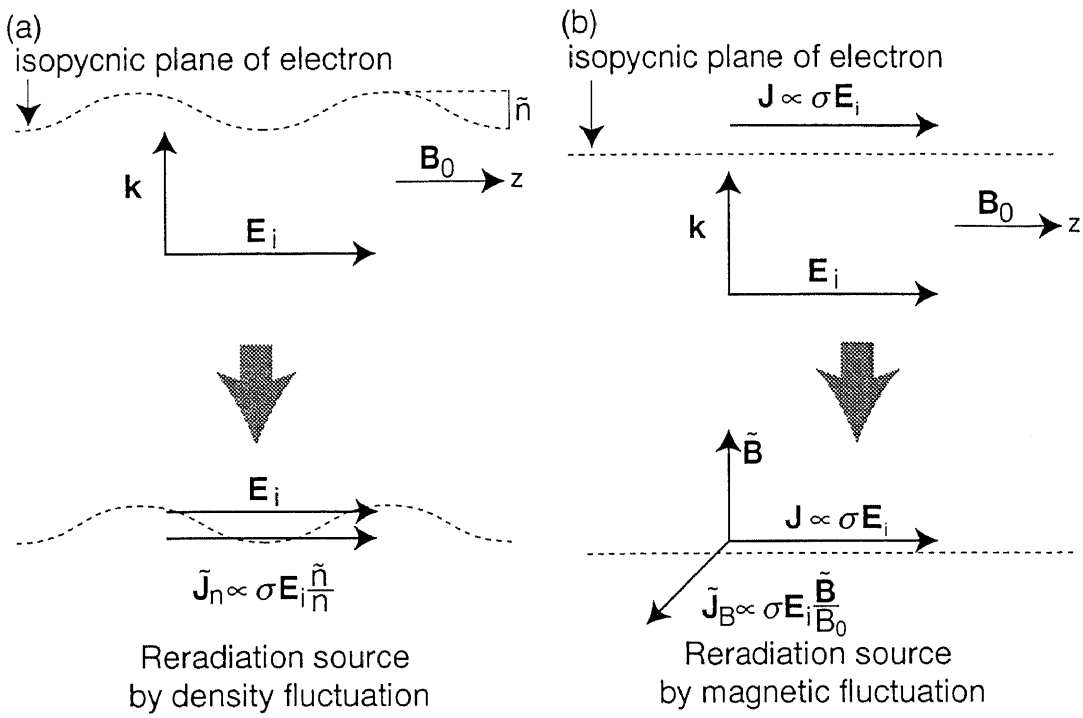

Figure 2. 1 Schematic view of the scattering process by density and magnetic fluctuation

2-2-2 Electric Field of the Scattered Wave by Magnetic and Density Fluctuations [18]

When an incident electromagnetic wave is injected to a plasma, the electrons in the plasma are accelerated by the electric field of the incident wave, and the accelerated electrons reradiate electromagnetic wave in all directions. This is the mechanism of electromagnetic wave scattering. The electric field of the scattered wave due to these electrons is obtained from Lienard-Wiechert's potential [19] as

$$E_s(r,t)=\frac{e}{4\pi\varepsilon_0 c}\left[\frac{n\times\{(n-\beta)\times d\beta/dt\}}{(1-\beta\cdot n)^3 R}\right]_{\text{ret}}, \tag{2.33}$$

where, r, t indicate evaluation position and time of the electric field, and β and n are the ratio of electron velocity to the speed of light and a unit vector directing to an

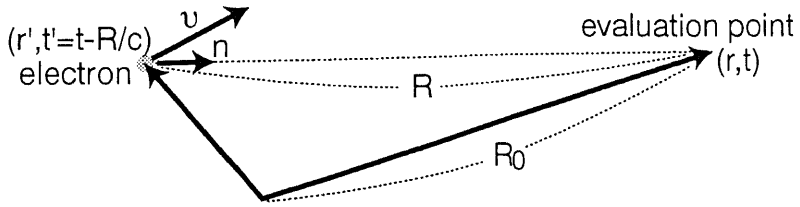

Figure 2.2 Coordinate systems for Eq. (2.33)

evaluation point from an electron respectively. And R indicates the distance from the electron to the evaluation point, and subscript "ret" means that the value in the brackets is evaluated at the retarded time $t=t'-R/c$. These coordinate systems are illustrated in Fig. 2.2. In the low electron temperature case (T_e<1 keV) like GAMMA10 plasma, Eq. (2.33) is written by β<<1 as

$$\boldsymbol{E}_s(\boldsymbol{r},t)=\frac{e}{4\pi\varepsilon_0 c^2 R}\left[\boldsymbol{n}\times\{\boldsymbol{n}\times d\boldsymbol{v}/dt\}\right]_{\mathrm{ret}}. \tag{2.34}$$

The electrons are forced to vibrate by the electromagnetic field of the incident wave. The equation of motion is given by

$$m\frac{d\boldsymbol{v}}{dt}=e\left(\boldsymbol{E}_i+\boldsymbol{v}\times\boldsymbol{B}_0\right), \tag{2.35}$$

where $\boldsymbol{E}_i$ and $\boldsymbol{B}_0$ are the electric field of the incident wave and the external magnetic field, respectively.

Let us denote the monochromatic plane wave with frequency ω_i and wave number vector $\boldsymbol{k}_i$, by the form $E_i=E_0\cos(\omega_i t-\boldsymbol{k}_i\cdot\boldsymbol{r})$. The acceleration force to the electron is

$$d\boldsymbol{v}/dt=\frac{e}{m}\left\{E_0\cos(\omega_i t-\boldsymbol{k}_i\cdot\boldsymbol{r})+\boldsymbol{v}\times\boldsymbol{B}_0\right\}. \tag{2.36}$$

By substituting Eq. (2.36) to Eq. (2.34), it is written as

$$\boldsymbol{E}_s(\boldsymbol{r},t)=\frac{e^2}{4\pi\varepsilon_0 mc^2 R}\left\{\left[\boldsymbol{n}\times\{\boldsymbol{n}\times\boldsymbol{E}_0\}\right]\cos(\omega_i t-\boldsymbol{k}_i\cdot\boldsymbol{r})+\left[\boldsymbol{n}\times\{\boldsymbol{n}\times(\boldsymbol{v}\times\boldsymbol{B}_0)\}\right]\right\}. \tag{2.37}$$

Equation (2.37) indicates electric field of the scattered wave by an electron in the scattering region. In order to evaluate the electric field of the scattered wave from all electrons that exist in the scattering region, Eq. (2.37) should be summed up in the scattering volume V_s as

$$\begin{aligned} E_s(r,t) &= r_0\left[n\times\{n\times E_0\}\right]\iint_{V_s} dr'\frac{n(r',t')\cos(\omega_i t-k_i\cdot r)}{R} \\ &\quad+\frac{e^2}{4\pi\varepsilon_0 mc^2}\int_{V_s} dr'\frac{n(r',t')\left[n\times\{n\times(v\times B_0)\}\right]}{R} \\ &= r_0\left[n\times\{n\times E_0\}\right]\iint_{V_s} dr'\frac{n(r',t')\cos(\omega_i t-k_i\cdot r)}{R} \\ &\quad+\frac{e}{4\pi\varepsilon_0 mc^2}\int_{V_s} dr'\frac{\left[n\times\{n\times(\sigma E_0\times B_0)\}\right]}{R}\cos(\omega_i t-k_i\cdot r) \end{aligned}, \tag{2.38}$$

where $n(r',t')$ is the electron density at the position r' and $r_0=e^2/4\pi\varepsilon_0 mc^2$ denotes the classical electron radius. Generally, potentials in a plasma are screened out in a distance of Debye length defined as $\lambda_D=(k_B T_e/4\pi ne^2)^{1/2}$. The cloud of shielding charge surrounding around each particle eliminates the electric field outside of the clouds. On a small distance compared to a Debye length, i.e., $k\lambda_D>>1$, where k is the wave number of fluctuation, the particle position is uncorrelated, and the electric field of the scattered wave is superposition by individual electrons. On the other hand, for $k\lambda_D\leq 1$, collective effects such as waves in a plasma can be introduced to the scattering problem. Here, we consider the density and the magnetic fluctuation with the wave number k and frequency ω, and rewrite the electron density $n(r',t')$ and external magnetic field $B_0(r',t')$ by the Fourier integral expression as,

$$n(r',t')=\int\frac{d\omega}{2\pi}\int\frac{dk}{(2\pi)^3}n(k,\omega)e^{j(\omega t'-k\cdot r')} \tag{2.39 a}$$

$$B_0(r',t')=\int\frac{d\omega}{2\pi}\int\frac{dk}{(2\pi)^3}B(k,\omega)e^{j(\omega t'-k\cdot r')}, \tag{2.39 b}$$

and the cosine factor by

$$\cos(\omega_i t' - \boldsymbol{k}_i \cdot \boldsymbol{r}') = \frac{1}{2}\left[e^{j(\omega_i t' - \boldsymbol{k}_i \cdot \boldsymbol{r}')} + e^{-j(\omega_i t' - \boldsymbol{k}_i \cdot \boldsymbol{r}')}\right]. \tag{2.40}$$

Then, equation (2.38) is represented as

$$\begin{aligned} \boldsymbol{E}_s(\boldsymbol{r},t) = {} & \frac{r_0}{2}\left[\boldsymbol{n}\times\{\boldsymbol{n}\times\boldsymbol{E}_0\}\right]\times \\ & \iiint_{V_S} \frac{n(\boldsymbol{k},\omega)}{(2\pi)^4 R}\left[e^{j\{(\omega_i+\omega)t'-(\boldsymbol{k}_i+\boldsymbol{k})\cdot\boldsymbol{r}'\}} + e^{-j\{(\omega_i-\omega)t'-(\boldsymbol{k}_i-\boldsymbol{k})\cdot\boldsymbol{r}'\}}\right] d\omega d\boldsymbol{k} d\boldsymbol{r}' \\ & + \frac{e}{4\pi\varepsilon_0 mc^2}\iiint_{V_S} \frac{d\omega d\boldsymbol{k} d\boldsymbol{r}'}{(2\pi)^4 2}\frac{\left[\boldsymbol{n}\times\left\{\boldsymbol{n}\times\left(\sigma\boldsymbol{E}_0\times\boldsymbol{B}(\boldsymbol{k},\omega)\right)\right\}\right]}{R}\times \\ & \left[e^{j\{(\omega_i+\omega)t'-(\boldsymbol{k}_i+\boldsymbol{k})\cdot\boldsymbol{r}'\}} + e^{-j\{(\omega_i-\omega)t'-(\boldsymbol{k}_i-\boldsymbol{k})\cdot\boldsymbol{r}'\}}\right] \end{aligned} \tag{2.41}$$

Since the observing position is sufficiently far from the scattering region, the distance R and time t' are approximated to $R \cong R_0 - \boldsymbol{n}\cdot\boldsymbol{r}'$, $t' \cong t - R_0/c + \boldsymbol{n}\cdot\boldsymbol{r}'/c$, respectively. Substituting these approximations into Eq. (2.41), we have

$$\begin{aligned} \boldsymbol{E}_s(\boldsymbol{r},t) = {} & \frac{r_0}{2R_0}\left[\boldsymbol{n}\times\{\boldsymbol{n}\times\boldsymbol{E}_0\}\right]\iiint_{V_S} \frac{d\omega d\boldsymbol{k} d\boldsymbol{r}'}{(2\pi)^4} n(\boldsymbol{k},\omega)\times \\ & \left[e^{j\{\omega_+ t-(\boldsymbol{k}-\boldsymbol{k}_+)\cdot\boldsymbol{r}'\}} + e^{-j\{\omega_- t+(\boldsymbol{k}-\boldsymbol{k}_-)\cdot\boldsymbol{r}'\}}\right] \\ & + \frac{e}{4\pi\varepsilon_0 mc^2 2R_0}\iiint_{V_S} \frac{d\omega d\boldsymbol{k} d\boldsymbol{r}'}{(2\pi)^4}\left[\boldsymbol{n}\times\left\{\boldsymbol{n}\times\left(\sigma\boldsymbol{E}_0\times\boldsymbol{B}(\boldsymbol{k},\omega)\right)\right\}\right]\times \\ & \left[e^{j\{\omega_+ t-(\boldsymbol{k}-\boldsymbol{k}_+)\cdot\boldsymbol{r}'\}} + e^{-j\{\omega_- t+(\boldsymbol{k}-\boldsymbol{k}_-)\cdot\boldsymbol{r}'\}}\right] \\ = {} & \frac{r_0}{2R_0}\left[\boldsymbol{n}\times\{\boldsymbol{n}\times\boldsymbol{E}_0\}\right]\iiint_{V_S} \frac{d\omega d\boldsymbol{k} d\boldsymbol{r}'}{(2\pi)^4} n(\boldsymbol{k},\omega)\times \\ & \left[e^{j\omega_+ t}e^{-j(\boldsymbol{k}-\boldsymbol{k}_+)\cdot\boldsymbol{r}'} + e^{-j\omega_- t}e^{-j(\boldsymbol{k}-\boldsymbol{k}_-)\cdot\boldsymbol{r}'}\right], \\ & + \frac{e}{4\pi\varepsilon_0 mc^2 2R_0}\iiint_{V_S} \frac{d\omega d\boldsymbol{k} d\boldsymbol{r}'}{(2\pi)^4}\left[\boldsymbol{n}\times\left\{\boldsymbol{n}\times\left(\sigma\boldsymbol{E}_0\times\boldsymbol{B}(\boldsymbol{k},\omega)\right)\right\}\right]\times \\ & \left[e^{j\omega_+ t}e^{-j(\boldsymbol{k}-\boldsymbol{k}_+)\cdot\boldsymbol{r}'} + e^{-j\omega_- t}e^{-j(\boldsymbol{k}-\boldsymbol{k}_-)\cdot\boldsymbol{r}'}\right] \end{aligned} \tag{2.42}$$

where $\omega_\pm = \omega_i \pm \omega$, $\boldsymbol{k}_\pm = \pm(\boldsymbol{k}_s - \boldsymbol{k}_i)$, $\boldsymbol{k}_s$ are the frequency and the wave number vector of the scattered wave respectively, and the time delay R_0/c is omitted. The integral

with respect to r' can be expressed in term of the delta function for $V_s \to \infty$, then we obtain the electric field of the scattered wave by the fluctuations as,

$$\begin{aligned} E_s(r,t) &= \frac{r_0}{2R_0}\left[n\times\{n\times E_0\}\right]\iint\frac{d\omega dk}{(2\pi)^4}n(k,\omega)\times \\ &\qquad \left[e^{j\omega_+ t}\delta(k-k_+)+e^{-j\omega_- t}\delta(k-k_-)\right] \\ &+\frac{e}{4\pi\varepsilon_0 mc^2 2R_0}\iint\frac{d\omega}{(2\pi)^4}\left[n\times\{n\times(\sigma E_0\times B(k,\omega))\}\right]\times \\ &\qquad \left[e^{j\omega_+ t}\delta(k-k_+)+e^{-j\omega_- t}\delta(k-k_-)\right] \\ &= \frac{r_0}{2R_0}\left[n\times\{n\times E_0\}\right]\int\frac{d\omega}{2\pi}\left[n(k_+,\omega)e^{j\omega_+ t}+n(k_-,\omega)e^{-j\omega_- t}\right] \\ &+\frac{e}{4\pi\varepsilon_0 mc^2 2R_0}\int\frac{d\omega}{2\pi}\left\{\begin{array}{l}\left[n\times\{n\times(\sigma E_0\times B(k_+,\omega))\}\right]e^{j\omega_+ t} \\ +\left[n\times\{n\times(\sigma E_0\times B(k_-,\omega))\}\right]e^{-j\omega_- t}\end{array}\right\} \end{aligned} \tag{2.43}$$

The first term of the right-hand side in Eq. (2.43) indicates the electric field of the scattered wave by density fluctuations, and the second term indicates that by magnetic fluctuations.

Consequently, it is found that the density and magnetic fluctuation lead to electromagnetic wave scattering, and the frequency of the scattered wave differs from that of the incident wave by fluctuation frequency, i.e., scattered wave with the frequency of ω_+ (ω_-) has the wave number of k_+ (k_-). And the wave number of the fluctuation is determined by the angle θ between normal surface of the incident wave and the scattered wave geometrically as Eq. (2.44) and Fig. 2.3.

$$|k_\pm| = 2|k_i|\sin\frac{\theta}{2} \tag{2.44}$$

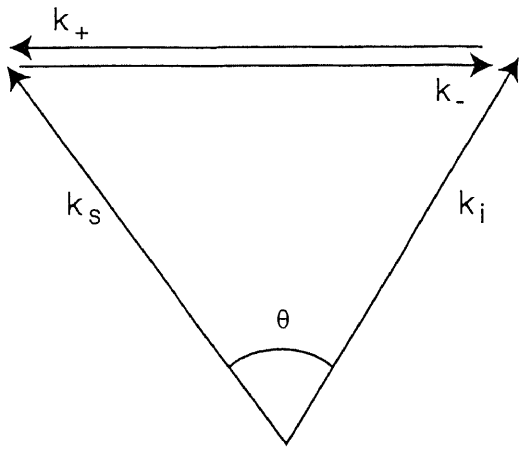

Figure 2.3 Relation between the wavenumber of incident, scattering and fluctuation waves

2-3 Comparison with Other Diagnostics

Density fluctuation measurement is one of the most difficult technique in the diagnostics with electromagnetic waves. Electromagnetic wave scattering or reflection are used in these diagnostics, and measurement with electromagnetic wave scattering is further classified according to Klein-Cook parameter and arrangement of the incident and detecting antennas. Klein-Cook parameter is obtained as,

$$Q \equiv \frac{k^2 L}{k_i}, \tag{2.45}$$

where Q is called Klein-Cook parameter, k_i and k are the wave number of the incident wave and density fluctuation respectively, and L is the width of the density fluctuation. In the case of $Q>>1$, the scattering of the electromagnetic waves obeys Bragg scattering. Conventional Thomson scattering method is utilized in this region, and it has been used to measure density fluctuations since early in the 1980s. On the other hand, in the case $Q<<1$, the scattering obeys Raman scattering. Fraunhofer Diffraction (FD) method is utilized in this region. This method is developed later in the 1980s,

and it has an advantage of measurement of small wave number region.

Reflectometer has been developed since 1990s. This method utilizes the reflection of the electromagnetic waves from the cutoff layer perturbed by the density fluctuations, and has an advantage of high spatial resolution.

Detailed characters of these diagnostics are described in the following.

Collective Thomson Scattering Method (CTS) [18, 20, 21]

In the Bragg region, the density fluctuation acts as intensity grating to the probe beam, and the scattering process obeys Bragg scattering, i.e., frequencies and wave numbers satisfy Bragg's condition between the incident wave, the scattering wave and the fluctuation. The probe beam and scattered wave intersect with a moderate scattering angle so as not to receive the probe beam as shown in Fig 2.4 (a). Frequency of the incident wave is chosen in order that the incident wave pass through the plasma, and the density fluctuation is measured in the region where the probe beam and scattered wave intersect. A wave number region to be measured in the system is determined by Eq. (2.45) and condition of the collective effect as,

$$\left(\frac{k_i}{L}\right)^{1/2} << k \leq \frac{1}{\lambda_D}. \tag{2.46}$$

Equation (2.46) indicates that large wave number region is measured by this method. The measured wave number also satisfies Eq. (2.44), so that the dispersion relation of the fluctuation is obtained by varying the scattering angle, however, the wave number of the fluctuation to be measured is limited by the size of the diagnosing port.

The minimum limit and resolution of the wave number depend on the condition that the scattering angle equals to the divergence of the probing beam, i.e.,

$$k_{\min} = \Delta k \cong \frac{2}{W_0}. \tag{2.47}$$

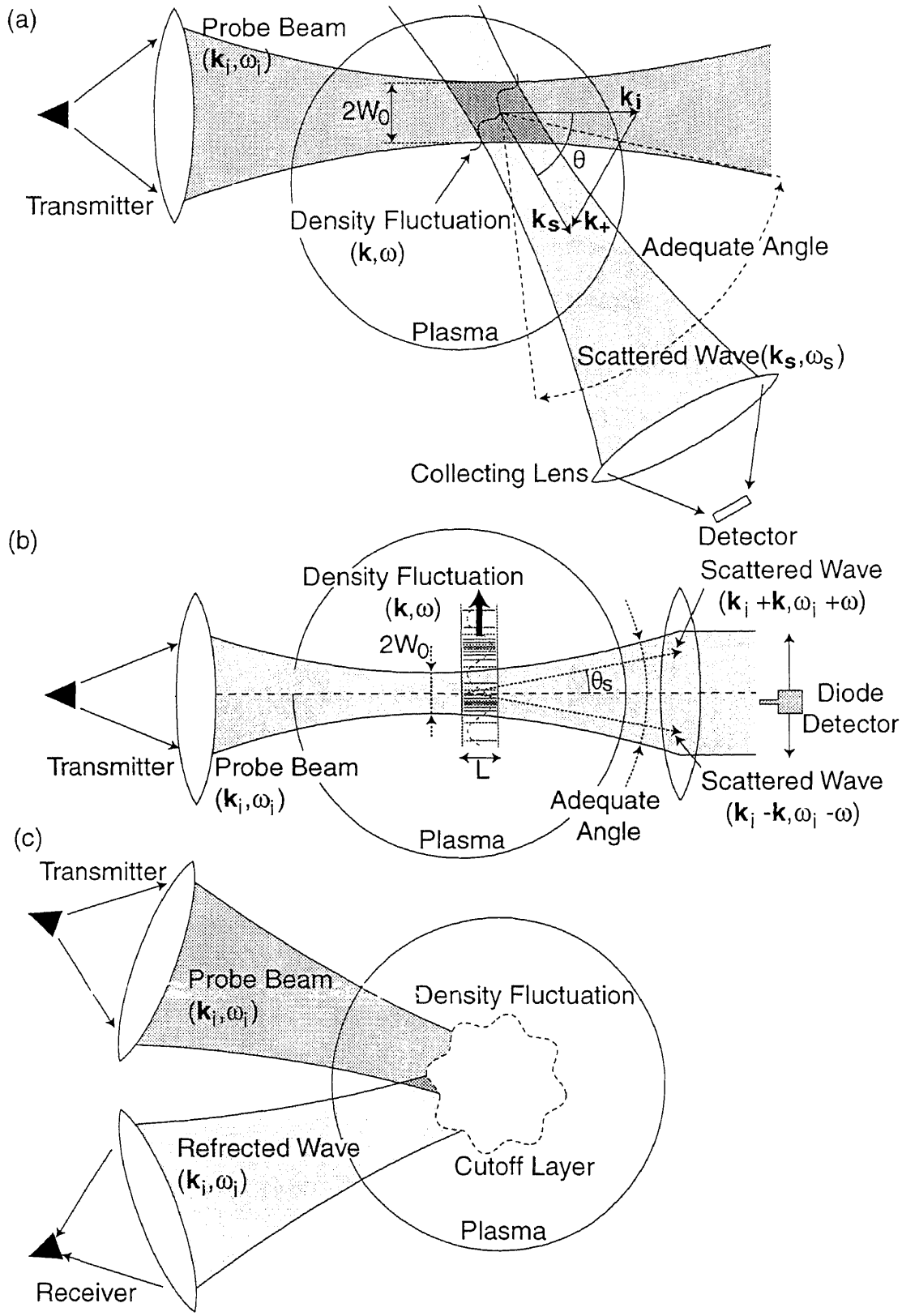

Figure 2.4 Schematic View of the CTS (a), FD(b) and reflectometer (c)

The spatial resolution perpendicular and along to the probing beam are $2W_0$ and $4W_0/\sin\theta$, respectively.

Fraunhofer Diffraction Method (FD) [22-24]

In the Raman region, the density fluctuation acts as phase grating to the probe beam, and first order of diffraction wave is induced independent of direction of fluctuation movement as shown in Fig. 2.4 (b). Two diagonal port is needed in this system, so that the accessibility of the measurement is better than CTS method. The incident wave in the range of FIR is often used in order to satisfy the condition of Clein-Cook parameter. The scattered wave is detected within the divergence of the probe beam, and measurement is performed by mixing the scattered wave and the transmitted wave. A wave number region to be measured in the system is determined by the wave number normalized by the width of the probe beam as,

$$0.1 \le \theta \le 1, \tag{2.48}$$

where, $\theta = kW_0/2$. Equation (2.48) is written with wavelength λ as,

$$\pi W_0 \le \lambda \le 10\pi W_0 . \tag{2.49}$$

Equation (2.49) indicates that the wavelength of the fluctuation with the length of approximately thirty times of the width of the beam waist can be observed by this system. And measured wave number also satisfies Eq. (2.44), so that dispersion relation of the fluctuation is obtained by scanning the diode detector across the beam at the forward focal plane. However, resolution along the probe beam is poor, so that the identification of the fluctuation is difficult, in the case more than two fluctuations are excited along the probe beam.

Reflectometer [25-28]

A schematic view of the reflectometer is shown in Fig. 2.4 (c). The frequency of the incident wave less than plasma frequency is used as a source, and amplitude or phase-modulated reflected wave from the perturbed cutoff layer is detected by the receiver. Since this system observes reflected wave, it has an advantage of good accessibility using only one diagnostic port. By mixing the detected signal with local oscillator, and analyzing the intermediate frequency signal, the frequency spectrum of the density fluctuation is obtained. This system has a high spatial resolution, however, no wave number information is obtained.

Cross-Polarization Scattering Method (CPS)

CPS method is a new technique to measure magnetic fluctuation. It is proposed early in the 1990s. This system utilizes CTS and reflectometer method simultaneously, that is, frequency of the probe beam is chosen in order that the probe beam encounters the cutoff layer, and arrangement of the antennas similar to CTS method is applied. This system can also measure the dispersion relation of the fluctuation as CTS method, however, the wave number of the fluctuation to be measured is limited due to the size of the diagnostics port. The wave numer resolution depends on the width of the probe beam as Eq. (2.47), and the spatial resolution is better than the CTS method considering that most of the scattering occurs at the cutoff layer. Addition to that, this system can measure in the small scattering angle within the divergence of the probe beam since the incident wave can not reach the receiver horn when it encounters the cutoff layer.

Maximum wave-number measured by this system is determined by the condition of Eq. (2.44). The measured wave number attains the maximum value at $\theta=\pi$, i.e., back scattering. While, the minimum wave-number is determined by the condition of Eq.

(2.47). In the practical case in the GAMMA10 measurement, the maximum and the minimum wave number measured by this system are about 7 cm^{-1} and 0.2 cm^{-1} for probing beam with frequency of 18 GHz and beam width of 10 cm.

Chapter 3

Description of the GAMMA10 Device and Fluctuations in GAMMA10

GAMMA10 is a tandem mirror device which has an effectively axisymmetric magnetic field configuration. The validity of a tandem mirror with thermal barriers as to the improvement of axial confinement has been confirmed. In recent experiments, moreover, neutrons attributed to the deuterium-deuterium (D-D) fusion reaction at the temperature of above 10 keV are observed [29].

In this chapter, the GAMMA10 device will be described in Sec. 3-1, and the heating and diagnostic systems used in GAMMA10 will be described in Secs. 3-2 and 3-3. And the several fluctuations excited in the GAMMA10 plasma will be described in Sec. 3-4.

3-1 Overview of the GAMMA10 Tandem Mirror

Configuration of the magnetic coils

GAMMA10 consists of 5 mirror cells, and total length is about 27 m as shown in Fig. 3.1. It shows the arrangement of magnetic coils, magnetic flux tube formed by the magnetic coils, distribution of the magnetic flux density on the machine axis and axial distribution of the expected plasma potential from top to bottom, respectively.

Central-cell is a main region for plasma confinement, and it is located at the center of the cells. Mirror ratio of 5 and magnetic flux density of 0.405 T at the midplane are formed by the 12 circular coils in the standard operation. The length and

the diameter of the vacuum vessel in the central-cell are 6 and 1 m, respectively. A fixed limiter with a radius of 0.18 m is installed at z=0.33 m , and it controls shape of the central-cell plasma.

Anchor-cells consists of 3 baseball coils and 2 recircularizing coils, which are connected to the both sides of the central-cell. Minimum-B field for magneto-hydro-

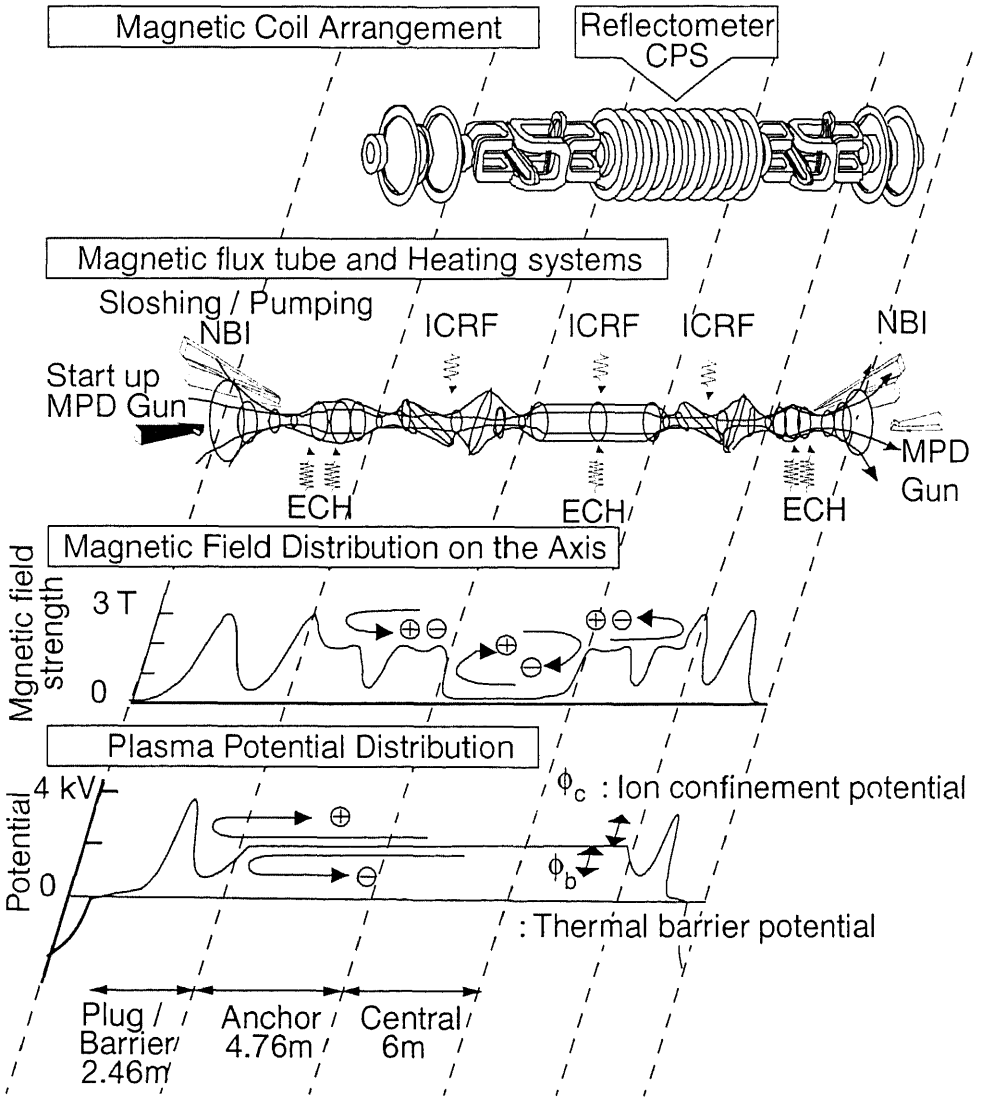

Figure 3.1 arrangement of magnetic coils, magnetic flux tube formed by the magnetic coils, distribution of the magnetic flux density on the machine axis and axial distribution of the expected plasma potential are illustrated from top to bottom.

dynamic (MHD) stability is formed by the baseball coil, i.e., radial electric field which excites MHD instabilities is suppressed by the minimum-B field. The recircularizing coils play a role in connecting the magnetic field of the central-cell and plug/barrier-cell axisymmetrically. Mirror ratio and magnetic flux density at the midplane are 3 and 0.61 T, respectively. Mirror length of anchor cell is 1.5 m.

Plug/Barrier cells are regions to form plasma potentials for ion and electron confinement. Axisymmetric magnetic field with mirror ratio of 6 is generated by 6 circular coils. Magnetic flux density at the plug and barrier region are 1 and 0.5 T, respectively. Mirror length of the cell is 2.5m.

In addition to these cells, end-regions are attached to the both end of the cells. End plates are installed in front of both end walls in order to control the plasma potential, which consist of five concentric, mutually insulated circular plates as shown in Fig. 3.2. End plates are electrically grounded or floated relative to the vacuum vessel and biased at the appropriate voltage which affect the radial electric field of the plasmas. In the standard operation, the azimuthally segmented end plates are floated from

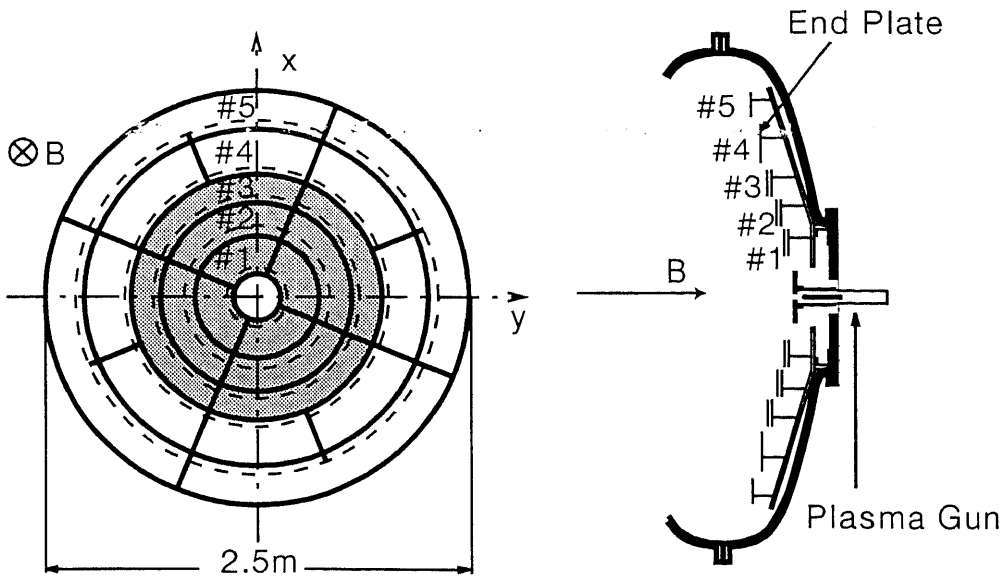

Figure 3.2 Schematic view of the end plates

the vacuum vessel through a 1 MΩ resistor so that the net current to the ends is effectively zero.

Vacuum exhaust system

Volume of the vacuum vessel of GAMMA10 is about 170 m^3. Six turbomolecular pumps, 6 helium cryopumps and 4 liquid helium cooled cryopanels are used to maintain the base pressure of $7x10^{-8}$ Torr during the plasma shot, and the total exhaust velocity of these pumps is 2712 m^3/s. ECR discharge cleaning with helium and baking process of the vacuum vessel are performed for preparation of the plasma shot.

3-2 Heating Systems

The GAMMA10 plasma is produced by the plasma guns, gas puffing system and ICRF power. The initial plasma with high ionization degree is produced by the plasma guns, which utilizes magneto-plasma-dynamic (MPD) arcjets, and they are injected into the central-cell from both ends along to magnetic field line. Duration of the MPD pulse is about 1 ms in the standard operation. After injection of MPD plasma, hydrogen gas is fueled into the initial plasma by the gas puffing systems. Finally, main plasma is started up by the ICRF heating of the gas. Arrangement of the gas puffing systems and various heating systems are shown in Fig. 3.3. In the standard operation, gas puffing systems of #1b, #2b, #3a and #4a are used.

ICRF (Ion Cyclotron Range of Frequency)

Two types of ICRF systems are used to produce and heat plasma, and are installed in the central-cell. The ICRF waves with frequencies of 9.9 and 10.3 MHz are excited in the plasma by the RF1 oscillator through Nagoya-Type III antennas located

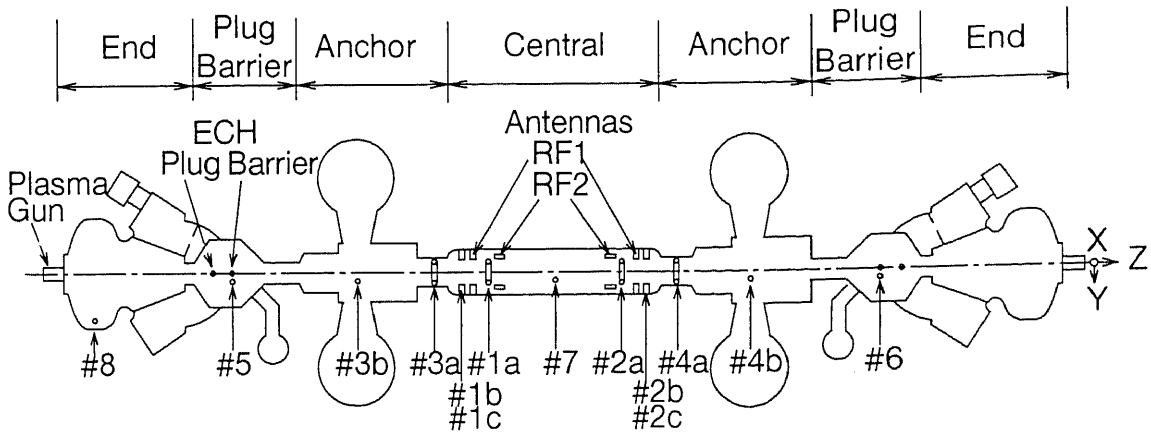

Figure 3.3 Arrangement of the heating systems and gas paffing systems

at z = ±2.2 m. These frequencies correspond to the ion cyclotron frequency at the midplane of the anchor cell. These waves not only produce a plasma in the central and anchor-cell region, but also heat the ions through ion cyclotron resonance heating in order to produce high beta plasmas for MHD stability [30, 31]. The maximum pulse duration and the total output power of the RF1 system are 500 ms and 1 MW, respectively. Another type of ICRF wave is used for heating ions in the central-cell. The ICRF wave with a frequency of 6.36 MHz is excited by the RF2 oscillator, and it is injected into the plasma by the double-half-turn antenna installed at z = ±1.7 m. This frequency corresponds to the ion cyclotron frequency near the midplane of the central cell. The maximum pulse duration and the total output power of the RF2 system are also 500 ms and 1 MW, respectively. Typically, the ion temperature and plasma density attain 5 keV and 2×10^{12} cm^{-3} by the application of the ICRF waves.

ECRH (Electron Cyclotron Resonance Heating)

The plug/barrier ECRH systems are used to form confinement potentials for ions and electrons. These systems utilize 4 gyrotrons with frequency of 28 GHz and maximum output power of 150 kW. This frequency corresponds to the electron cyclo-

tron frequency at the plug region and the second harmonics of the electron cyclotron frequency at the barrier region, respectively. These microwaves in the X mode are launched by Vlasov-Nakajima parabolic reflector antennas via low-loss oversize-waveguides, and electrons are heated by these microwaves through electron cyclotron damping. Warm electrons produced by the plug-ECRH are running away from the plug region due to axial gradient of the magnetic field, so that the potential hill for ion confinement is formed at the plug region. While, the barrier-ECRH produce hot electrons in the barrier region. Since axial gradient of the magnetic field in this region is nearly zero, the hot electrons are confined in the midplane of the barrier region. Consequently, the potential dip is produced by these electrons.

In addition to these systems, central-ECRH system is installed at the central cell to produce hot electrons. The frequency and the output power is same to the plug/barrier-ECRH systems. And this frequency corresponds to the second harmonics frequency of the electron cyclotron frequency at the central-cell. This system is used for suppression of the ion energy loss induced by the electron drag [32].

NBI (Neutral Beam Injection)

Two types of NBI systems are installed in the plug/barrier-cells, one in called sloshing NBI system and the another is called pumping NBI system. The sloshing NBI system injects a neutral hydrogen beam at the angle of 41 degree to the magnetic field line. This system produces sloshing ion distribution at plug/barrier region in order to form ion confining potential efficiently. The pumping NBI system also injects a neutral hydrogen beam at the angle of 30 degree. This system is used to sustain the confining potential by driving cold ions out of the thermal barrier by charge exchange process.

3-3 Diagnostics

Several diagnostics are used in GAMMA10 for measurement of plasma parameters such as density, temperature, potential. In this section, several diagnostics relating to the thesis are introduced briefly.

Microwave interferometer

In GAMMA10, the line integrated density is measured with seven Mach-Zehnder-type microwave interferometers, which are installed in the central cell, east and west anchor cells, inner mirror throat between the anchor cell and the plug/barrier cell, east and west barrier cells, east and west plug cells, and the central mirror throat between the central cell and east anchor cell. Especially, a transmitter and receiver of interferometer installed in the central cell are movable along the y-axis, and radial density profile is deduced by application of Abel inversion technique to chordal line-density profiles.

Soft x-ray detector [33]

Several types of x-ray diagnostic systems are installed in order to diagnose the electron temperature and its distribution function, such as x-ray pulse-height analyzer (PHA) and x-ray absorption method using semiconductor and microchannel-plate (MCP) detectors. The PHA and absorption methods are applied to the plug/barrier and central-cell plasmas for the measurement of energy spectra and temperature profiles, respectively.

HIBP (Heavy Ion Beam Probe) [34]

The radial profiles of plasma potential in the central-cell (z = 1.2 m) and barrier midplane (z = -8.8 m) are measured with HIBP using neutral Au^0-beam. An incident beam accelerated up to 16 kV can be swept radially across the plasma using an electrostatic deflector. Ions are discharged by the plasma along with the beam orbit. The Au^+ beam are detected by the electrostatic energy analyzer of a parallel plate type with micro-channel plate. The energy and time resolutions of the system are less than 50 V and 200 μs, respectively.

CX-NPA (Charge eXchange Neutral Particle Analyzer) [35]

CX-NPA is used for the measurement of ion temperature using charge exchange reaction with neutral hydrogen atoms. The system is installed in the central-cell (z = -0.6m), which is the same axial position as the scanning interferometer. The viewing angle of the system can be changed from -8.0 to +8.0 degree, which almost covers the whole cross section of the plasma. At each angle the energy distribution of CX-neutrals up to 30 keV is observed. The ion temperature profiles are calculated by the chordal data obtained by radial scan together with the density profile, plasma pressure, H_α profile and T_e profile.

3-4 Fluctuations in GAMMA10

Several types of fluctuations are excited in the GAMMA10 plasma. These fluctuations are considered to induce radial or axial transport of plasma particles. In this section, we describe the fluctuations mainly excited in GAMMA10. These fluctuations are classified into following types according to type of the driving force and

frequency range.

Flute instability [36]

In the simple magnetic confinement system, the Rayleigh-Taylor instability is excited easily, since a high-pressure plasma is sustained by the magnetic field, that is, a heavy matter is sustained by a light matter.

For simplicity derivation of the instability, now we assume that a boundary between the plasma and the vacuum is in the y-z plane as shown in Fig. 3.4 (a), and the external magnetic field is spreaded over the plasma and the vacuum uniformly. We also assume the temperature of ions and electrons to be zero, i.e., plasma-beta is low. A vector of the force g caused by the plasma pressure and/or curvature of the external magnetic field is in the positive or negative x direction, and the force is assumed to be

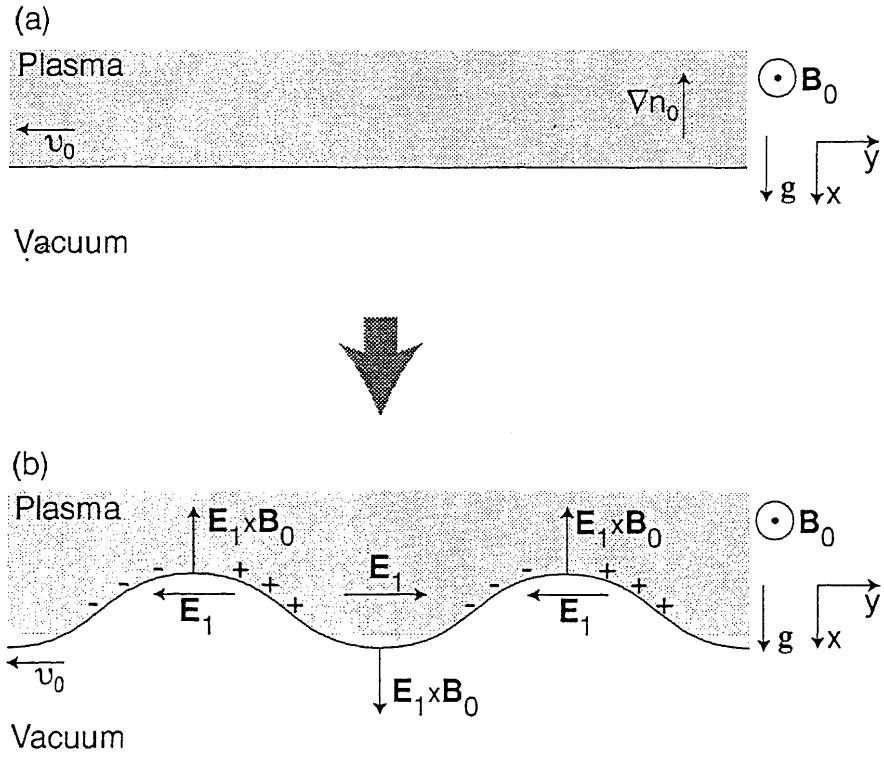

Figure 3.4 Physical mechanism of the flute instability

a constant. A vector of density gradient is also in the negative x direction.

The ions and the electrons move toward to the negative y direction with a velocity of $\boldsymbol{v}_0$ due to the $\boldsymbol{g}\times\boldsymbol{B}_0$ drift. In the equilibrium condition, the ions obey following equation of motion.

$$m_i n_0(\boldsymbol{v}_{i0}\cdot\nabla)\boldsymbol{v}_0 = en_0\boldsymbol{v}_{i0}\times\boldsymbol{B}_0 + m_i n_0\boldsymbol{g} \tag{3.1}$$

Where, m_i and n_0 are the mass of an ion and the ion density, respectively. Since the force $\boldsymbol{g}$ is assumed to be a constant, $\boldsymbol{v}_0$ becomes constant, i.e., left term of the Eq. (3.1) equals to zero. Taking the cross product of Eq. (3.1) with $\boldsymbol{B}_0$, we have the drift velocity of the ion, as

$$\boldsymbol{v}_{i0} = \frac{m_i}{eB_0^2}\boldsymbol{g}\times\boldsymbol{B}_0 = -\frac{g}{\omega_{ci}}\hat{\boldsymbol{y}}, \tag{3.2}$$

where ω_{ci} is the ion cyclotron frequency. While, the drift velocity of the electron is negligible compared to that of the ions, since the electron cyclotron frequency is much higher than the ion cyclotron frequency. These velocities make random thermal fluctuations grown as shown in Fig. 3.4 (b). That is, the electric field $\boldsymbol{E}_1$ is generated due to the difference of the drift velocity between the ion and the electron, and these are forced to move positive or negative y direction by $\boldsymbol{E}_1\times\boldsymbol{B}_0$ drift. Consequently, the disturbed boundary grows unlimitedly.

In the cylindrical plasma, flute-like boundary is formed by the instability as shown in Fig. 3.5, so that this instability is called "flute instability".

In the perturbed field such as Fig. 3.4 (b), the equation of motion for the ions is rewritten as,

$$\begin{aligned} m_i(n_0+n_1)\left[\frac{\partial}{\partial t}(\boldsymbol{v}_{i0}+\boldsymbol{v}_{i1})+(\boldsymbol{v}_{i0}+\boldsymbol{v}_{i1})\cdot\nabla(\boldsymbol{v}_{i0}+\boldsymbol{v}_{i1})\right] \\ = e(n_0+n_1)\left[\boldsymbol{E}_1+(\boldsymbol{v}_{i0}+\boldsymbol{v}_{i1})\times\boldsymbol{B}_0\right]+m_i(n_0+n_1)\boldsymbol{g} \end{aligned}, \tag{3.3}$$

where, n_1 and $\boldsymbol{v}_{i1}$ are the perturbed component of the ion density and the drift velocity,

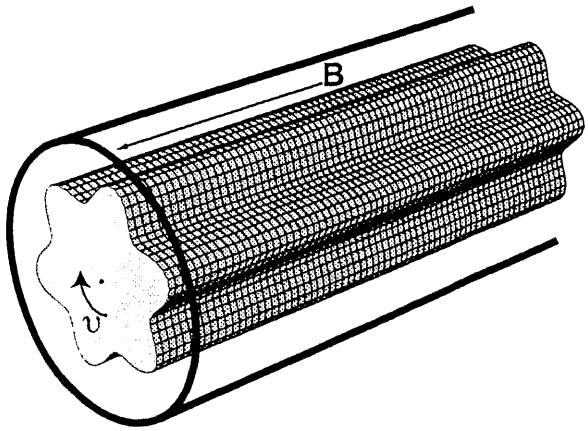

Figure 3.5 Schematic view of the flute instability

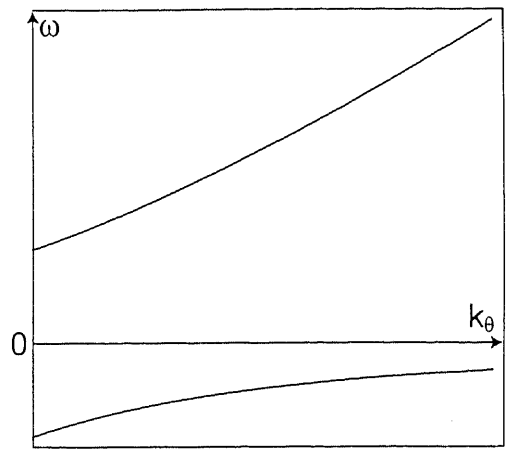

Figure 3.6 Dispersion relation of the flute instability

respectively. By using Eqs. (3.1) and (3.3), and neglecting the second-order term of the perturbed component in the equation, we have the equation of motion for the first order component of the perturbed ions by

$$m_i n_0\left[\frac{\partial \boldsymbol{v}_{i1}}{\partial t}+(\boldsymbol{v}_{i0}\cdot\nabla)\boldsymbol{v}_{i1}\right]=en_0(\boldsymbol{E}_1+\boldsymbol{v}_{i1}\times\boldsymbol{B}_0). \tag{3.4}$$

Using quasi-linear approximation, and substituting each component of the perturbed-ion velocity and the perturbed-electric field, i.e., $\boldsymbol{v}_{i1}=v_{ix}\hat{x}+v_{iy}\hat{y}$, $\boldsymbol{E}_1=\boldsymbol{E}_{1y}\hat{y}$, into Eq. (3.4), we have the each component of the ion velocity as,

$$v_{ix}=\frac{e}{m_i\omega_{ci}}E_{1y}=\frac{E_{1y}}{B_0} \tag{3.5 a}$$

$$v_{iy}=-j\frac{\omega-kv_{i0}}{\omega_{ci}}\frac{E_{1y}}{B_0}. \tag{3.5 b}$$

Where, ω and k are the frequency and wave number of the fluctuation, respectively. And relation $\omega_{ci}^2>>(\omega-kv_{i0})^2$ is adopted to derive Eqs. (3.5).

Each velocity for the electron is derived in the same manner. Now we consider that the electron cyclotron frequency is much higher than the ion cyclotron frequency, each component of the velocity for the electron are

$$\upsilon_{ex} = \frac{E_{1y}}{B_0} \tag{3.6 a}$$

$$\upsilon_{ey} = 0 \tag{3.6 b}$$

Next, continuity equation for the first order of the perturbed component is written for the ion as,

$$\frac{\partial n_1}{\partial t} + (\boldsymbol{\upsilon}_{i0} \cdot \nabla) n_1 + (\boldsymbol{\upsilon}_{i1} \cdot \nabla) n_0 + n_0 \nabla \cdot \boldsymbol{\upsilon}_{i1} = 0. \tag{3.7}$$

Using quasi-linear approximation, the equation (3.7) is rewritten by

$$-j\omega n_1 + jk\upsilon_{i0} n_1 + \upsilon_{ix} n_0' + jkn_0 \upsilon_{iy} = 0, \tag{3.8}$$

where, $n_0' = \partial n_0 / \partial x$.

Quasi-linearized first order of the continuity equation for the electrons is also derived by the same way as,

$$-j\omega n_1 + \upsilon_{ex} n_0' = 0, \tag{3.9}$$

here, this equation is derived with the relation of υ_{e0}=0 and υ_{ey}=0.

Using Eqs. (3.5), (3.8) and (3.6), (3.9), we have

$$(\omega - k\upsilon_{i0}) n_1 + j\frac{E_{1y}}{B_0} n_0' + jkn_0 \frac{\omega - k\upsilon_{i0}}{\omega_{ci}} \frac{E_{1y}}{B_0} = 0 \tag{3.10 a}$$

$$\frac{E_{1y}}{B_0} = \frac{j\omega n_1}{n_0'}. \tag{3.10 b}$$

Consequently, we have the dispersion relation of the fluctuation by using Eqs. (3.2) and (3.10), as

$$\omega^2 - k\upsilon_{i0}\omega - g\frac{n_0'}{n_0} = 0. \tag{3.11}$$

The solutions are

$$\omega = \frac{1}{2} k\upsilon_{i0} \pm \left[\frac{1}{4} k^2 \upsilon_{i0}^2 + g\frac{n_0'}{n_0} \right]^{1/2}. \tag{3.12}$$

The dispersion relation of the flute mode is shown in Fig. 3.6. This relation

shows that the solution is a real number for $-g n_0'/n_0 < k^2 v_0^2/4$, so that the plasma is convectively stable . In order to excite the flute instability, it is necessary for g and n_0'/n_0 to have an opposite sign mutually, i.e., this condition corresponds to the physical picture that a heavy matter is sustained by a light matter.

In the GAMMA10 plasma, the flute instability may be excited in the frequency around 5 kHz.

Drift wave [37]

The drift mode is introduced by taking account of a finite temperature of the electrons in the inhomogeneous density plasma. Now we consider that a magnetic field $\boldsymbol{B}_0$ is in the z direction, and the plasma density varies along the x direction as shown in Fig. 3.7 (a). We also assume that the temperature of the ions is cold, and that

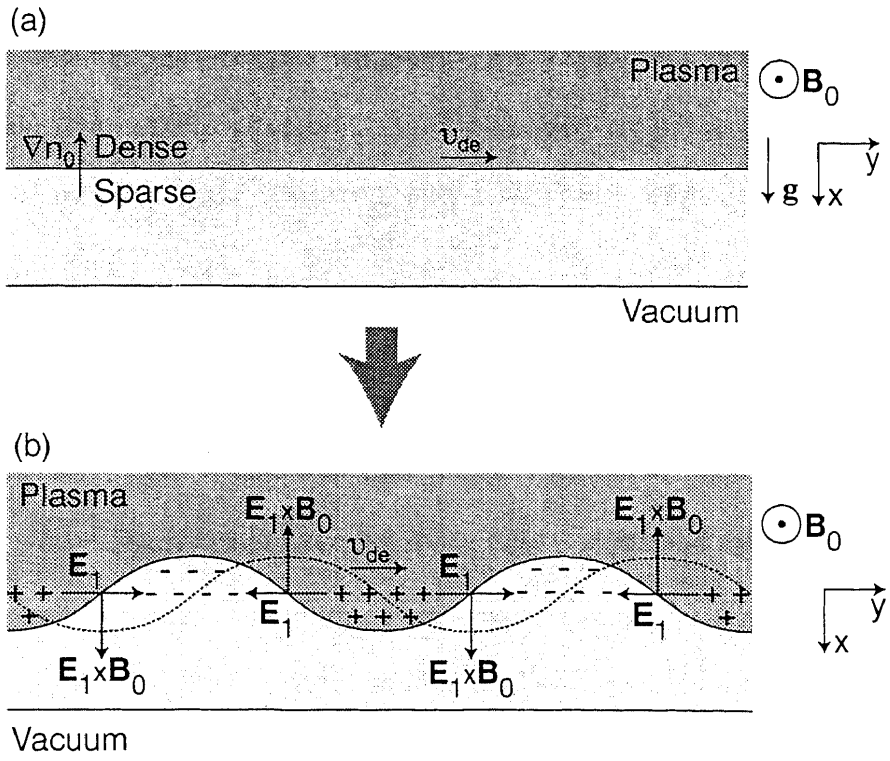

Figure 3.7 Physical mechanism of the drift instability

of the electrons is finite and constant.

In the existence of the density gradient, the electrons move toward to the positive y direction with a velocity of v_{de} due to the diamagnetic drift of the electrons, i.e.,

$$v_{de} = -\frac{k_B T_e}{m_e \omega_{ce} n} \frac{dn}{dx}, \tag{3.13}$$

where T_e is the electron temperature.

This diamagnetic drift velocity causes charge-separation perpendicular to the density gradient. That is, the ions, which has less mobility compared to that of the electrons due to a low temperature, remains in the dense region of the random thermal fluctuations as shown in Fig. 3.7 (b). While, the electrons can run away from the dense region due to the diamagnetic drift, and these are localized in the sparse region of the fluctuation. Thus, the electric field $\boldsymbol{E}_1$ are formed at the nodes of the fluctuation, and the fluctuation propagates toward to the positive y direction due to the $\boldsymbol{E}_1 \times \boldsymbol{B}_0$ force to the ions.

Addition to that, the electrons can also run away from the dense region along the magnetic field with a thermal velocity, so that the density perturbation also propagates along the magnetic field. This instability driven by the density gradient is called drift instability.

Next, we shall derive the dispersion relation of the drift mode classifying into two cases according to a value of the plasma-beta.

(a) Drift wave in the low pressure plasma ($\beta = 2\mu_0 n k_B T / B_0^2 << 1$)

In the low pressure plasma, the magnetic field is assumed to be homogeneous, and we consider less longitudinal phase-velocity of the drift wave compared to the Alfven velocity. In this assumption, the electric field, which makes the drift mode risen, is curl-free, so that it is written by $\boldsymbol{E} = -\nabla\varphi$, where φ is a plasma potential. The electrons can move along the magnetic field freely with the thermal velocity, so that

these attain thermodynamical equilibrium, i.e.,

$$\tilde{n}_e/n = e\varphi/k_B T_e, \tag{3.14}$$

where $\tilde{n}_e$ and n are the perturbed and unperturbed electron density, respectively.

While, the perturbed ion-density $\tilde{n}_i$ can be obtained from the continuity equation as

$$\frac{\partial \tilde{n}_i}{\partial t} + \nabla(n\boldsymbol{v}_i) = 0, \tag{3.15}$$

where $\boldsymbol{v}_i$ is the macroscopic ion velocity, which can be obtained from the equation of motion for the ion. For $\omega << \omega_{ci}$, the solution of the equation is expressed by using quasi-linear approximation as

$$\boldsymbol{v}_{i\perp} = \frac{j}{B_0}[\hat{z} \times \boldsymbol{k}]\varphi \tag{3.16 a}$$

$$v_{iz} = \frac{e}{m_i}\frac{k_z}{\omega}\varphi, \tag{3.16 b}$$

where $\boldsymbol{v}_{i\perp}$ and v_{iz} are the ion velocity perpendicular and parallel to the magnetic field, respectively. By substituting Eqs. (3.16) into Eq. (3.15),and using quasi-linear approximation, we have

$$\frac{\tilde{n}_i}{n} = \left(\frac{\omega^*}{\omega} + \frac{k_z^2 T_e}{m_i \omega^2}\right)\frac{e}{k_B T_e}, \tag{3.17}$$

where

$$\omega^* = \frac{k_B T_e k_y}{m_i \omega_{ci}}\frac{1}{n}\frac{dn}{dx} = \frac{k_B T_e k_y}{m_e \omega_{ce}}\frac{1}{n}\frac{dn}{dx} = v_{de}k_y \tag{3.18}$$

is the drift frequency.

Finally, we have the dispersion relation of the drift instability by using quasi-neutral condition, i.e., $\tilde{n}_i = \tilde{n}_e$, as

$$\omega^2 - \omega^*\omega - c_s^2 k_z^2 = 0, \tag{3.19}$$

where $c_s = (T_e/m_i)^{1/2}$ is the sound velocity.

(b) Drift wave in the high pressure plasma ($\beta = 2\mu_0 n k_B T / B_0^2 >> m_e / m_i$)

Now we consider that the plasma pressure is high, i.e., the ion is not cold, but has a finite temperature which equals to the electron temperature (T_i=T_e). As the electron temperature increases with increasing plasma-beta, the longitudinal phase velocity of the drift mode increases. Now we also consider the case that the longitudinal component of the phase velocity of the mode reaches Alfven velocity c_a. For $\omega/k_z \sim c_a$, the longitudinal electric-field of the mode can not be considered curl-free, so that the magnetic field is bent slightly. In this situation, we introduce a longitudinal potential ψ determined by Poisson formula; $E_z = -\partial\psi/\partial z$, where E_z is a longitudinal component of the electric field. While, we also assume slow oscillation of the mode, so that the transverse component of the electric field is considered to be curl-free. That is, in the same manner to the low-pressure case, we can retain the transverse potential φ; $\boldsymbol{E}_\perp = -\nabla_\perp \varphi$, where the $\boldsymbol{E}_\perp$ is the transverse component of the electric field.

Since the thermal velocity of the electrons considerably exceeds the longitudinal phase velocity, the electrons reach equilibrium along the magnetic field line, i.e.,

$$(\nabla \times \boldsymbol{P})_z + enE_z + en(\boldsymbol{v}_{de} \times \boldsymbol{B})_z = 0, \tag{3.20}$$

where $\boldsymbol{P}$ is the pressure of electrons. Using the quasi-linear approximation and Poisson formula, Eq. (3.20) is rewritten by

$$jk_B k_z \tilde{n}_e T_e - k_B T_e \frac{B_x'}{B_0}\frac{dn}{dx} = jk_z en\psi . \tag{3.21}$$

Where, B_x' is the x-component of the perturbation in the magnetic field due to the effect of magnetic-field bend. This is described by using Faraday's law and quasi-linear approximation, as

$$B_x' = j\frac{k_y k_z}{\omega}(\varphi - \psi). \tag{3.22}$$

By substituting Eq. (3.22) into Eq. (3.21), we have

$$\frac{\tilde{n}_e}{n} = \frac{e}{k_B T_e}\varphi + \frac{e}{k_B T_e}(\psi - \varphi)\left(1 - \frac{\omega^*}{\omega}\right). \tag{3.23}$$

In order to relate φ and ψ, Ampere's law specialized in a low frequency region is used. The z-component of the induced current is written by applying quasi-linear approximation to the law, as

$$j_z = \frac{\varepsilon_0 c^2}{\omega} k_\perp^2 k_z (\varphi - \psi), \tag{3.24}$$

where $k_\perp^2 = k_x^2 + k_y^2$. The z-component of the induced current is also introduced from the relation, $\nabla \cdot \boldsymbol{j} = 0$, in addition to Eq. (3.24). From the relation, we obtain

$$j_z = jk_z^{-1} e \nabla_\perp n(\boldsymbol{v}_{i\perp} - \boldsymbol{v}_{e\perp}). \tag{3.25}$$

The perpendicular components of the ion and the electron velocity are determined by the equation of motion for the ion and the electron. The solutions are

$$\boldsymbol{v}_{i\perp} = \frac{j}{B_0}[\hat{z} \times \boldsymbol{k}]\varphi + \frac{\omega}{B_0 \omega_{ci}} \boldsymbol{k}_\perp \varphi - \frac{jk_B T_i k_\perp^2}{m_i \omega_{ci} B_0}[\hat{z} \times \boldsymbol{k}]\varphi \tag{3.26 a}$$

$$\boldsymbol{v}_{e\perp} = \frac{j}{B_0}[\hat{z} \times \boldsymbol{k}]\varphi, \tag{3.26 b}$$

where the first, second and the third term of the right hand for the ion velocity express the component of the velocity due to $\boldsymbol{E}_1 \times \boldsymbol{B}_0$ force, perpendicular component of the electric field $\boldsymbol{E}_\perp$ and finite ramor radius effect, respectively.

By substituting these solutions into Eq. (3.25), and comparing the longitudinal induced current with Eq. (3.24), we have the relation between φ and ψ, as

$$\varphi - \psi = -\frac{1}{c_A^2 k_z^2}\omega(\omega + \omega^*)\varphi, \tag{3.27}$$

where c_A is the Alfven velocity determined by $c_A = \left(\varepsilon_0 c^2 B_0^2 / n m_i\right)^{1/2}$.

Finally, by substituting Eq. (3.27) into Eq. (3.23), and using quasi-neutral condition, i.e., comparing with Eq. (3.17), and considering the longitudinal wave number is consid-

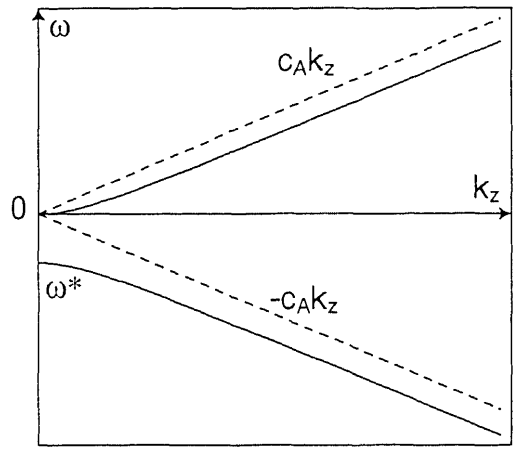

Figure 3.8 Dispersion relation of the drift instability

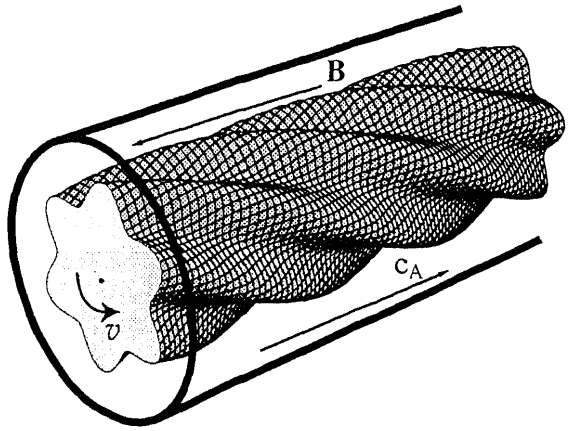

Figure 3.9 Schematic view of the drift instability

erably small, we have the dispersion relation of the electromagnetic drift mode as,

$$\omega^2 + \omega^* \omega - c_A^2 k_z^2 = 0. \tag{3.28}$$

The dispersion relation of the electromagnetic drift wave is shown in Fig. 3.8. As the longitudinal wave number becomes sufficiently small, this mode changes to electrostatic drift mode which oscillates with the frequency of ω^*. Figure 3.9 shows an illustration of the equidensity surface of the drift instability in the cylindrical plasma.

In the GAMMA10 plasma, the drift wave may be excited in the frequency around 10 kHz.

Alfven Ion Cyclotron (AIC) instability [38-40]

The AIC instability is excited in the frequency range of 5.6 ~ 5.9 MHz in the GAMMA10 plasma. This frequency range is associated with 0.85 ~ 0.95 times the ion cyclotron frequency. This instability is excited with increase in anisotropic ion-temperature and plasma-beta. The dispersion relation of the AIC instability is described as

$$D(k,\omega) = k^2 c^2 - \omega^2 + \omega_{pi}^2 \chi_i(k,\omega) = 0, \tag{3.29}$$

where χ_i is the electric susceptibility of the ion which is expressed as follows.

$$\chi_i = \frac{\omega}{\omega - \omega_{ci}} - \left(\frac{\omega}{\omega - \omega_{ci}} + \frac{T_\perp}{T_{//}} \right) Z_1(\zeta), \tag{3.30}$$

where, $Z_1(\zeta)$ is the plasma dispersion function, and ζ is written as the form,

$$\zeta = \frac{W - 1}{\left(\beta_\perp T_{//} / (1 - \beta_\perp) T_\perp \right)^{1/2} kc/\omega_{pi}}. \tag{3.31}$$

Chapter 4

CPS Measurement with Continuous Wave Source

In order to develop magnetic fluctuation measurement system, it is important to confirm that detected signals satisfy CPS process described in Chap. 2. For this reason, we have performed the CPS measurement with continuous wave as a source which has an advantage of fluctuation frequency measurement.

In this chapter, the CPS system along with the reflectometer system and result of these systems are described in Secs. 4-1 and 4-2. And the system with a movable receiver horn for measurement of dispersion relation of the magnetic fluctuation is described in Secs. 4-2 and 4-3. These systems are designed to measure the fluctuation in the range of low frequency (< 200 kHz).

4-1 Homodyne System for CPS and Reflectometer

The schematic of the CPS and the reflectometer diagnostic systems is shown in Fig. 4.1. Figure 4.1 (a) describes the X mode reflectometer and the O→X CPS (O mode injector and X mode receiver). Figure 4.1 (b) describes the X mode reflectometer and the X→O CPS (X mode injector and O mode receiver). They were located at the midplane of the central cell (z=0). These systems utilize a 7-18 GHz, 100-150 mW output of a yttrium-iron-garnet (YIG) oscillator as a source, and the incident

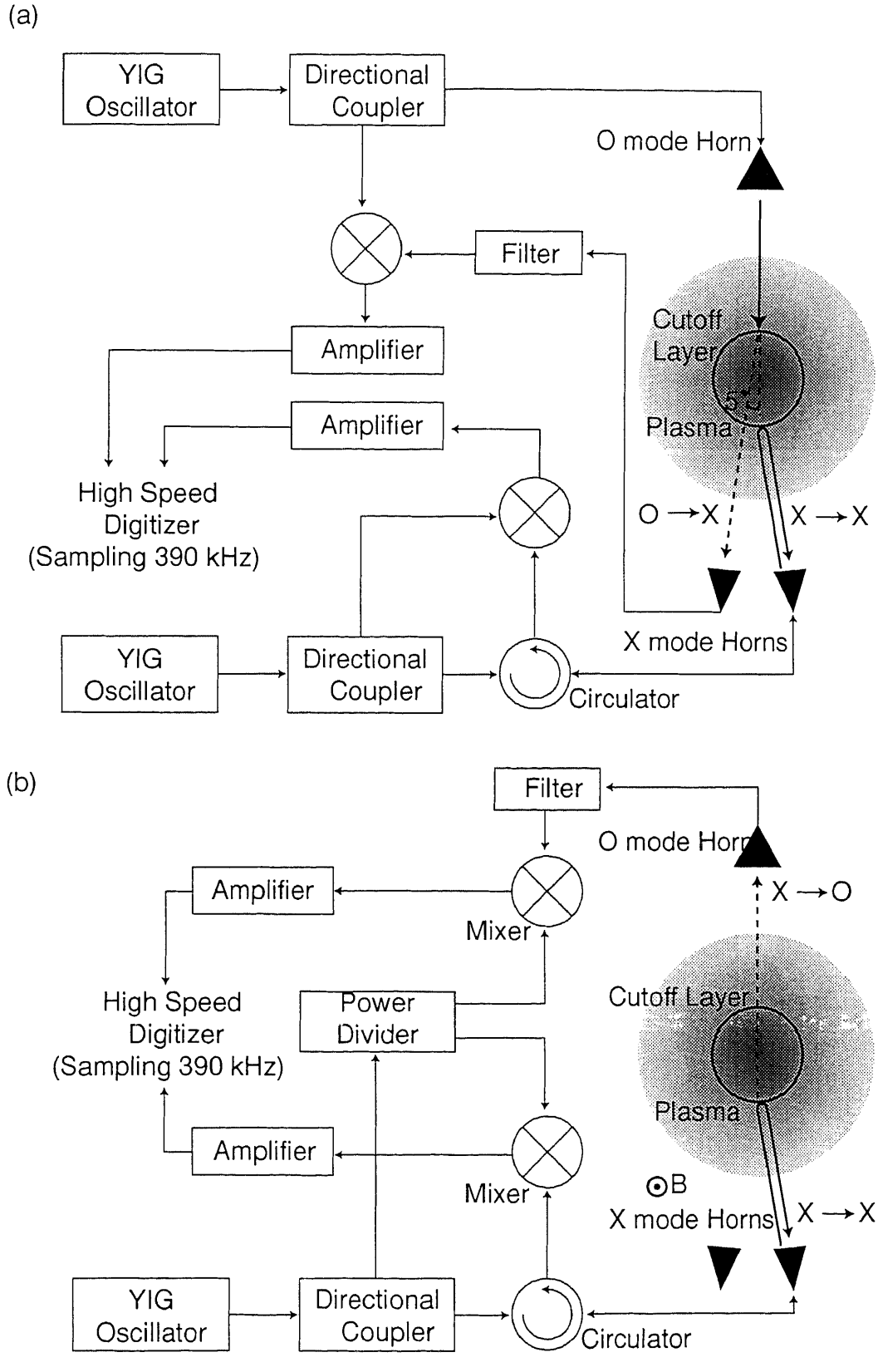

Figure 4.1 Schematic View of O→X CPS and X mode reflectometer system (a), X→O CPS and X mode reflectometer system (b)

wave is fed to a transmitter horn via a waveguide and a coaxial cable. The pyramidal horns with O mode and X mode propagations are installed in the top and bottom ports respectively, and are used as transmitters or receivers. The mode-converted scattered signal and the reflectometer signal are mixed with the local oscillator (LO) wave. The intermediate frequency (IF) signal is amplified by low-noise amplifiers, and fed to high-speed digitizers with 2.5 μs sampling time and 4 MB memory.

The cutoff frequencies of the O and the X mode microwaves are distributed radially as shown in Fig. 4.2 in the typical electron density of the central-cell plasma. In order for the receiver horn to avoid detecting an incident wave directly, a proper frequency is chosen. The incident wave with this frequency encounters the cutoff layer,

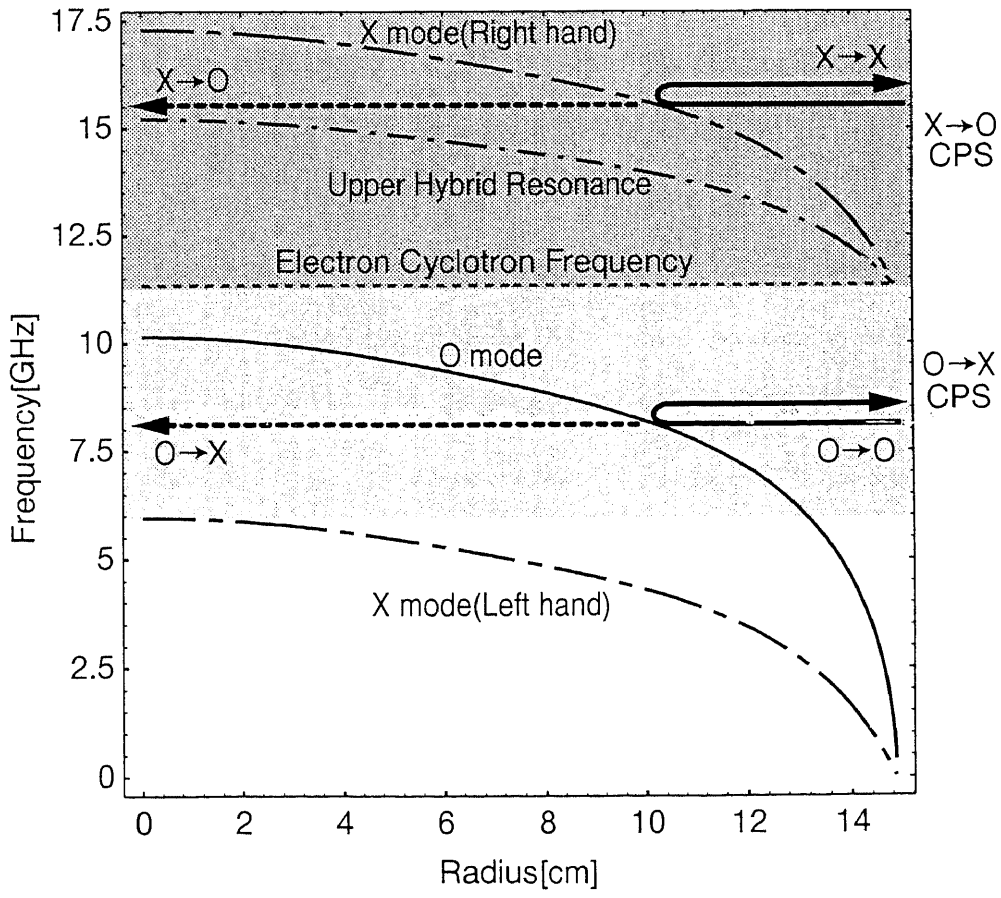

Figure 4.2 Typical cutoff frequencies of Ordinary and Extraordinary modes in the central cell plasma

however the mode converted scattered wave can propagate through the plasma as shown in Fig. 4.2.

4-2 Results and Discussion

The typical plasma parameters in the present experiment are as follows: the line-integrated density is $n_c l_c = 4 \times 10^{13}$ cm^{-2} with an effective diameter of l_c =32 cm, the electron temperature is T_e = 60-100 eV, and the averaged ion temperature is T_i = 4-6 keV. Figure 4.3 shows an example of hot ion modes with the time sequence of the heating system, where the line-integrated density and the diamagnetic-loop signal at the central cell and the CPS signal (O→X) during the time the ECRH power is applied are plotted from top to bottom, respectively. The frequency spectrum of the CPS signal shows that low-frequency waves of less than 100 kHz are strongly excited in a plasma. The time evolution of the frequency spectra is shown in Figs. 4.4 and 4.5. Figure 4.4 corresponds to the O→X mode CPS (incident frequency: 10.2 GHz) and the X-mode reflectometer (14.287 GHz) signals, while the X→O mode CPS (11.46 GHz) and the X-mode reflectometer (11.159 GHz) signals are shown in Fig. 4.5. The incident frequencies are chosen so that both systems observe similar radial positions of the plasma at the same time. It is apparent that the intensity and the spectrum of the fluctuations change after the application of the barrier-ECRH, indicating the modification of the radial electric field due to the potential formation. It is noted that the frequency spectra of the CPS signals are broader than that of the reflectometer signal.

The discrepancy of the spectra between the CPS and the reflectometer signals can be explained as follows. The refractive indexes of the O-mode and the X-mode propagations are given by Eqs. (2.22), (2.23), as

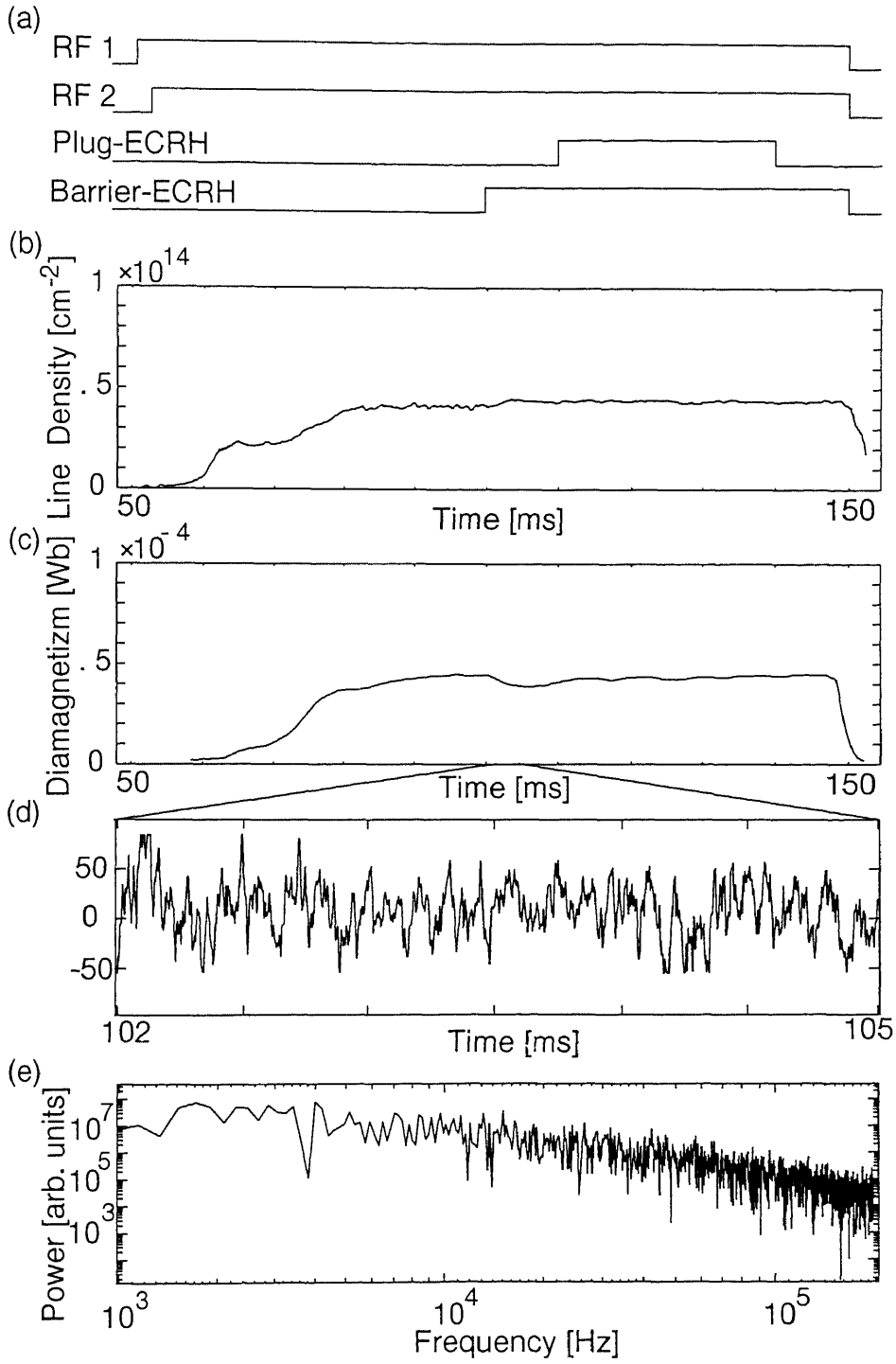

Figure 4.3 (a) Time sequences of the heating systems, (b) line integrated density, (c) diamagnetic loop signal, (d) CPS signal, and (e) power spectrum of the CPS signal .

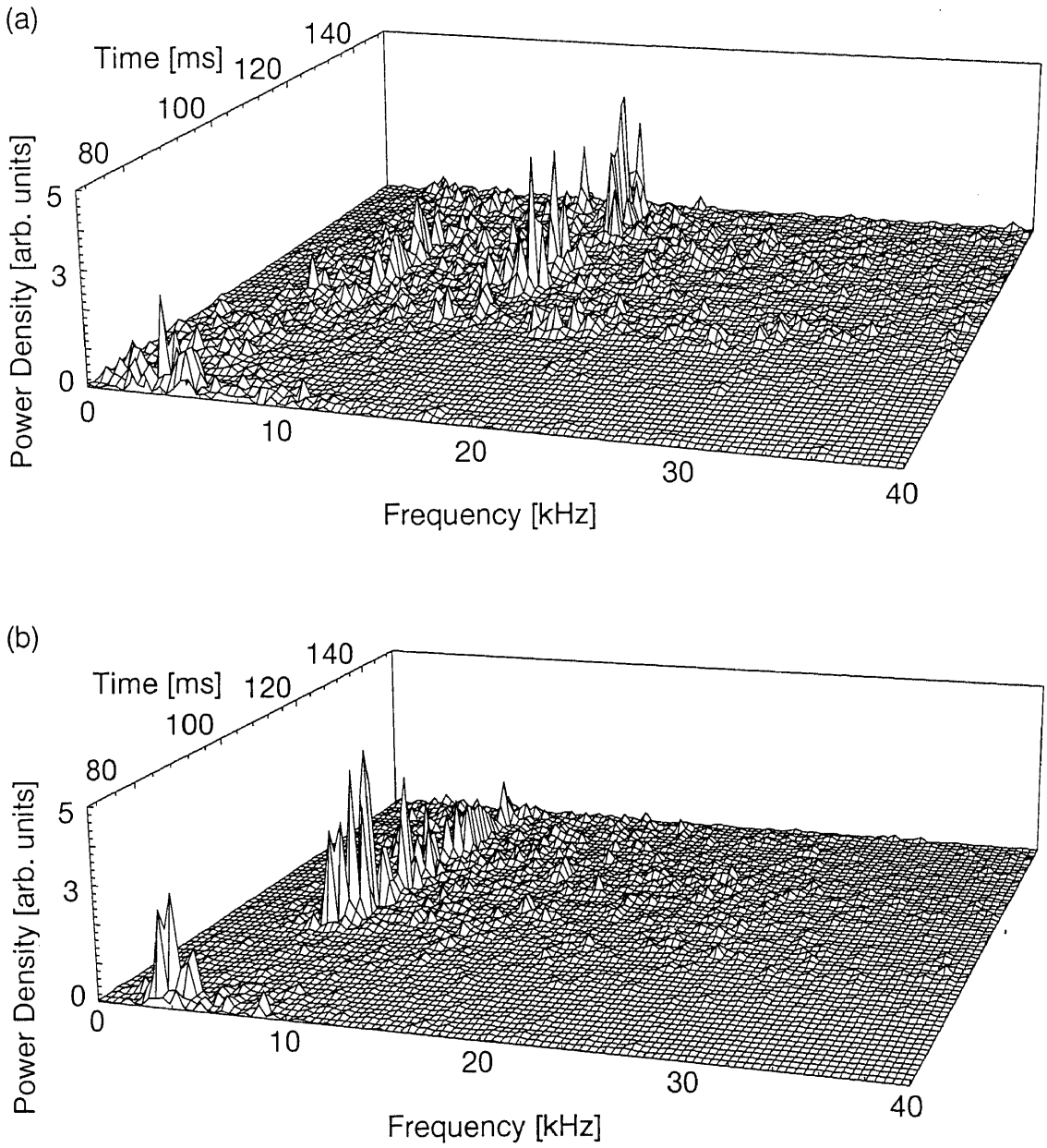

Figure 4.4 Power spectral density of CPS (O→X) signal (top) and reflectometer (X→X) signal (bottom)

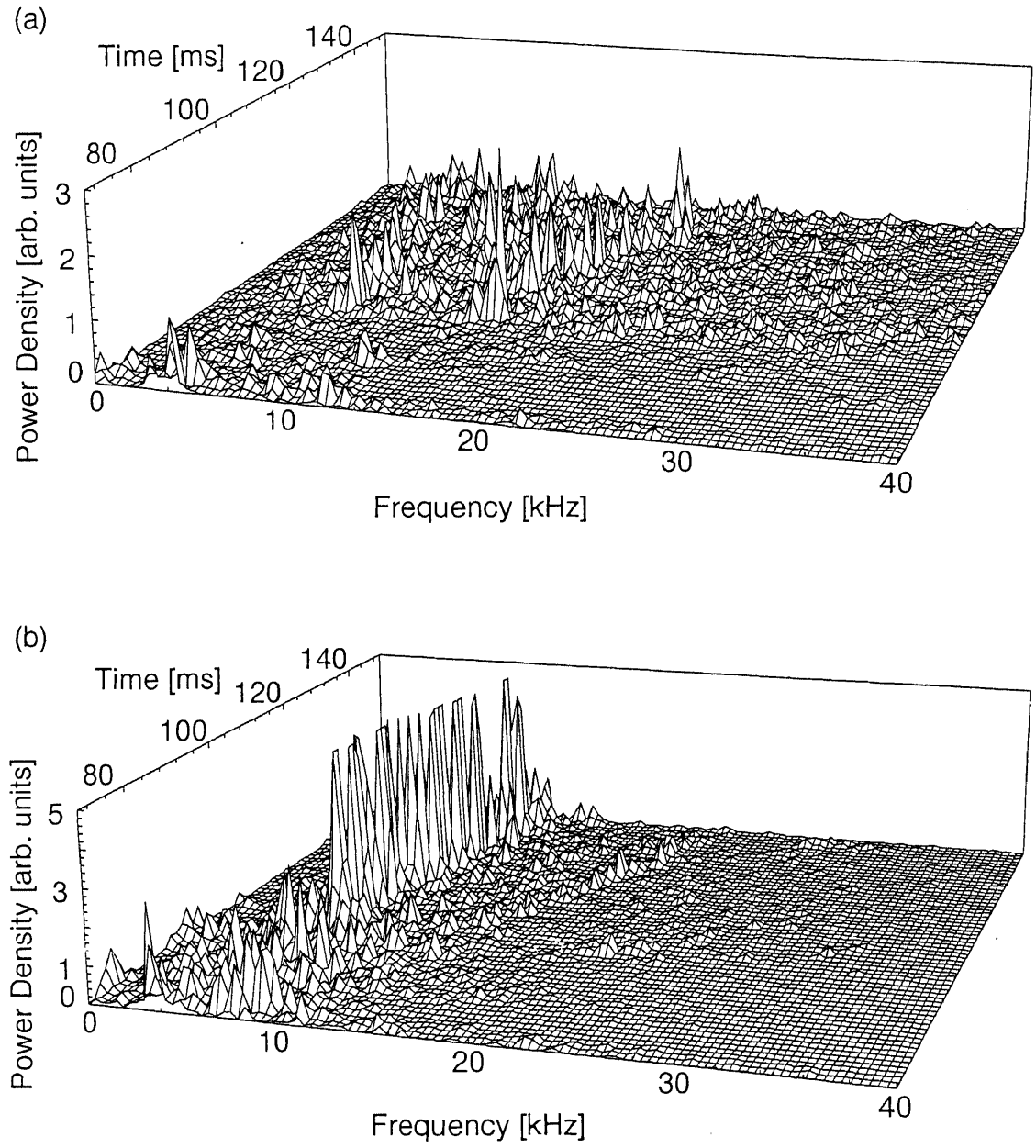

Figure 4.5 Power spectral density of CPS (X→O) signal (top) and reflectometer (X→X) signal (bottom)

$$N_O = \frac{ck_O}{\omega} = \left(1 - \frac{\omega_{pe}^2}{\omega^2}\right)^{1/2}, \tag{4.1}$$

and

$$N_X = \frac{ck_X}{\omega} = \left(1 - \frac{\omega_{pe}^2}{\omega^2} \cdot \frac{\omega^2 - \omega_{pe}^2}{\omega^2 - \omega_{pe}^2 - \omega_{ce}^2}\right)^{1/2} \tag{4.2}$$

in the cold plasma approximation, where ω_{pe} and ω_{ce} are the electron plasma frequency and the electron cyclotron frequency, respectively.

In the CPS process, the incident O (X) wave is converted to the X (O) wave by magnetic fluctuations until it reaches the cutoff layer of the plasma. The scattering process satisfies the wave number matching condition $\boldsymbol{k} = \boldsymbol{k}_i - \boldsymbol{k}_s$, where $\boldsymbol{k}$, $\boldsymbol{k}_i$ and $\boldsymbol{k}_s$ are the wave-number vectors of the fluctuation, the incident wave and the scattered wave, respectively. Therefore, $k \cong 0$ in the transparent region of the plasma, since the scattering angle $\theta_s \cong 0$ for the present system and $k = 2k_i \sin(\theta_s/2)$, where $k_i \cong k_s$ is close to the wave number in the vacuum. At the cutoff region in the O→X process, the wave number of the incident wave, k_O becomes 0 according to Eq. (4.1). However, that of the mode-converted X wave, k_s becomes ω/c according to Eq. (4.2). In the X→O process, the wave number of the mode-converted O wave, k_s becomes (0.8-1) ω/c at the cutoff region according to Eqs. (4.1) and (4.2) in the same manner. As a result, k varies from 0 to k_i for the O→X process and from 0 to (0.8-1)k_i for the X→O process. On the other hand, the reflectometer always gives $k \cong 0$, since the wave numbers of the incident wave and the scattered wave equal to 0 at the cutoff layer. Since the frequency of the fluctuation is usually given by the relation $\omega = k v_p$, where v_p is the phase velocity of the wave, we could observe the higher frequency by the CPS measurement. The phase velocity of the fluctuations determined from the observed spectra, $v_p \cong 3\text{km/s}$ is in agreement with $|v_d - v_r| = 2 - 5\text{km/s}$ using the

present experimental conditions, where $v_d \cong T_e/eBL_n = 1-4\text{km/s}$ is the drift velocity, $v_r = E/B \cong 6\text{km/s}$ is the $E \times B$ rotation velocity, e is the charge of an electron, L_n is the density scale length, and E is the radial electric field of the central cell plasma. The magnetic field fluctuations may have a significant influence in the drift-wave mode due to the finite-β effect and the shearless magnetic field of a tandem mirror, i.e., $\left(4\pi n_e T_e/B^2\right)\left(L_s^2/L_n^2\right) > 1$, where L_s is the shear length of the magnetic field [41].

It is seen in Figs. 4.4 and 4.5 that the spectrum of the X→O signal has a higher frequency than that of the O→X signal. This may be explained due to the difference of the scattering region. The O→X scattering occurs in the core plasma region, while the X→O scattering occurs in the edge region where the larger value for phase velocity can be expected.

4-3 Homodyne System for Movable Receiver

A schematic view of the CPS system is shown in Fig. 4.6. It is also located at the midplane of the central-cell (z=0 m). Pyramidal horns attached to the horizontal port and the bottom port are used to inject the incident microwave power in X mode. Two pyramidal horns attached to the top port are used to receive the scattered power in O mode. The receiver horns can observe the signals with various scattering angles by using an optical rail and rotary stages. The system utilizes a 7-18 GHz, 100-150mW output of a YIG oscillator as a source. The CPS signals picked up by the receiver horns are detected by homodyne systems. The resultant intermediate frequencies (IF) are amplified by low-noise amplifiers, and fed to high-speed digitizers with 0.5 μs or 20 ns sampling time and 4 MB memory. In the present experiment the frequency of the oscillator is fixed during a plasma shot.

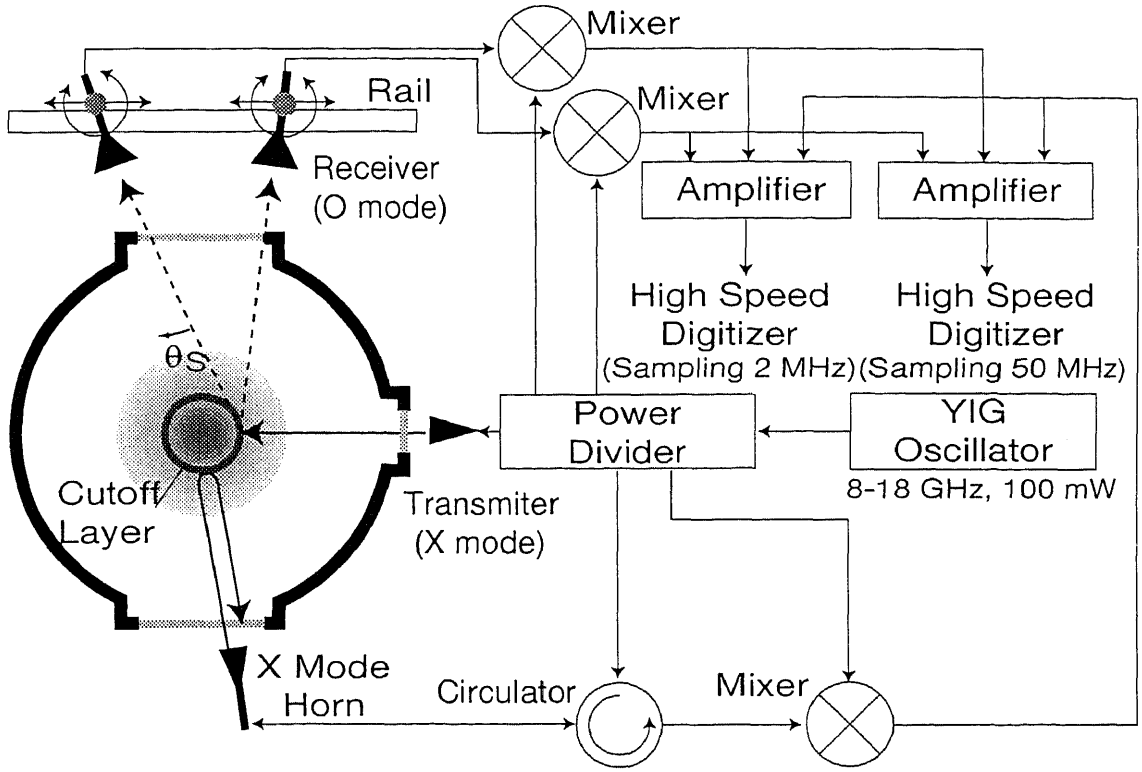

Figure 4.6 Schematic view of the scaning CPS and reflectometer

4-4 Results and Discussion

Dispersion relation of the low-frequency waves

Figure 4.7 shows the time evolutions of the diamagnetizm, line-integrated density at the central-cell, and an example of the CPS signal and the time sequence of the heating systems. The power spectra of the CPS signal for various scattering angles are also shown in Fig. 4.7. The scattering angle θ_s of the receiver horn is measured from the vertical axis at the cutoff point of the incident wave frequency as shown in Fig. 4.6, since the scattering cross section attains the maximum value at the cutoff layer. It is seen that the power spectrum of the CPS signal broadens with an increase in the scattering angle. The peak frequency is plotted against the scattering angle in Fig. 4.8 (a). The frequency seems to be proportional to the scattering angle, although

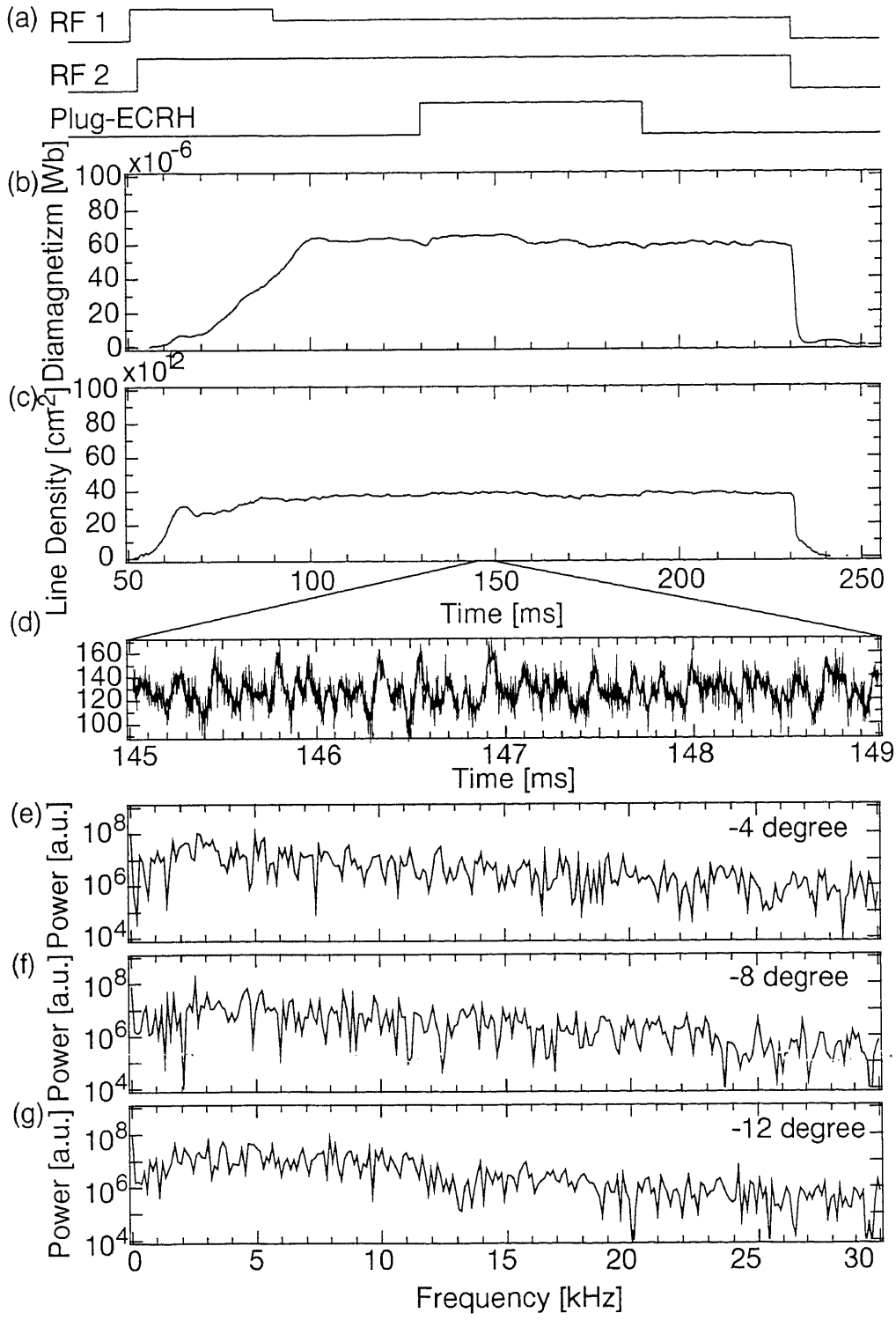

Figure 4.7 Time evolution of the plasma parameters at the central cell: (a) time sequence of the heating systems, (b) diamagnetic-loop signal, (c) line-integrated density, and (d) CPS signal, Frequency spectra of the CPS signal for various scattering angles (-4, -8, -12 degree) are shown in the bottom figure.

the dependence on the positive scattering angle shows a deviation from linear relationship between k and ω at large scattering angle. This deviation is considered to be occurred due to mixing of the reflected wave along with the CPS signal. That is, the lower frequency is estimated by the reflected wave which has no wave-number resolution in the same manner to Sec. 4-2. The k-ω spectrum, i.e., the dispersion relation of the fluctuations is shown in Fig. 4.8 (b). The wave numbers of the fluctuations are calculated from the matching condition

$$k = k_s - k_i \ , \tag{4.3}$$

where k , k_s, and k_i are the wave number vectors of the fluctuations, the scattered wave, and the incident wave, respectively. Here, the wave number of the incident wave is assumed to be zero, since the CPS process occurs mainly near the cutoff layer.

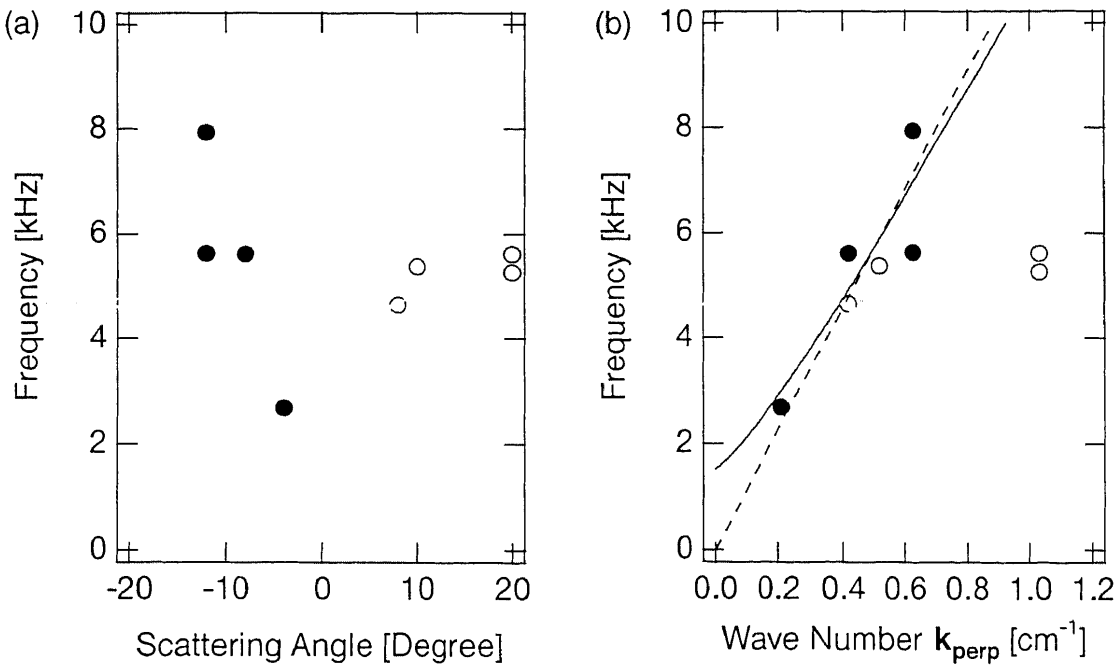

Figure 4.8 (a) Dependence between the peak frequency and the scattering angle.
(b) Dispersion relation of the magnetic fluctuation.

The wave number of the fluctuations can be divided into two components, azimuthal component ($k_\theta = k_s \sin\theta$) and radial one ($k_r = k_s \cos\theta$). In Fig. 4.8 (b), the horizontal axis shows the azimuthal component of the wave number. The dispersion relation is given by

$$\omega^2 + \omega^* \omega - c_A^2 k_z^2 = 0. \tag{4.4}$$

A solid line seems to agree with the electromagnetic drift wave Doppler shifted by the $\boldsymbol{E} \times \boldsymbol{B}$ rotation velocity. In the present stage, it is difficult to distinguish the mode of the magnetic fluctuation. Note that the clear dependence of the peak frequency on the scattering angle is not observed in the edge plasma region. It is considered that the radial component of the wave number is dominant in the edge plasma region.

Coupling between the ICRF modes and the low frequency waves

The simultaneous measurements of the CPS and the reflectometry are performed with the setup shown in Fig. 4.6, where a horn attached to the bottom port is used as a receiver of the reflectometer as well as a transmitter of the CPS and the reflectometer. The reflected wave is separated from the incident wave by a circulator, and is mixed with the unpertubed LO wave in a mixer. Figure 4.9 shows the time sequence of the heating systems, the diamagnetizm, and the line-integrated density of the central-cell plasma from top to bottom. The RF2 power is further increased during the time of 130-180 ms, while the ECRH power is not applied. The time evolution of the frequency spectrum of the CPS signal is shown in Fig. 4.10 for two frequency regimes. In Fig. 4.10(b) the peak at 6.36 MHz corresponds to the RF2-driven wave. The spectrum around 5.7 MHz can be observed when the diamagnetic signal attains a certain level. Several discrete peaks are observed in this mode. The instability was identified as the Alfven ion cyclotron (AIC) mode. The increase of plasma beta and ion tem-

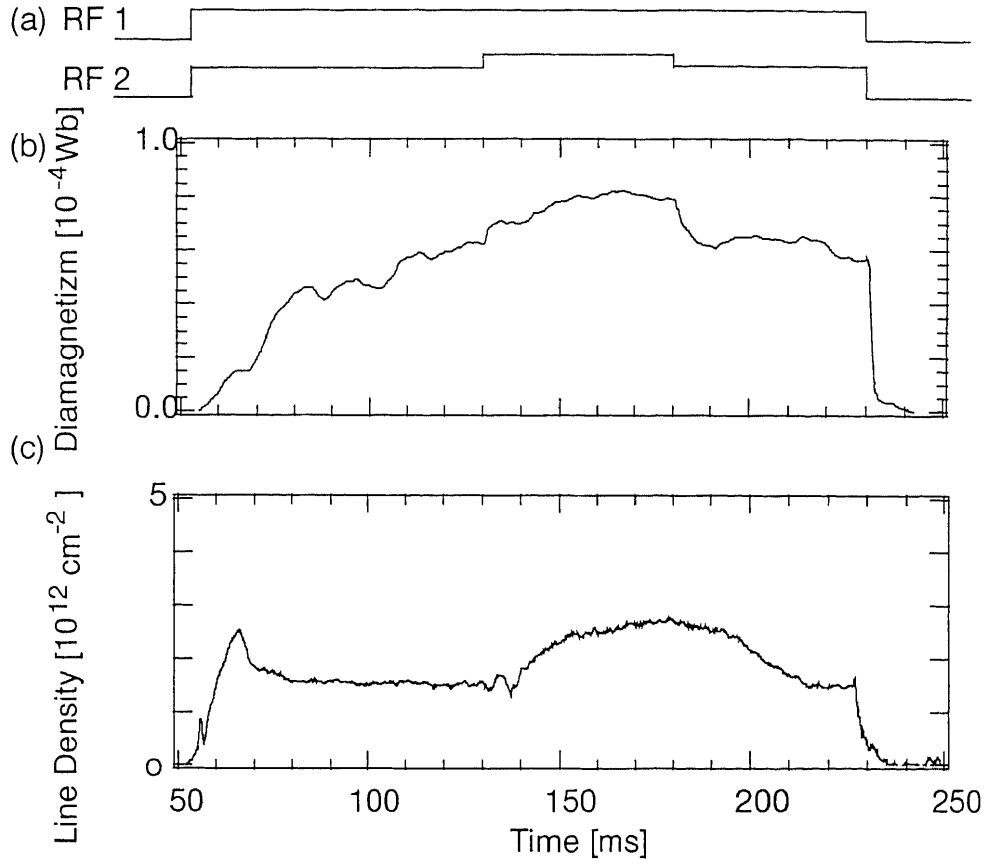

Figure 4.9 The sequences of the heating systems are shown in the top figure, and time evolution of the diamagnetic loop signal (a) and the line-integrated density (c).

perature anisotropy produce the instability. The AIC mode is the eigenmode determined by the axial boundary conditions, which causes the discrete peaks in the frequency range of $\omega \cong 0.9\omega_{ci}$, where ω_{ci} is the ion cyclotron frequency. When the additional RF2 power is applied at 130 ms, the low frequency fluctuations start to grow with increase in the AIC modes. The frequency spectra of the CPS and the reflectometer signals at 145 ms are shown in Fig. 4.11 for two frequency regimes. The peak at 70 kHz in the low frequency regime agrees with the frequency difference between two peaks observed in the high frequency regime, that is, two discrete AIC modes around 5.7 MHz. It is noted that the peak power at 70 kHz observed in the CPS signal is about 3 times larger than that observed in the reflectometer signal, while the

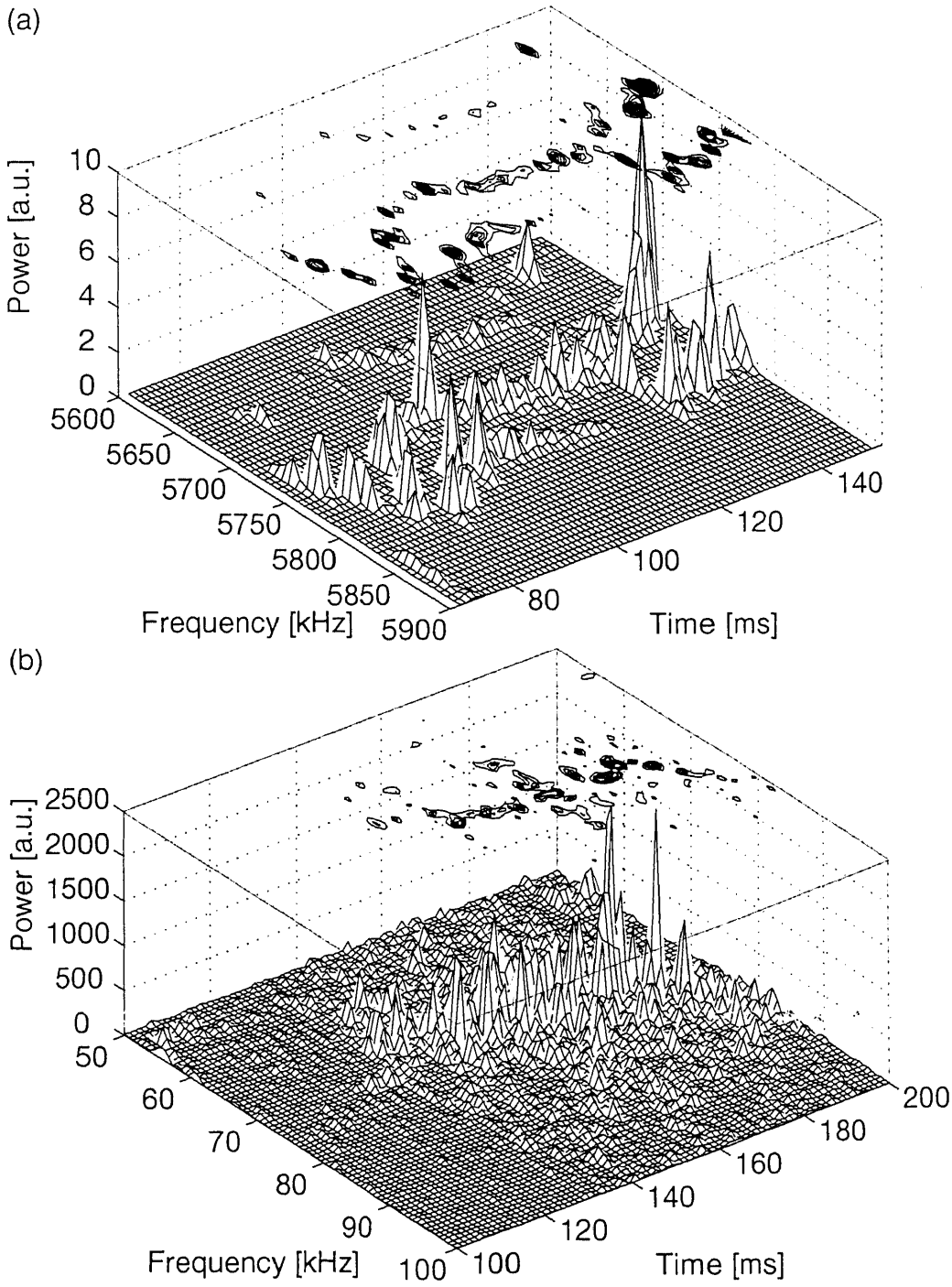

Figure 4.10 Time evolution of the frequency spectra of the CPS (X→O) signal in the high-frequency regime (top) and low-frequency regime (bottom).

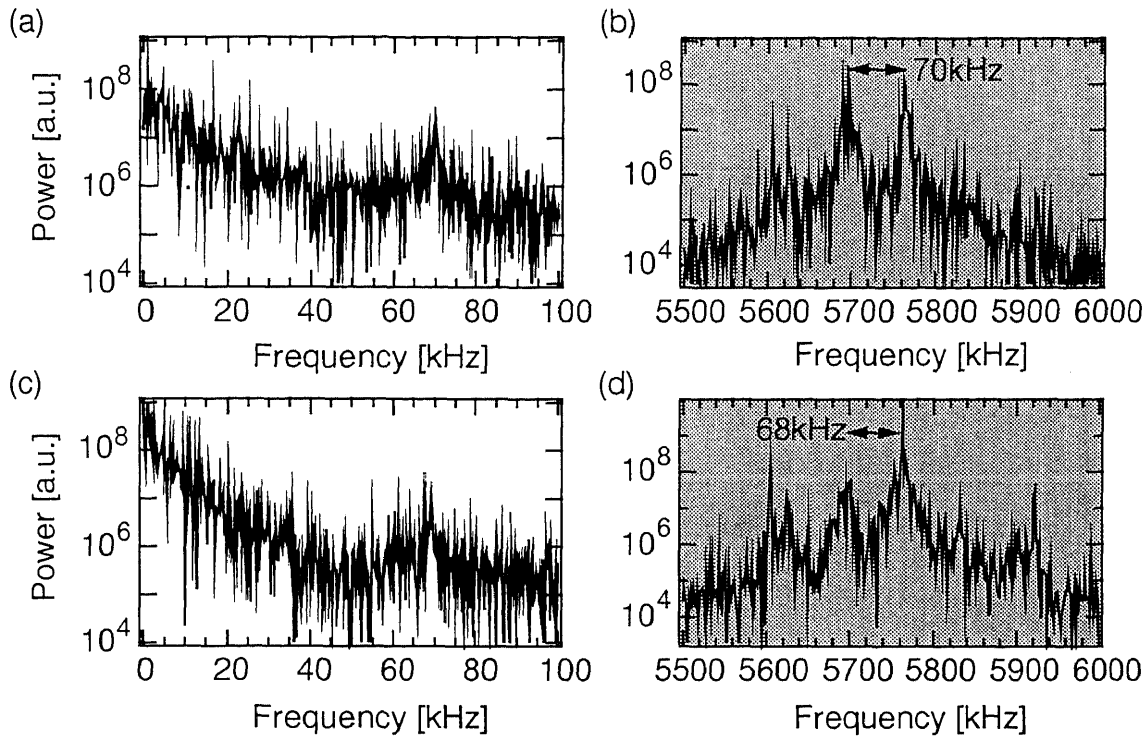

Figure 4.11 Frequency spectra of the CPS signal (a, b) and the reflectometer signal (c, d) at 145 ms.

power below 40 kHz in the CPS signal is smaller than that in the reflectometer signal. The fluctuations around 70 kHz is considered to be the electromagnetic waves excited due to the nonlinear coupling between the discrete modes of the electromagnetic AIC wave. This may cause the saturation of the diamagnetism at the central cell plasma.

4-5 Summary

In summary, the cross-polarization scattering diagnostic technique with frequency of 8-18 GHz was applied to the central-cell plasma of the GAMMA 10 tandem mirror for measurement of electromagnetic plasma waves in the low-frequency region. The CPS process is identified by comparing the frequency spectra between the CPS and

the reflectometer signals. The CPS signals (both O→X and X→O scattering) exhibit broader frequency spectra than those of the reflectometer signals, which is considered to be satisfaction of the wave number matching condition.

Addition to that, the k-ω spectra of the low frequency waves (<40 kHz) are obtained from the angular distribution of the scattered waves. From the ridge of the k-ω spectra the dispersion relation of the electromagnetic drift wave Doppler shifted by the $E \times B$ rotation velocity is considered to be confirmed. The CPS method also observe the low frequency fluctuations (~70 kHz) at the same time with the observation of the Alfven ion cyclotron (AIC) waves (~5.7 MHz). As the plasma beta value and temperature anisotropy increase, the amplitude of AIC mode becomes large, and the discrete modes appear. The adjacent AIC modes couple to excite another low-frequency waves which may cause the saturation of the plasma beta. These are considered to be the signature of the magnetic fluctuation measured using this method.

Chapter 5

Systems for CPS Measurement with Ultrashort-Pulse Wave Source

An ultrashort-pulse microwaves is useful as a probe beam due to having broad band frequency. It can diagnose spatial profile of plasma parameters without sweeping the frequency of the probe beam [42, 43]. Addition to that, since it is considered that the pulse height of the scattered wave by magnetic fluctuation is accurately proportional to the amplitude of the magnetic fluctuation, a CPS measurement system which utilizes the ultrashort-pulse has an advantage of estimating the fluctuation amplitude compared to the CW system.

In this chapter, the relation between the amplitude of the magnetic fluctuation and the height of the scattered impulse is clarified by the numerical simulation of the CPS process. The absolute value of the magnetic fluctuation in the central cell plasma is estimated by comparing between experimental results and simulation results.

5-1 Simulation of Cross-Polarization Scattering Process

We have performed a numerical simulation of electromagnetic wave propagation taking into account the CPS process using frequency dependent finite difference time domain ($(FD)^2TD$) method [44, 45] in order to investigate the relationship between the fluctuation amplitude and the scattered electric field quantitatively. The FDTD technique

for the analysis of interactions of electromagnetic wave with material bodies was formulated by Yee for nondispersive media more than 30 years ago [46]. Recently, $(FD)^2TD$ formulation has been developed, which allows explicit calculation of wide band transient electromagnetic interactions with frequency dependent materials. In the following section, we will describe about the simulation model of the $(FD)^2TD$ method. The details of the derivation of the CPS process with $(FD)^2TD$ notation is described in Appendix A.

Simulation Model

The simulation is a three-dimensional problem which has a width of 0.05 m (x direction), height of 0.25 m (y direction) and depth of 0.25 m (z direction) as shown in Fig. 5.1. The parameters used for the $(FD)^2TD$ calculations are cell size $\Delta x = \Delta y = \Delta z = 2.5$ mm, time step size $\Delta t = 4.5$ ps, number of cells Nx=20, Ny=100, Nz=100, and number of time steps =250. The electron density is almost zero in the region of $y < 0.125$ m, and it has a constant value varying from 0 to 2×10^{12} cm^{-3} in the region of $y > 0.125$ m. The external magnetic flux density in the z direction is 0.405 T in the whole of the computation space. The incident wave used in the $(FD)^2TD$ is a plane Gaussian impulse amplitude-modulated

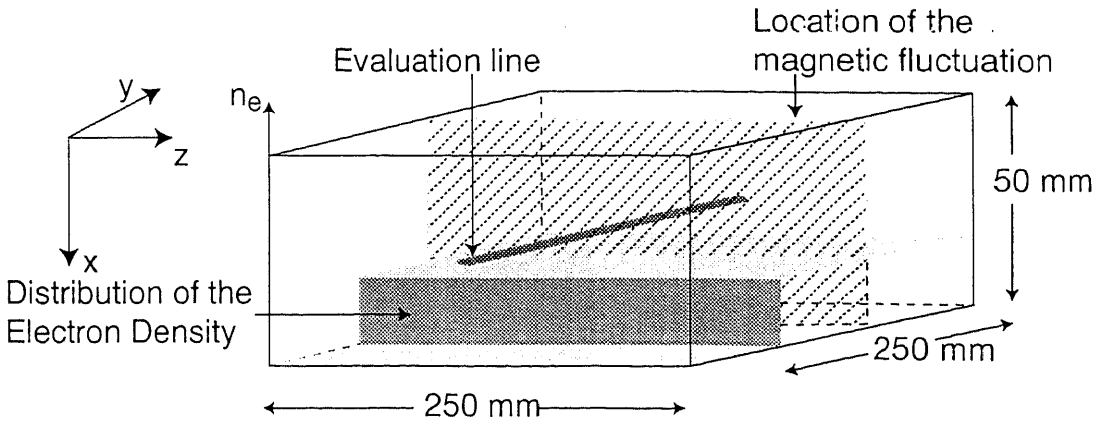

Figure 5.1 Computational space of the simulation and electron density distribution and evaluation line used in the simulation

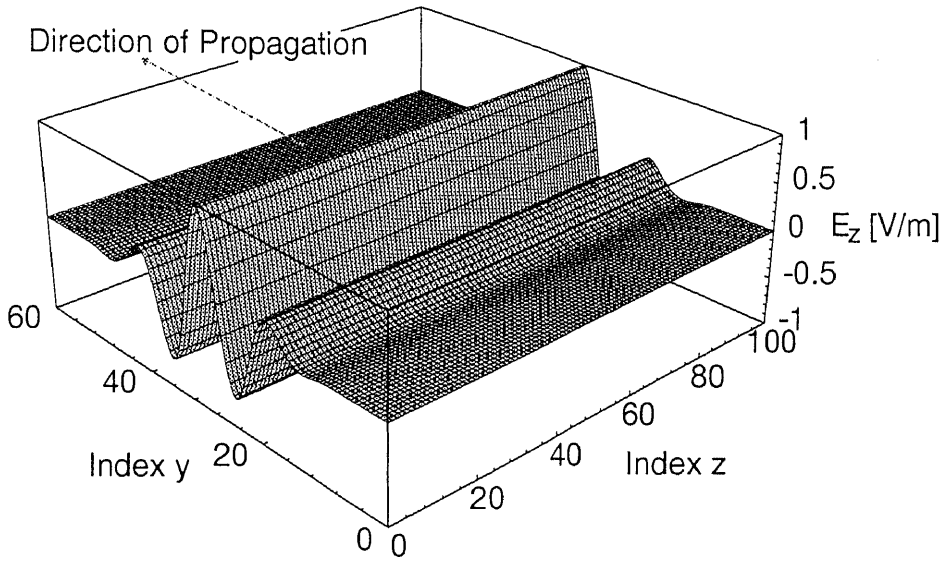

Figure 5.2 Schematic view of the initial electric field in O mode

with a sinusoidal wave which has a frequency of 10 GHz and amplitude of 1 V/m illustrated in Fig. 5.2. The same initial electric fields are given in the z-y plane at each x index. The polarization of the incident wave is O mode (z-polarized). Initial magnetic field in the x direction is also set up in order for the pulse wave propagates to the positive y direction. On the x-y plane at z=0 and z=100, 2nd Liao [47] , which is a name of a boundary condition, is used in order that the electromagnetic waves pass through the boundary without reflection. The Amplitude of the magnetic fluctuation and the electron density are variables in this calculation, and location of the magnetic fluctuation in the x direction is fixed on the x-z cross section at y=187.5 mm.

5-2 Simulation Results and Discussion

The distribution of electron density and the propagation of incident wave in the O mode (Ez) and scattered wave in the X mode (Ex) induced by the CPS process are demon-

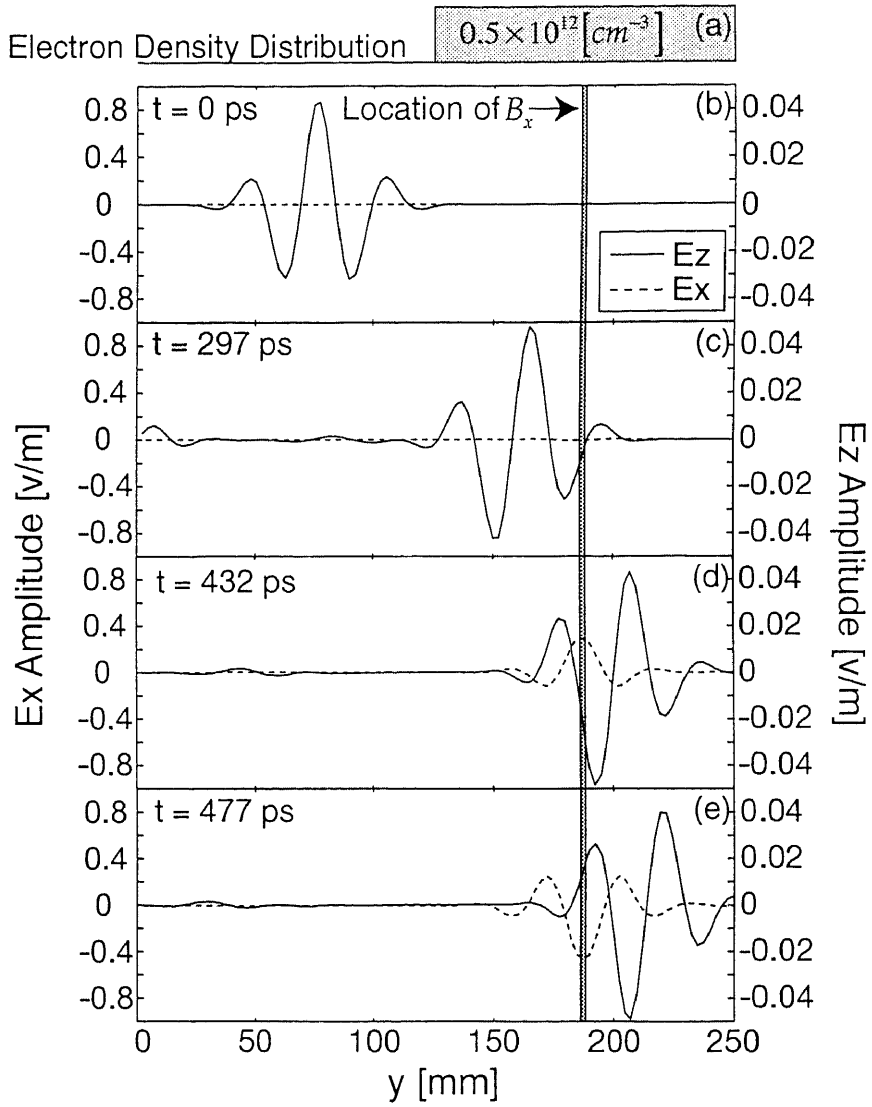

Figure 5.3 Distribution of electron density (a), and propagation of incident (full curve) and scattered (broken curve) waves at t = 0 ps (b), 297 ps (c), 432 ps (d) and 477 ps (e).

strated after several time steps in Fig. 5.3. The magnetic fluctuation is located at $y = 0.1875$ m with amplitude of $\tilde{B}_x/B_0 = 10\%$, where the electron density is $0.5\text{x}10^{12}$ cm^{-3}. The incident wave passes through the plasma with little attenuation because of the low density, however, several percent of the incident wave is reflected at the edge of the plasma due to the difference in wave impedance between vacuum and the plasma. The reflected wave

propagates toward the negative direction at t = 297 ps. While, the scattered wave is induced when the incident wave passes through the plasma with magnetic fluctuations (t =432 ps). Then the induced scattered wave propagates into both positive and negative y directions (t = 477 ps).

The ratio of electric field between the scattered wave and the incident wave at the scattering point is plotted as a function of the electron density normalized by the cutoff density in Fig. 5.4. In this calculation, the amplitude of magnetic fluctuation is fixed at 0.0405 T (10%). The amplitude of the scattered wave increases with an increase in the electron density of the scattering point, that is, each element of the conductivity tensor contained in the induced current of the CPS increases due to the increment of electron plasma frequency. While, the mode-converted scattered wave does not induced in the case that the magnetic fluctuation in the z direction is in the same location. This is due to the

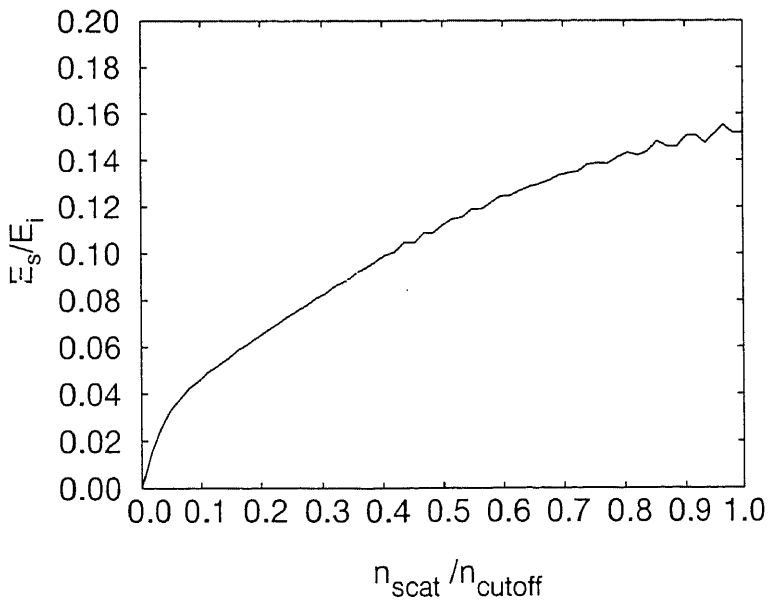

Figure 5.4 The ratio of the amplitude of the scattered wave to that of the incident wave as a function of the electron density at the position where the magnetic fluctuations exist.
The density is nomalized by the cut-off density of the incident wave.

same direction of the incident electric field and the magnetic fluctuation vectors.

The relationship between the electric field of the scattered wave and the magnetic fluctuation level is shown in Fig. 5.5. In this calculation, the electron density is fixed at 0.1×10^{12} cm^{-3}. Amplitude of the scattered wave is exactly proportional to the normalized magnetic fluctuation level, and the gradient of this line is 0.152. This is explained that the induced current of the CPS is proportional to the amplitude of the magnetic fluctuation indicated in Eq. (2.32). Since the incident wave propagates in two-dimensions, and the cutoff layer of the plasmas is not flat in actual experiments, it is considered that the mode conversion rate is lower than this simulation.

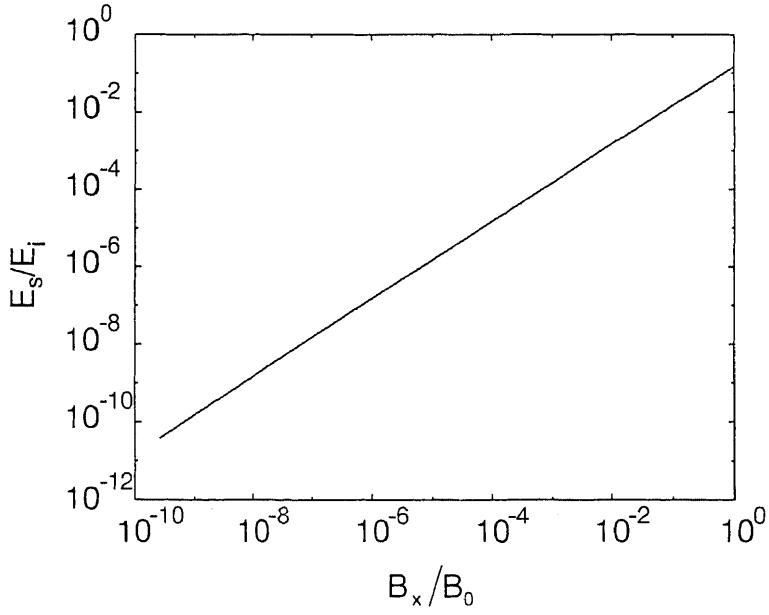

Figure 5.5 Dependence of the conversion efficiency on the nomalized magnetic fluctuation level

5-3 System for Measurement of CPS Using Ultrashort Pulse Microwaves

The schematic view of the ultrashort pulse-utilized CPS measurement system is shown in Fig. 5.6. This system is also located at the midplane of the central cell (z=0 m). A microwave source is a Picosecond Pulse Labs, Model 3500D Impulse Generator, which generates a voltage impulse with an 8V amplitude and a full-width at half maximum (FWHM) of 65 ps, into a 50 Ω load at a repetition rate of 1 MHz. The amplitude of the impulse can be adjusted by an attenuator switch attached to the impulse generator. The attenuation varies from 0 to 81 dB. In the present experiment, the attenuation is fixed at 15 dB. The impulse is at first fed through a 30 cm section of WRD750 waveguide (7-18 GHz pass band) which attenuates the low-frequency portion of the Fourier conponent and chirps the signal. The chirped signal is then amplified by a 40 dB, 6-18 GHz low-noise amplifier, and band-pass filtered using an interdigital-type band-pass filter. A range of filters is available with center frequencies from 8 to 11 GHz at 1 GHz intervals and 3 dB relative bandwidth of 3% of the center frequency. For the present experiment, band-pass filters at 7, 8, 10, 11 GHz were used. The band-pass filtered signal is then amplified by a 40 dB, 6-18 GHz low noise amplifier (DBS Microwave, DBL-0618N720), and fed to transmitter horn in the O mode located at the bottom port. In order to eliminate the X mode component of the transmitter wave due to the mode contamination of the horn, the polarizer which attenuates the X mode wave with 40 dB is used in front of the transmitter. The impulse is then injected into the plasma via a teflon optical lens.

In the receiver section, the mode-converted impulse due to the CPS process and multireflection by the chamber wall are detected by the receiver horn in the X mode via a

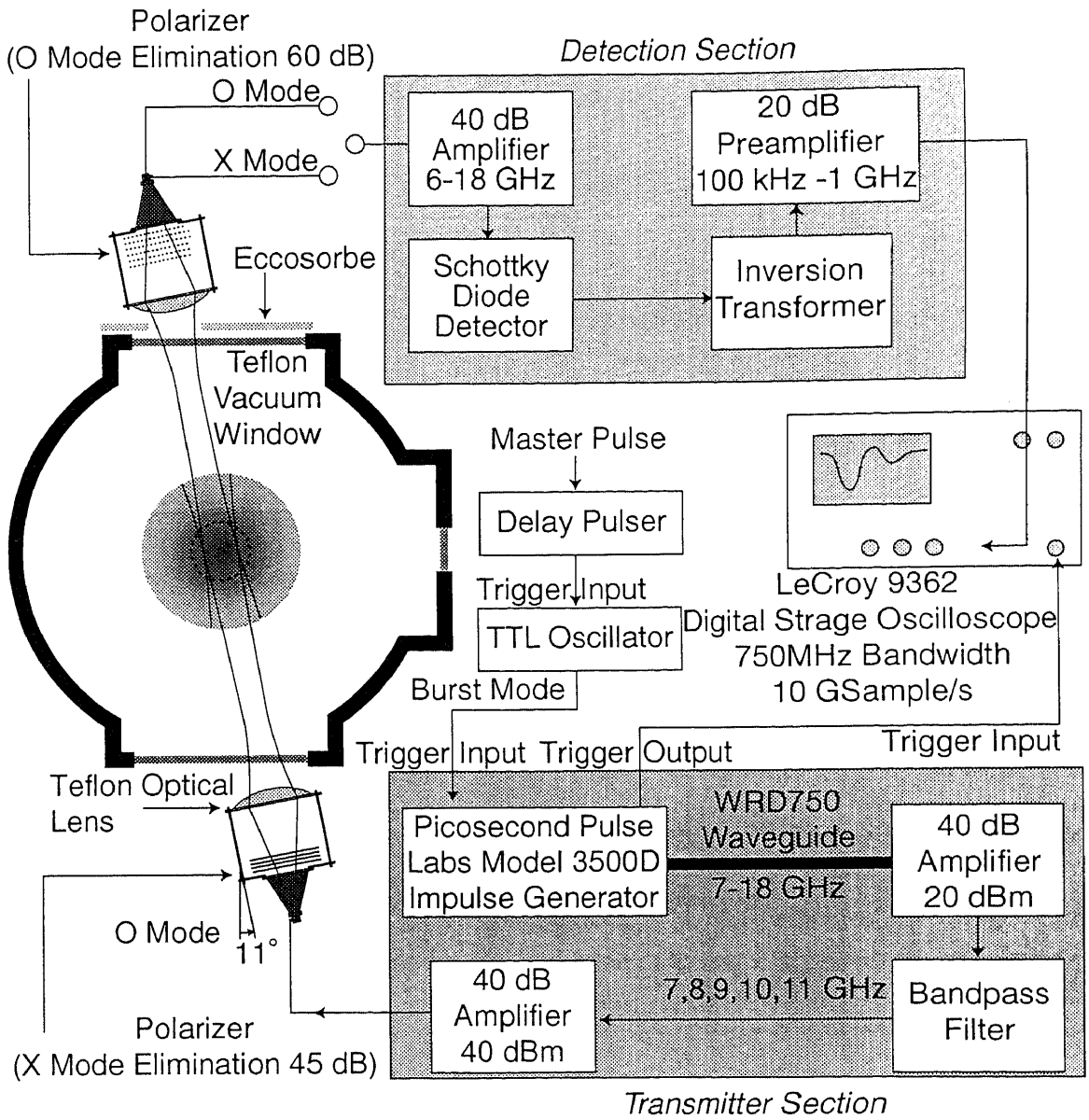

Figure 5.6 Schematic View of the magnetic fluctuation-induced impulse measurement system

the teflon optical lens located at the top port. Eccosorbs and a polarizer which attenuate the O-mode wave with 60 dB are used in front of the optical lens and the receiver horn, respectively. These are used in order to eliminate multi-reflected signal having much higher amplitude compared to the scattered wave by the magnetic fluctuations. The received wave is first amplified by the 40 dB gain amplifier, and detected by a Schottky barrier diode detector. The square-law detected signal is amplified and fed to a digital oscilloscope with 10 GSample/s.

5-4 Results and Discussion of Pulse Measurements

The waveforms observed by the oscilloscope are shown in Fig. 5.7. The frequency of the incident waves are 7(a), 8(b), 10(c) and 11 GHz(d). They are plotted by the full curve or broken curve corresponding with or without the plasma. Several traces are plotted in the same figure by performing the pulsed measurements in the same condition and in the different plasma shot.

The incident impulse in the O mode with these frequencies encounters the cutoff layer, and it is reflected at the vacuum chamber wall. The mode converted wave in the X mode with the frequency of 7 or 8 GHz is also reflected at the cutoff layer of the right hand X mode. However, the mode converted X mode due to magnetic fluctuation with the frequency of 10 or 11 GHz can passes through the plasma.

The Mode converted signals are observed due to multiple reflection by the vacuum chamber wall even if the plasma does not exist. In this case, it is noted that the impulse, which reaches the receiver horn directly, is eliminated by the polarizer attached to the receiver horn. That is, only the impulse reflected at the chamber wall rotate their mode slightly and reach the receiver horn.

In the case that the impulse with frequency of 10 or 11 GHz is injected into the plasma, the CPS impulse can reach directly to the receiver horn before arrival of the multi-reflected impulse. Time delay of the impulse between with and without plasma is about 4 ns, and is nearly consistent with the difference of optical path length.

While, in the case that the impulse with frequency of 7 or 8 GHz is injected into the plasma, it is arrived at the receiver horn after arrival of the mode-converted, multi-re-

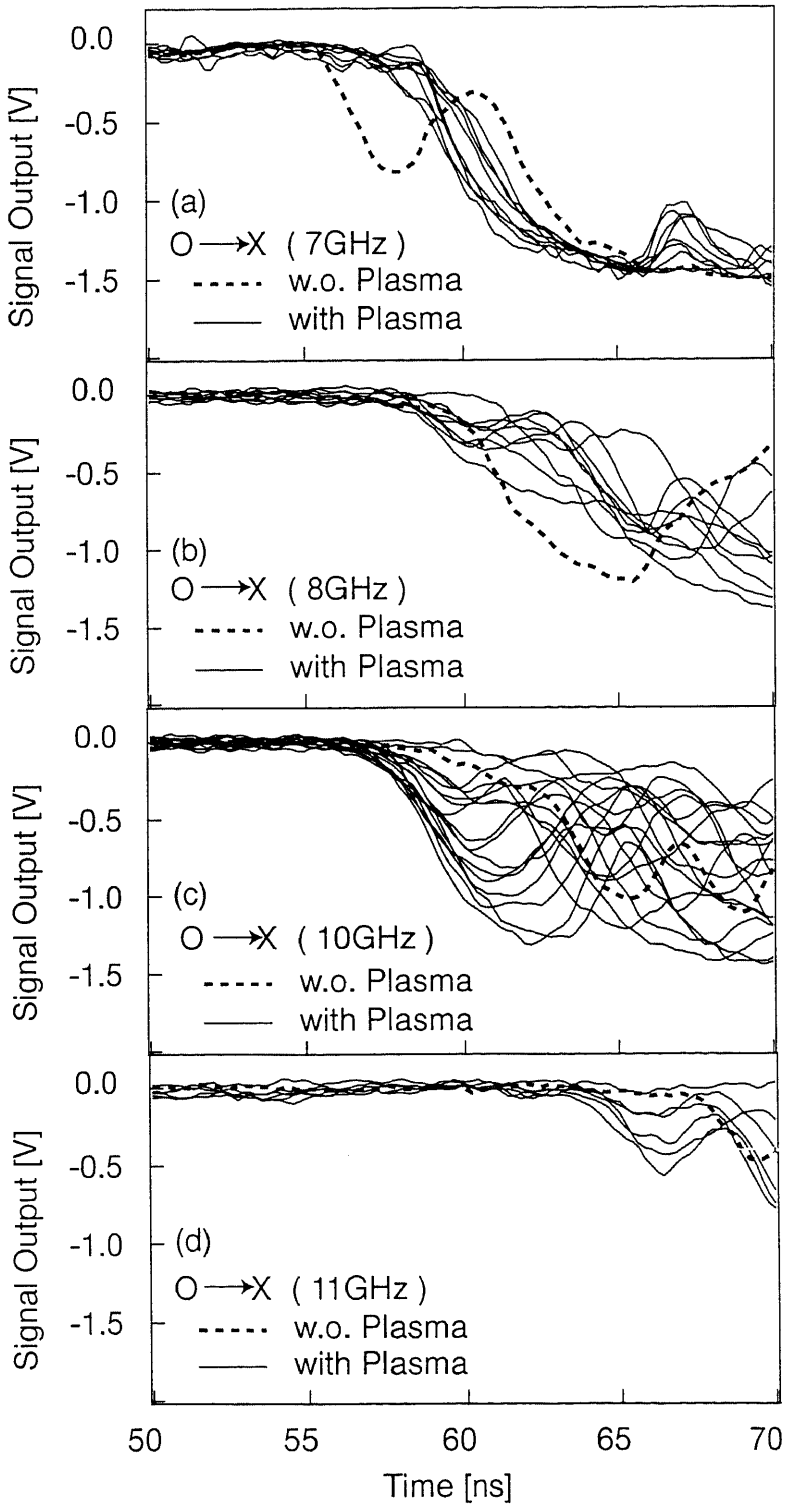

Figure 5.7 Waveforms observed by the oscilloscop without plasma (broken curve) and with plasma (full curve). Incident frequencies are 7(a), 8(b), 10(c) and 11 GHz(d).

flected impulse. This is considered that the optical path length is extended effectively due to the existence of the cutoff layer.

The detector output of 10 and 11 GHz components are 0-1.3 V and 0-0.6 V, respectively. The difference of each signal is explained as the difference of the incident power of each component in an ultrashort pulse, i.e., the amplitude with frequency of 10 GHz is 4 times as large as that of 11 GHz. The shot by shot deviation of the amplitude from 0 to 1.3 V may be attributed to the difference of magnetic fluctuation level at the measurement time. These are considered to be the signature of magnetic fluctuations measured with this system. We have measured the O→O mode direct transmission of the impulse without plasma. The detector output is 1.3 V with 55 dB attenuation of the impulse as shown in Fig, 5.8. By using this value, we estimate the mode conversion rate (the scattered power divided by the incident power) as $P_s/P_i \cong 0-10^{-4}$, i.e., $E_s/E_i \cong 0-10^{-2}$, where E_s, and E_i are the electric field of the scattered and the incident wave, respectively. The normalized magnetic fluctuation level with less than 10% is estimated by comparing the experimental results and the simulation (Fig. 5.5). However, this value includes the total scattered power from the scattering volume. In order to estimate the averaged level of the magnetic fluc-

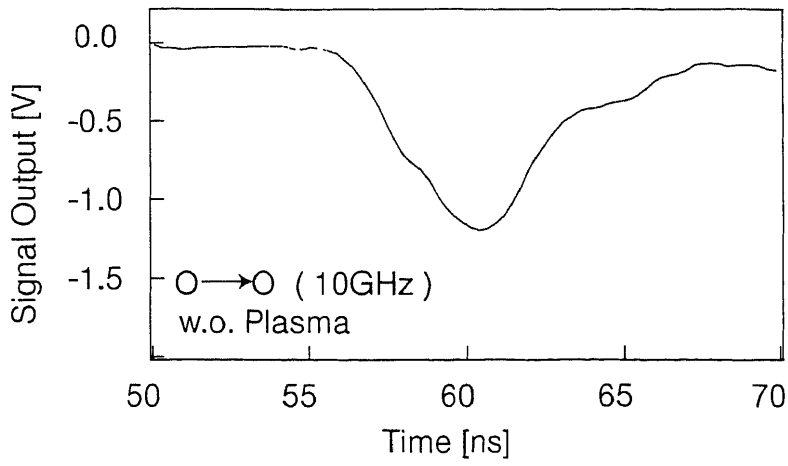

Figure 5.8 Waveforms observed by the oscilloscop without plasma. The horn in O mode is used as a receiver, and incident frequencies is 10 GHz.

tuation, the following estimation is performed. Assuming that the magnetic fluctuations of 10% are spreaded over the scattering volume, we obtain the total mode conversion rate along to the probe beam as 6.43 by integrating the mode-conversion rate (Fig 5.4) from 0 to 1 of n_{scat}/n_{cutoff}, that is, the integration is performed from the plasma edge to the cutoff layer. Since the mode-conversion rate is precisely proportional to the level of the magnetic fluctuation, the total averaged level of the fluctuations is obtained by comparing the rate of $E_s/E_i \cong 10^{-2}$ and $E_s/E_i \cong 6.43$, i.e., total averaged level approximates to $\tilde{B}/B \leq 10^{-2}/6.43 \times 10\% \cong 0.016\%$. This value is almost consistent with the absolute amplitude of 0.02% measured by the magnetic probes located at the edge of the plasma. However, the identification of the fluctuation is impossible in this system. The incident impulse with repetition rate of more than 20 MHz and pulse height-amplitude converter and Fourier analysis of the signal are necessary in order to identify the fluctuation.

5-5 Summary

In summary, the simulation of cross-polarization scattering has been performed with $(FD)^2TD$ method to clarify the relations between magnetic fluctuation and scattered wave induced by the CPS process. The relations between the scattered electric field and the density at the scattering center or the magnetic fluctuation level are obtained from the calculation. It is confirmed that the mode converted scattered wave increases with an increase in the electron density, and the ratio of the scattered wave to the normalized magnetic fluctuation level is 0.152.

The ultrashort pulse CPS system has been applied to the central-cell plasma in order to measure absolute level of the magnetic fluctuations. It is also confirmed that the CPS signal can be observed when the 10 or 11 GHz impulse is injected into the plasma. The averaged fluctuation amplitude is estimated to be 0.016% by comparing with the simulation results.

Chapter 6

Conclusions

In conclusion, we developed the CPS measurement system for measurement of the internal magnetic fluctuations.

At first, we have applied the CW wave-utilized CPS system to the central-cell plasma along with the reflectometer system, and found that the frequency spectrum of the CPS signal is broader than that of the reflectometer signal. This is explained that the signal with the CPS measurement satisfies wave-number matching condition in the scattering process, i.e., it observes finite wave number of the fluctuation. While reflectometer observes wave number of nearly zero, so that the frequency spectrum of the CPS signal is broader than that of the reflectometer signal by considering that the both measurements measure the fluctuation with same phase velocity.

Then we have applied the CPS system with movable receivers in order to observe the dispersion relation of the fluctuation. As a result of the measurement, it is found that the frequency spectrum is broadening, i.e., the central frequency is increasing, with an increase in the scattering angle due to the wave-number matching condition. Since the measured wave number can be divided into azimuthal and radial wave number from the geometrical analysis of the scattering angle, we can obtain the dispersion relation of the fluctuation. The present fluctuation seems to be electromagnetic drift wave Doppler shifted by $\boldsymbol{E} \times \boldsymbol{B}$ rotation velocity.

Next, we have applied the CPS measurement system which utilizes the ultrashort-pulse microwaves as a source in order to measure the absolute level of the magnetic fluc-

tuations.

Before the experiment, we have performed the numerical simulation of the electromagnetic-wave propagation in the dispersive and anisotropic medium with $(FD)^2TD$ method. We clarified the relations between the magnetic fluctuation and the scattered wave induced by the CPS process from the simulation, i.e., the mode converted scattered wave increases with an increase in the electron density and the level of the magnetic fluctuation.

In the experiment, we confirmed that the CPS signal can be observed when the 10 or 11 GHz impulse is injected into the plasma. The 10 or 11 GHz impulse injected into the plasma can reach the receiver earlier compared to that injected into the vacuum. While the 7 or 8 GHz impulse injected into the plasma was observed with several-nanoseconds delay compared to that injected into the vacuum. These are considered to be a signature that the mode-converted signal can be received with this system properly. From the deviation of the received impulse, the averaged fluctuation amplitude is estimated to be 0.016% by comparing with the simulation results.

From these experiments, we confirmed that the magnetic fluctuations can be measured with this system.

Appendix

Formulation of the CPS Process with $(FD)^2TD$ Notation

In this Appendix, we will formulate the CPS process with $(FD)^2TD$ notation. The $(FD)^2TD$ is a method that simulates propagation of electromagnetic fields in the dispersive and anisotropic medium [48,49]. At first, we will formulate the Maxwell's equation in the non-lossy medium with $(FD)^2TD$ notation along with the description of the coordinate systems in the calculation. Then the induced current by the CPS process is formulated with $(FD)^2TD$ in A-2. In A-3, full formulation of the CPS process is derived by combining Maxwell's equation and the induced current by the CPS.

A-1 Formulation of Maxwell Equation with $(FD)^2TD$ Notation

Coordinate Systems [50]

Computation space is divided temporally and spatially by a finite difference as shown in Fig. A.1, and Maxwell's equation is calculated according to the calculus of finite difference. Each component of the electric fields is evaluated spatially by the vector along the sides of a cubic cell divided by the width of Δx, Δy and Δz. The magnetic field components are evaluated by the normal vector of the cubes. The fields are divided temporally by finite difference Δt, and the electric and magnetic fields are defined to evaluate at the integer time and half integer time, respectively.

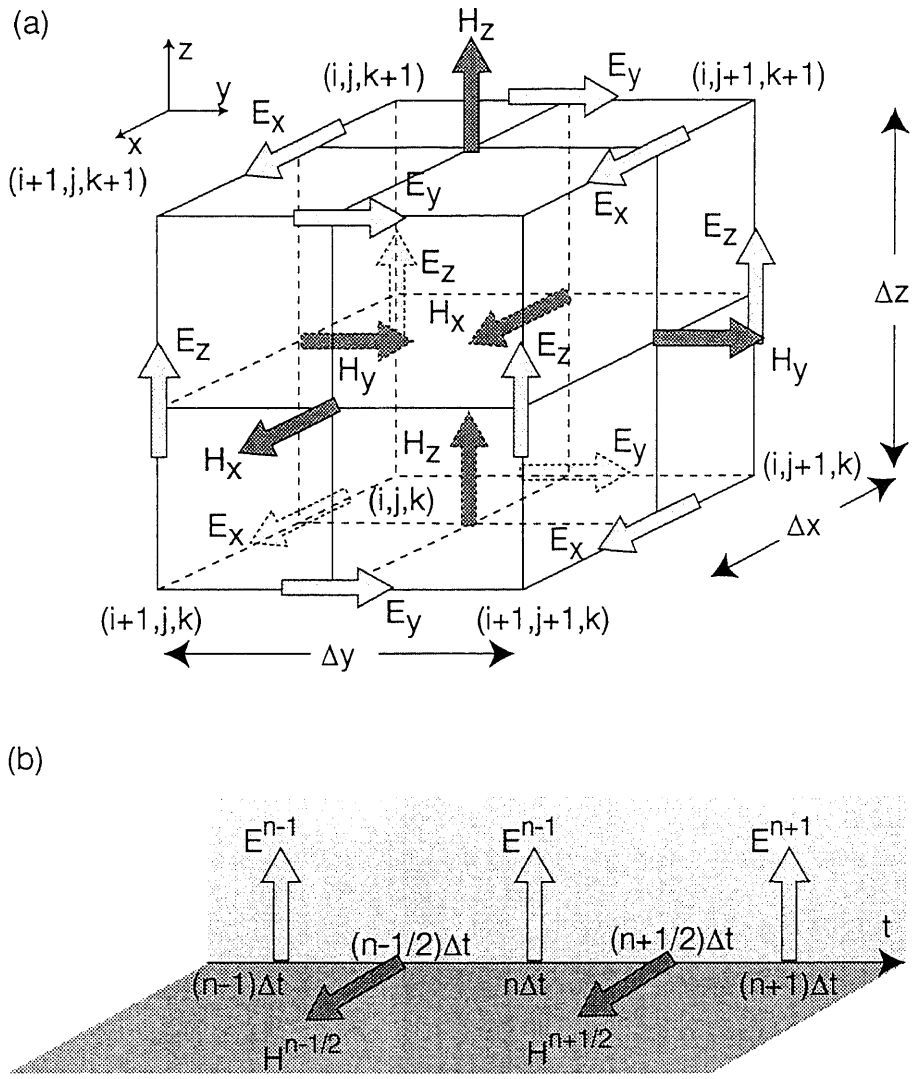

Figure A.1 Temporal and Spatial coordinate systems of the electromagnetic fields

Size of the Cell and Time Steps [50]

The FDTD method is based on calculus of finite difference, so that precision results of the simulation is obtained by minimal cell size, however the size of the memory and calculation time is further extended with the number of the cells. And maximum size of the cell is decided by the Nyquist's sampling theorem, i.e., size of the cell is smaller than half-wave length. Generally, the cell width of less than one tenth of the target wave length is adequate for precise calculation, i.e.,

$$\Delta x = \Delta y = \Delta z = \Delta \le \frac{\upsilon}{f_{\max}} \frac{1}{10}, \tag{A.1}$$

where υ is the speed of the target wave, and $f_{\max}$ is the target frequency.

While, the time step size is limited distinctly by the Courant's stability criterion as,

$$\Delta t \le \frac{1}{\upsilon\sqrt{(1/\Delta x)^2 + (1/\Delta y)^2 + (1/\Delta z)^2}}. \tag{A.2}$$

Temporary Formulation of Ampere's Law

In this subsection, we assume that the plasma is not a lossy medium and also dispersive and anisotropic materials. Derivation of the induced current with $(FD)^2TD$ notation will be described in A-2. According to the assumption, Ampere's law is described as

$$\nabla \times \boldsymbol{H} = \frac{\partial \boldsymbol{D}(\omega)}{\partial t} = \varepsilon_0 \frac{\partial \hat{\varepsilon}_r(\omega)\boldsymbol{E}}{\partial t}, \tag{A.3}$$

where $\hat{\varepsilon}_r(\omega)$ is the relative dielectric tensor denoted by

$$\hat{\varepsilon}_r(\omega) = \begin{pmatrix} \varepsilon_{xx} & -j\varepsilon_{xy} & 0 \\ j\varepsilon_{yx} & \varepsilon_{yy} & 0 \\ 0 & 0 & \varepsilon_{zz} \end{pmatrix} \tag{A.4}$$

$$= \begin{pmatrix} 1 - \dfrac{(\omega_{pe}/\omega)^2 \cdot (1 - j\nu/\omega)}{(1 - j\nu/\omega)^2 - (\omega_{ce}/\omega)^2} & -j\dfrac{(\omega_{pe}/\omega)^2 \cdot (\omega_{ce}/\omega)}{(1 - j\nu/\omega)^2 - (\omega_{ce}/\omega)^2} & 0 \\ j\dfrac{(\omega_{pe}/\omega)^2 \cdot (\omega_{ce}/\omega)}{(1 - j\nu/\omega)^2 - (\omega_{ce}/\omega)^2} & 1 - \dfrac{(\omega_{pe}/\omega)^2 \cdot (1 - j\nu/\omega)}{(1 - j\nu/\omega)^2 - (\omega_{ce}/\omega)^2} & 0 \\ 0 & 0 & 1 - \dfrac{\omega_{pe}^2}{\omega(j\nu - \omega)} \end{pmatrix},$$

$$= \begin{pmatrix} 1 + \chi_{xx}(\omega) & -j\chi_{xy}(\omega) & 0 \\ j\chi_{xy}(\omega) & 1 + \chi_{xx}(\omega) & 0 \\ 0 & 0 & 1 + \chi_{zz}(\omega) \end{pmatrix}$$

where χ are the dielectric susceptibility functions. In order to transform these susceptibili-

ties to time-domain functions, these are expanded into partial fractions and Fourier transformed as,

$$\chi_{yy}(t)=\chi_{yx}(t)=\mathrm{Re}\left[\tilde{\chi}_{xy}(t)\right]=\mathrm{Re}\left[\frac{2\omega_p^2}{s_p-\bar{s}_p}\left\{\left(1+\frac{\nu}{s_p}\right)e^{s_p t}-\frac{\nu}{s_p}\right\}\right] \tag{A.5 a}$$

$$j\chi_{xx}(t)=j\chi_{yy}(t)=\mathrm{Re}\left[j\tilde{\chi}_{xx}(t)\right]=\mathrm{Re}\left[\frac{2\omega_p^2\omega_c}{s_p-\bar{s}_p}\frac{1}{s_p}\left(e^{s_p t}-1\right)\right] \tag{A.5 b}$$

$$\chi_{zz}(t)=\frac{\omega_p^2}{\nu}\left(1-e^{-\nu t}\right)U(t), \tag{A.5 c}$$

where $s_p=-\nu+j\omega_{ce}$ and $\bar{s}_p=-\nu-j\omega_{ce}$ are the value at the pole of frequency-domain electric susceptibilities, and ν and $U(t)$ are the collision frequency and unit step function, respectively.

We can rewrite each component of the frequency-dependent constitutive equations relates to dielectric flux density by using these coefficients and convolution theorem [19] as,

$$D_x(t)/\varepsilon_0=E_x(t)+\int_0^t E_x(t-\tau)\chi_{xx}(\tau)d\tau-\int_0^t E_y(t-\tau)\chi_{xy}(\tau)d\tau \tag{A.6 a}$$

$$D_y(t)/\varepsilon_0=E_y(t)+\int_0^t E_y(t-\tau)\chi_{yy}(\tau)d\tau+\int_0^t E_x(t-\tau)\chi_{yx}(\tau)d\tau \tag{A.6 b}$$

$$D_z(t)/\varepsilon_0=E_z(t)+\int_0^t E_z(t-\tau)\chi_{zz}(\tau)d\tau. \tag{A.6 c}$$

Then Piecewise Linear Recursive Convolution (PLRC) method [51] is applied to Eq. (A.6) in order to calculate the electric field in the strong dispersive-medium precisely. This method assumes that the electric field evolves linearly from previous time step to present time step in the calculations. The integrations in the equations at $t=n\Delta t$ are written as the sum of the sequences by

$$\begin{aligned}\frac{D_x^n}{\varepsilon_0}=E_x^n&+\mathrm{Re}\left[\sum_{m=0}^{n-1}\left\{E_x^{n-m}\tilde{\chi}_{xx}^m+\left(E_x^{n-m-1}-E_x^{n-m}\right)\tilde{\xi}_{xx}^m\right\}\right]\\&-\mathrm{Re}\left[\sum_{m=0}^{n-1}\left\{E_y^{n-m}\tilde{\chi}_{xy}^m+\left(E_y^{n-m-1}-E_y^{n-m}\right)\tilde{\xi}_{xy}^m\right\}\right]\end{aligned} \tag{A.7 a}$$

$$\frac{D_y^n}{\varepsilon_0} = E_y^n + \mathrm{Re}\left[\sum_{m=0}^{n-1}\left\{E_y^{n-m}\tilde{\chi}_{yy}^m + \left(E_y^{n-m-1} - E_y^{n-m}\right)\tilde{\xi}_{yy}^m\right\}\right] - \mathrm{Re}\left[\sum_{m=0}^{n-1}\left\{E_x^{n-m}\tilde{\chi}_{yx}^m + \left(E_x^{n-m-1} - E_x^{n-m}\right)\tilde{\xi}_{yx}^m\right\}\right] \quad \text{(A.7 b)}$$

$$\frac{D_z^n}{\varepsilon_0} = E_z^n + \sum_{m=0}^{n-1}\left\{E_z^{n-m}\chi_{zz}^m + \left(E_z^{n-m-1} - E_z^{n-m}\right)\xi_{zz}^m\right\}, \quad \text{(A.7 c)}$$

where, superscripts like n, n-m and m indicate that the values are evaluated at $t=n\Delta t$, $(n-m)\Delta t$ and $m\Delta t$, respectively, and $\tilde{\chi}_{kl}^m$ and $\tilde{\xi}_{kl}^m$ are the constants described by

$$\tilde{\chi}_{kl}^m = \int_{m\Delta t}^{(m+1)\Delta t}\tilde{\chi}_{kl}(\tau)d\tau \quad \text{(A.8)}$$

and

$$\tilde{\xi}_{kl}^m = \int_{m\Delta t}^{(m+1)\Delta t}(\tau - m\Delta t)\tilde{\chi}_{kl}(\tau)d\tau \quad \text{(A.9)}$$

, respectively.

Finally, Ampere's law with the $(FD)^2TD$ notation is obtained by substracting dielectric flux density at $t=(n-1)\Delta t$ from Eqs. (A.7), as

$$\begin{aligned}\left(D_x^n - D_x^{n-1}\right)/\varepsilon_0 &= \left(1+\chi_{xx}^0 - \xi_{xx}^0\right)E_x^n - \left(1-\xi_{xx}^0\right)E_x^{n-1} \\ &\quad -\left(\chi_{xy}^0 - \xi_{xy}^0\right)E_y^n - \xi_{xy}^0 E_y^{n-1} - \Phi_{xx}^{n-1} + \Phi_{xy}^{n-1} \\ &= \frac{\Delta t}{\varepsilon_0}\left(\nabla\times\boldsymbol{H}^{n-1/2}\right)_x\end{aligned} \quad \text{(A.10 a)}$$

$$\begin{aligned}\left(D_y^n - D_y^{n-1}\right)/\varepsilon_0 &= \left(1+\chi_{yy}^0 - \xi_{yy}^0\right)E_y^n - \left(1-\xi_{yy}^0\right)E_y^{n-1} \\ &\quad +\left(\chi_{yx}^0 - \xi_{yx}^0\right)E_x^n + \xi_{yx}^0 E_x^{n-1} - \Phi_{yy}^{n-1} - \Phi_{yx}^{n-1} \\ &= \frac{\Delta t}{\varepsilon_0}\left(\nabla\times\boldsymbol{H}^{n-1/2}\right)_y\end{aligned} \quad \text{(A.10 b)}$$

$$\begin{aligned}\left(D_z^n - D_z^{n-1}\right)/\varepsilon_0 &= \left(1+\chi_{zz}^0 - \xi_{zz}^0\right)E_z^n - \left(1-\xi_{zz}^0\right)E_z^{n-1} - \Phi_{zz}^{n-1} \\ &= \frac{\Delta t}{\varepsilon_0}\left(\nabla\times\boldsymbol{H}^{n-1/2}\right)_z\end{aligned} \quad \text{(A.10 c)}$$

where Φ_{kl}^{n-1} are the variables at previous time step expressed by

$$\Phi_{kl}^{n-1} = \mathrm{Re}\left[\tilde{\Phi}_{kl}^{n-1}\right] = \mathrm{Re}\left[\sum_{m=0}^{n-2} E_l^{n-m-1}\Delta\tilde{\chi}_{kl}^{m} + \left(E_l^{n-m-2} - E_l^{n-m-1}\right)\Delta\tilde{\xi}_{kl}^{m}\right], \tag{A.11}$$

where, $\Delta\tilde{\chi}_{kl}^{m}$ and $\Delta\tilde{\xi}_{kl}^{m}$ are described by $\Delta\tilde{\chi}_{kl}^{m} = \tilde{\chi}_{kl}^{m} - \tilde{\chi}_{kl}^{m+1}$ and $\Delta\tilde{\xi}_{kl}^{m} = \tilde{\xi}_{kl}^{m} - \tilde{\xi}_{kl}^{m+1}$, respectively.

Consequently, each component of the electric field is obtained by solving the simultaneous equations of Eqs. (A.10) for E_x, E_y and E_z at the present time step as follows.

$$\begin{aligned}
E_x^n = {} & \frac{\left(1+\chi_{xx}^0-\xi_{xx}^0\right)\left(1-\xi_{xx}^0\right)-\left(\chi_{xy}^0-\xi_{xy}^0\right)\xi_{xy}^0}{\left(1+\chi_{xx}^0-\xi_{xx}^0\right)^2+\left(\chi_{xy}^0-\xi_{xy}^0\right)^2}E_x^{n-1} \\
& + \frac{\chi_{xx}^0\xi_{xy}^0+\left(1-\xi_{xx}^0\right)\chi_{xy}^0}{\left(1+\chi_{xx}^0-\xi_{xx}^0\right)^2+\left(\chi_{xy}^0-\xi_{xy}^0\right)^2}E_y^{n-1} \\
& + \frac{1+\chi_{xx}^0-\xi_{xx}^0}{\left(1+\chi_{xx}^0-\xi_{xx}^0\right)^2+\left(\chi_{xy}^0-\xi_{xy}^0\right)^2}\left(\Phi_{xx}^{n-1}-\Phi_{xy}^{n-1}+\frac{\Delta t}{\varepsilon_0}\left(\nabla\times\boldsymbol{H}^{n-1/2}\right)_x\right) \\
& + \frac{\chi_{xy}^0-\xi_{xy}^0}{\left(1+\chi_{xx}^0-\xi_{xx}^0\right)^2+\left(\chi_{xy}^0-\xi_{xy}^0\right)^2}\left\{\Phi_{yy}^{n-1}+\Phi_{yx}^{n-1}+\frac{\Delta t}{\varepsilon_0}\left(\nabla\times\boldsymbol{H}^{n-1/2}\right)_y\right\}
\end{aligned} \tag{A.12 a}$$

$$\begin{aligned}
E_y^n = {} & \frac{\left(1+\chi_{yy}^0-\xi_{yy}^0\right)\left(1-\xi_{yy}^0\right)-\left(\chi_{yx}^0-\xi_{yx}^0\right)\xi_{xy}^0}{\left(1+\chi_{yy}^0-\xi_{yy}^0\right)^2+\left(\chi_{yx}^0-\xi_{yx}^0\right)^2}E_y^{n-1} \\
& - \frac{\chi_{yy}^0\xi_{yx}^0+\left(1-\xi_{yy}^0\right)\chi_{yx}^0}{\left(1+\chi_{yy}^0-\xi_{yy}^0\right)^2+\left(\chi_{yx}^0-\xi_{yx}^0\right)^2}E_x^{n-1} \\
& + \frac{1+\chi_{yy}^0-\xi_{yy}^0}{\left(1+\chi_{yy}^0-\xi_{yy}^0\right)^2+\left(\chi_{yx}^0-\xi_{yx}^0\right)^2}\left\{+\Phi_{yy}^{n-1}+\Phi_{yx}^{n-1}+\frac{\Delta t}{\varepsilon_0}\left(\nabla\times\boldsymbol{H}^{n-1/2}\right)_y\right\} \\
& - \frac{\chi_{yx}^0-\xi_{yx}^0}{\left(1+\chi_{yy}^0-\xi_{yy}^0\right)^2+\left(\chi_{yx}^0-\xi_{yx}^0\right)^2}\left(\Phi_{xx}^{n-1}-\Phi_{xy}^{n-1}+\frac{\Delta t}{\varepsilon_0}\left(\nabla\times\boldsymbol{H}^{n-1/2}\right)_x\right)
\end{aligned} \tag{A.12 b}$$

$$E_z^n = \frac{1-\xi_{zz}^0}{1+\chi_{zz}^0-\xi_{zz}^0}E_z^{n-1} + \frac{1}{1+\chi_{zz}^0-\xi_{zz}^0}\left\{\Phi_{zz}^{n-1}+\frac{\Delta t}{\varepsilon_0}\left(\nabla\times\boldsymbol{H}^{n-1/2}\right)_z\right\} \tag{A.12 c}$$

Temporal and Spatial Formulation of Faraday's Law

For formulating Faraday's law with $(FD)^2TD$ notation, we assume that magnetic

permeability is a value in the vacuum, i.e., calculation does not take account of anisotropic and dispersive effect in Faraday's law. Faraday's law is

$$\frac{\partial \boldsymbol{H}}{\partial t} = -\frac{1}{\mu}\nabla \times \boldsymbol{E}. \tag{A.13}$$

The derivative of $\boldsymbol{H}$ at $t=n\Delta t$ is made as central difference between the magnetic field at $t=(n+1/2)\Delta t$ and $t=(n-1/2)\Delta t$, as

$$\frac{\boldsymbol{H}^{n+1/2} - \boldsymbol{H}^{n-1/2}}{\Delta t} = -\frac{1}{\mu}\nabla \times \boldsymbol{E}. \tag{A.14}$$

The rotation of $\boldsymbol{E}$ at evaluation point of each magnetic field component is made spatially by the same way to the temporal derivation. Finally, the magnetic field of each component at the present time step is described as,

$$\begin{aligned} H_x^{n+1/2}(i,j+1/2,k+1/2) = {} & H_x^{n-1/2}(i,j+1/2,k+1/2) \\ & -\frac{\Delta t}{\mu_0 \Delta y}\left\{E_z^n(i,j+1,k+1/2) - E_z^n(i,j,k+1/2)\right\} \\ & +\frac{\Delta t}{\mu_0 \Delta z}\left\{E_y^n(i,j+1/2,k+1) - E_y^n(i,j+1/2,k)\right\} \end{aligned} \tag{A.15a}$$

$$\begin{aligned} H_y^{n+1/2}(i+1/2,j,k+1/2) = {} & H_y^{n-1/2}(i+1/2,j,k+1/2) \\ & -\frac{\Delta t}{\mu_0 \Delta z}\left\{E_x^n(i+1/2,j,k+1) - E_x^n(i+1/2,j,k)\right\} \\ & +\frac{\Delta t}{\mu_0 \Delta x}\left\{E_z^n(i+1,j,k+1/2) - E_z^n(i,j,k+1/2)\right\} \end{aligned} \tag{A.15b}$$

$$\begin{aligned} H_z^{n+1/2}(i+1/2,j+1/2,k) = {} & H_z^{n-1/2}(i+1/2,j+1/2,k) \\ & -\frac{\Delta t}{\mu_0 \Delta x}\left\{E_y^n(i+1,j+1/2,k) - E_y^n(i,j+1/2,k)\right\} \\ & +\frac{\Delta t}{\mu_0 \Delta y}\left\{E_x^n(i+1/2,j+1,k) - E_x^n(i+1/2,j,k)\right\} \end{aligned} \tag{A.15c}$$

where, i, j and k denote the position of each electromagnetic field vector.

In the case of non-lossy medium, the calculation is executed by applying Eqs. (A.12) and (A.15) mutually.

A-2 Formulation of Induced Current of the CPS with (FD)^{2}TD Notation

In this subsection, we will formulate the induced current by the CPS with (FD)^{2}TD notation. Each element of the induced current by the CPS is derived from Eq. (2.32), as

$$J_{CPS}(\omega) = -\frac{\omega_{ce}\varepsilon_0\omega^2}{\omega_{pe}^2 B_0} \times \begin{pmatrix} 2j\chi_{xx}\chi_{xy}\tilde{B}_z E_x + \left(\chi_{xx}^2 + \chi_{xy}^2\right)\tilde{B}_z E_y - \left\{\left(\chi_{xx}^2 + \chi_{xy}^2\right)\tilde{B}_y + 2j\chi_{xx}\chi_{xy}\tilde{B}_x\right\}E_z \\ -\left(\chi_{xx}^2 + \chi_{xy}^2\right)\tilde{B}_z E_x + 2j\chi_{xx}\chi_{xy}\tilde{B}_z E_y + \left\{\left(\chi_{xx}^2 + \chi_{xy}^2\right)\tilde{B}_x - 2j\chi_{xx}\chi_{xy}\tilde{B}_y\right\}E_z \\ \chi_{zz}^2\tilde{B}_y E_x - \chi_{zz}^2\tilde{B}_x E_y \end{pmatrix} \quad \text{(A.16)}$$

where $\tilde{B}_x$, $\tilde{B}_y$ and $\tilde{B}_z$ are the each component of the magnetic field fluctuation. The frequency-dependent components such as $\omega^2\chi_{xx}(\omega)\chi_{xy}(\omega)$ are converted into time-dependent components by Laplace transformation. Convolution theorem and PLRC method are also applied to these components by the same way to derivation of Ampere's law. Finally, we have the induced current at the present time step, as

$$J_x^n = -\frac{\omega_{ce}\varepsilon_0}{\omega_{pe}^2 B_0}\begin{Bmatrix} \tilde{B}_z\left(2\Psi_{xxxy\chi}^{n(E_x)} + 2\Psi_{xxxy\xi}^{n(E_x)} + \Psi_{xx^2\chi}^{n(E_y)} + \Psi_{xx^2\xi}^{n(E_y)} + \Psi_{xy^2\chi}^{n(E_y)} + \Psi_{xy^2\xi}^{n(E_y)}\right) \\ -\tilde{B}_y\left(\Psi_{xx^2\chi}^{n(E_z)} + \Psi_{xx^2\xi}^{n(E_z)} + \Psi_{xy^2\chi}^{n(E_z)} + \Psi_{xy^2\xi}^{n(E_z)}\right) \\ -\tilde{B}_x\left(2\Psi_{xxxy\chi}^{n(E_z)} + 2\Psi_{xxxy\xi}^{n(E_z)}\right) \end{Bmatrix} \quad \text{(A.17a)}$$

$$J_y^n = -\frac{\omega_{ce}\varepsilon_0}{\omega_{pe}^2 B_0}\begin{Bmatrix} \tilde{B}_z\left(2\Psi_{xxxy\chi}^{n(E_y)} + 2\Psi_{xxxy\xi}^{n(E_y)} - \Psi_{xx^2\chi}^{n(E_x)} - \Psi_{xx^2\xi}^{n(E_x)} - \Psi_{xy^2\chi}^{n(E_x)} - \Psi_{xy^2\xi}^{n(E_x)}\right) \\ +\tilde{B}_x\left(\Psi_{xx^2\chi}^{n(E_z)} + \Psi_{xx^2\xi}^{n(E_z)} + \Psi_{xy^2\chi}^{n(E_z)} + \Psi_{xy^2\xi}^{n(E_z)}\right) \\ -\tilde{B}_y\left(2\Psi_{xxxy\chi}^{n(E_z)} + 2\Psi_{xxxy\xi}^{n(E_z)}\right) \end{Bmatrix} \quad \text{(A.17b)}$$

$$J_z^n = -\frac{\omega_{ce}\varepsilon_0}{\omega_{pe}^2 B_0}\left\{\tilde{B}_y\left(\Psi_{zz^2\chi}^{n(E_x)} + \Psi_{zz^2\xi}^{n(E_x)}\right) - \tilde{B}_x\left(2\Psi_{zz^2\chi}^{n(E_y)} + 2\Psi_{zz^2\xi}^{n(E_y)}\right)\right\} \tag{A.17c}$$

where $\Psi_{\text{argument}}^{n(E_{\text{argument}})}$ is the variable. In this equation, subscripts like $xxxy\chi$, $xx^2\chi$, $xy^2\chi$, $xxxy\xi$, $xx^2\xi$ and $xy^2\xi$ are associated with components of $\tilde{\chi}_{xxxy}^m$, $\tilde{\chi}_{xx^2}^m$, $\tilde{\chi}_{xy^2}^m$, $\tilde{\xi}_{xxxy}^m$, $\tilde{\xi}_{xx^2}^m$, and $\tilde{\xi}_{xy^2}^m$, respectively, which values are derived by the same way to Eqs. (A.8) and (A.9). And superscripts like E_x, E_y, and E_z indicate that the component of each electric field is a dependent variable in the expression of Ψ_{argument}^n. The value of Ψ^n is related to that at $t=(n\text{-}1)\Delta t$, e.g.

$$\Psi_{xxxy\chi}^n = \tilde{\chi}_{xxxy}^0 E^n + e^{(-\nu+j\omega_c)\Delta t}\Psi_{xxxy\chi}^{n-1} + \Phi_{xxxy\chi}^{n-1}, \tag{A.18}$$

where $\tilde{\chi}_{xxxy}^0$ is the constant derived by integrating $\tilde{\chi}_{xxxy}(\tau)$ from 0 to Δt, and $\Phi_{xxxy\chi}^{n-1}$ is the variable described as

$$\Phi_{xxxy\chi}^{n-1} = -\frac{j\omega_{pe}^4\Delta t}{2(-\nu+j\omega_{ce})}e^{(-\nu+j\omega_c)\Delta t}\left(e^{(-\nu+j\omega_c)\Delta t}-1\right)E^{n-1} + e^{(-\nu+j\omega_c)\Delta t}\Phi_{xxxy\chi}^{n-2}. \tag{A.19}$$

A-3 Full Formulation of the CPS Process

Temporal Formulation of Faraday's Law

Faraday's law at the present time step is rewritten with $(FD)^2TD$ notation, as

$$\begin{aligned}\frac{\Delta t}{\varepsilon_0}\nabla\times H^{n-1/2} &= \frac{D^n - D^{n-1}}{\varepsilon_0} + \frac{\Delta t}{\varepsilon_0}J^{n-1/2} \\ &= \frac{D^n - D^{n-1}}{\varepsilon_0} + \frac{\Delta t}{\varepsilon_0}\frac{J^n + J^{n-1}}{2},\end{aligned} \tag{A.20}$$

where, induced current can not be evaluated at half integer time, so that the averaged induced current by present and previous time step are used in the calculation.

While, Eqs. (A.17) is rewritten by expanding for electric field at the present and previous time step, as

$$J_x^n = -\frac{\omega_{ce}\varepsilon_0}{\omega_{pe}^2 B_0}\begin{bmatrix} 2\tilde{B}_z\left\{\chi^0_{,xxxy}E_x^n + \xi^0_{,xxxy}\left(E_x^{n-1}-E_x^n\right)+P_1^{n-1}\right\} \\ +\tilde{B}_z\left\{\left(\chi^0_{,xx^2}+\chi^0_{,xy^2}\right)E_y^n+\left(\xi^0_{,xx^2}+\xi^0_{,xy^2}\right)\left(E_y^{n-1}-E_y^n\right)+P_2^{n-1}\right\} \\ -\tilde{B}_y\left\{\left(\chi^0_{,xx^2}+\chi^0_{,xy^2}\right)E_z^n+\left(\xi^0_{,xx^2}+\xi^0_{,xy^2}\right)\left(E_z^{n-1}-E_z^n\right)+P_3^{n-1}\right\} \\ -2\tilde{B}_x\left\{\chi^0_{,xxxy}E_z^n+\xi^0_{,xxxy}\left(E_z^{n-1}-E_z^n\right)+P_4^{n-1}\right\} \end{bmatrix} \quad \text{(A.21 a)}$$

$$J_y^n = -\frac{\omega_{ce}\varepsilon_0}{\omega_{pe}^2 B_0}\begin{bmatrix} -\tilde{B}_z\left\{\left(\chi^0_{,xx^2}+\chi^0_{,xy^2}\right)E_x^n+\left(\xi^0_{,xx^2}+\xi^0_{,xy^2}\right)\left(E_x^{n-1}-E_x^n\right)+Q_1^{n-1}\right\} \\ +2\tilde{B}_z\left\{\chi^0_{,xxxy}E_y^n+\xi^0_{,xxxy}\left(E_y^{n-1}-E_y^n\right)+Q_2^{n-1}\right\} \\ +\tilde{B}_x\left\{\left(\chi^0_{,xx^2}+\chi^0_{,xy^2}\right)E_z^n+\left(\xi^0_{,xx^2}+\xi^0_{,xy^2}\right)\left(E_z^{n-1}-E_z^n\right)+P_3^{n-1}\right\} \\ -2\tilde{B}_y\left\{\chi^0_{,xxxy}E_z^n+\xi^0_{,xxxy}\left(E_z^{n-1}-E_z^n\right)+P_4^{n-1}\right\} \end{bmatrix} \quad \text{(A.21 b)}$$

$$J_z^n = -\frac{\omega_{ce}\varepsilon_0}{\omega_{pe}^2 B_0}\begin{bmatrix} \tilde{B}_y\left\{\chi^0_{,zz^2}E_x^n+\xi^0_{,zz^2}\left(E_x^{n-1}-E_x^n\right)+R_1^{n-1}\right\} \\ -\tilde{B}_x\left\{\chi^0_{,zz^2}E_y^n+\xi^0_{,zz^2}\left(E_y^{n-1}-E_y^n\right)+R_2^{n-1}\right\} \end{bmatrix} \quad \text{(A.21 c)}$$

where,

$$P_1^{n-1} = \mathrm{Re}\left[e^{s_p\Delta t}\left(\tilde{\Psi}^{n-1(E_x)}_{,xxxy\chi}+\tilde{\Psi}^{n-1(E_x)}_{,xxxy\xi}\right)+\Phi^{n-1(E_x)}_{,xxxy\chi}+\Phi^{n-1(E_x)}_{,xxxy\xi}\right] \quad \text{(A.22 a)}$$

$$P_2^{n-1} = \mathrm{Re}\left[\begin{matrix} e^{s_p\Delta t}\left(\tilde{\Psi}^{n-1(E_y)}_{,xx^2\chi}+\tilde{\Psi}^{n-1(E_y)}_{,xx^2\xi}+\tilde{\Psi}^{n-1(E_y)}_{,xy^2\chi}+\tilde{\Psi}^{n-1(E_y)}_{,xy^2\xi}\right) \\ +\Phi^{n-1(E_y)}_{,xx^2\chi}+\Phi^{n-1(E_y)}_{,xx^2\xi}+\Phi^{n-1(E_y)}_{,xy^2\chi}+\Phi^{n-1(E_y)}_{,xy^2\xi} \end{matrix}\right] \quad \text{(A.22 b)}$$

$$P_3^{n-1} = \mathrm{Re}\left[\begin{matrix} e^{s_p\Delta t}\left(\tilde{\Psi}^{n-1(E_z)}_{,xx^2\chi}+\tilde{\Psi}^{n-1(E_z)}_{,xx^2\xi}+\tilde{\Psi}^{n-1(E_z)}_{,xy^2\chi}+\tilde{\Psi}^{n-1(E_z)}_{,xy^2\xi}\right) \\ +\Phi^{n-1(E_z)}_{,xx^2\chi}+\Phi^{n-1(E_z)}_{,xx^2\xi}+\Phi^{n-1(E_z)}_{,xy^2\chi}+\Phi^{n-1(E_z)}_{,xy^2\xi} \end{matrix}\right] \quad \text{(A.22 c)}$$

$$P_4^{n-1} = \mathrm{Re}\left[e^{s_p\Delta t}\left(\tilde{\Psi}^{n-1(E_z)}_{,xxxy\chi}+\tilde{\Psi}^{n-1(E_z)}_{,xxxy\xi}\right)+\Phi^{n-1(E_z)}_{,xxxy\chi}+\Phi^{n-1(E_z)}_{,xxxy\xi}\right] \quad \text{(A.22 d)}$$

$$Q_1^{n-1} = \mathrm{Re}\left[\begin{matrix} e^{s_p\Delta t}\left(\tilde{\Psi}^{n-1(E_x)}_{,xx^2\chi}+\tilde{\Psi}^{n-1(E_x)}_{,xx^2\xi}+\tilde{\Psi}^{n-1(E_x)}_{,xy^2\chi}+\tilde{\Psi}^{n-1(E_x)}_{,xy^2\xi}\right) \\ +\Phi^{n-1(E_x)}_{,xx^2\chi}+\Phi^{n-1(E_x)}_{,xx^2\xi}+\Phi^{n-1(E_x)}_{,xy^2\chi}+\Phi^{n-1(E_x)}_{,xy^2\xi} \end{matrix}\right] \quad \text{(A.22 e)}$$

$$Q_2^{n-1} = \mathrm{Re}\left[e^{s_p\Delta t}\left(\tilde{\Psi}^{n-1(E_y)}_{,xxxy\chi}+\tilde{\Psi}^{n-1(E_y)}_{,xxxy\xi}\right)+\Phi^{n-1(E_y)}_{,xxxy\chi}+\Phi^{n-1(E_y)}_{,xxxy\xi}\right] \quad \text{(A.22 f)}$$

$$R_1^{n-1} = \mathrm{Re}\left[e^{-\nu\Delta t}\left(\Psi^{n-1(E_x)}_{,zz^2\chi}+\Psi^{n-1(E_x)}_{,zz^2\xi}\right)+\Phi^{n-1(E_x)}_{,zz^2\chi}+\Phi^{n-1(E_x)}_{,zz^2\xi}\right] \quad \text{(A.22 g)}$$

$$R_2^{n-1} = \mathrm{Re}\left[e^{-\nu\Delta t}\left(\Psi_{zz^2\chi}^{n-1(E_v)} + \Psi_{zz^2\xi}^{n-1(E_v)} \right) + \Phi_{zz^2\chi}^{n-1(E_v)} + \Phi_{zz^2\xi}^{n-1(E_v)} \right]. \tag{A.22 h}$$

By substituting Eqs. (A.10) and (A.21) into Eq. (A.20), we have simultaneous equations for the electric fields at present and previous time steps, as

$$h_x = A_x E_x^n + B_x E_x^{n-1} + C_x E_y^n + D_x E_y^{n-1} + F_x E_z^n + G_x E_z^{n-1} + I_x \tag{A.23 a}$$

$$h_y = A_y E_y^n + B_y E_y^{n-1} + C_y E_x^n + D_y E_x^{n-1} + F_y E_z^n + G_y E_z^{n-1} + I_y \tag{A.23 b}$$

$$h_z = A_z E_z^n + B_z E_z^{n-1} + C_z E_x^n + D_z E_x^{n-1} + F_z E_y^n + G_z E_y^{n-1} + I_z \tag{A.23 c}$$

where, each coefficient is described by

$$A_x = A_y = 1 + \chi_{xxx}^0 - \xi_{xxx}^0 - \frac{\omega_{ce}\Delta t}{2B_0\omega_{pe}^2} \cdot 2\tilde{B}_z\left(\chi_{xxxy}^0 - \xi_{xxxy}^0 \right) \tag{A.24 a}$$

$$B_x = B_y = -1 + \xi_{xxx}^0 - \frac{\omega_{ce}\Delta t}{2B_0\omega_{pe}^2} \cdot 2\tilde{B}_z\xi_{xxxy}^0 \tag{A.24 b}$$

$$C_x = -C_y = -\chi_{xxy}^0 + \xi_{xxy}^0 - \frac{\omega_{ce}\Delta t}{2B_0\omega_{pe}^2} \cdot \tilde{B}_z\left(\chi_{xx^2}^0 - \xi_{xx^2}^0 + \chi_{xy^2}^0 - \xi_{xy^2}^0 \right) \tag{A.24 c}$$

$$D_x = -D_y = -\xi_{xxy}^0 - \frac{\omega_{ce}\Delta t}{2B_0\omega_{pe}^2} \cdot \tilde{B}_z\left(\xi_{xx^2}^0 + \xi_{xy^2}^0 \right) \tag{A.24 d}$$

$$F_x = \frac{\omega_{ce}\Delta t}{2B_0\omega_{pe}^2}\left\{ \tilde{B}_y\left(\chi_{xx^2}^0 - \xi_{xx^2}^0 + \chi_{xy^2}^0 - \xi_{xy^2}^0 \right) + 2\tilde{B}_x\left(\chi_{xxxy}^0 - \xi_{xxxy}^0 \right) \right\} \tag{A.24 e}$$

$$G_x = \frac{\omega_{ce}\Delta t}{2B_0\omega_{pe}^2}\left\{ \tilde{B}_y\left(\xi_{xx^2}^0 + \xi_{xy^2}^0 \right) + 2\tilde{B}_x\xi_{xxxy}^0 \right\} \tag{A.24 f}$$

$$h_x = \frac{\Delta t}{\varepsilon_0}\left(\nabla \times \boldsymbol{H}^{n-1/2} \right)_x \tag{A.24 g}$$

$$\begin{aligned} I_x = & -\Phi_{xxx}^{n-1} + \Phi_{xxy}^{n-1} \\ & - \frac{\omega_{ce}\Delta t}{2B_0\omega_{pe}^2}\left(2\tilde{B}_z P_1^{n-1} + \tilde{B}_z P_2^{n-1} - \tilde{B}_y P_3^{n-1} - 2\tilde{B}_x P_4^{n-1} \right) + \frac{\Delta t}{2\varepsilon_0} J_x^{n-1} \end{aligned} \tag{A.24 h}$$

$$F_y = \frac{\omega_{ce}\Delta t}{2B_0\omega_{pe}^2}\left\{2\tilde{B}_y\left(\chi^0_{xxxy} - \xi^0_{xxxy}\right) - \tilde{B}_x\left(\chi^0_{xx^2} - \xi^0_{xx^2} + \chi^0_{xy^2} - \xi^0_{xy^2}\right)\right\} \quad \text{(A.24 i)}$$

$$G_y = -\frac{\omega_{ce}\Delta t}{2B_0\omega_{pe}^2}\left\{\tilde{B}_x\left(\xi^0_{xx^2} + \xi^0_{xy^2}\right) - 2\tilde{B}_y\xi^0_{xxxy}\right\} \quad \text{(A.24 j)}$$

$$h_y = \frac{\Delta t}{\varepsilon_0}\left(\nabla \times \boldsymbol{H}^{n-1/2}\right)_y \quad \text{(A.24 k)}$$

$$I_y = -\Phi^{n-1}_{yy} - \Phi^{n-1}_{yx} - \frac{\omega_{ce}\Delta t}{2B_0\omega_{pe}^2}\left(-\tilde{B}_z Q_1^{n-1} + 2\tilde{B}_z Q_2^{n-1} + \tilde{B}_x P_3^{n-1} - 2\tilde{B}_y P_4^{n-1}\right) + \frac{\Delta t}{2\varepsilon_0} J_y^{n-1} \quad \text{(A.24 l)}$$

$$A_z = 1 + \chi^0_{zz} - \xi^0_{zz} \quad \text{(A.24 m)}$$

$$B_z = -1 + \xi^0_{zz} \quad \text{(A.24 n)}$$

$$C_z = -\frac{\omega_{ce}\Delta t}{2B_0\omega_{pe}^2}\tilde{B}_y\left(\chi^0_{zz^2} - \xi^0_{zz^2}\right) \quad \text{(A.24 o)}$$

$$D_z = -\frac{\omega_{ce}\Delta t}{2B_0\omega_{pe}^2}\tilde{B}_y\xi^0_{zz^2} \quad \text{(A.24 p)}$$

$$F_z = \frac{\omega_{ce}\Delta t}{2B_0\omega_{pe}^2}\tilde{B}_x\left(\chi^0_{zz^2} - \xi^0_{zz^2}\right) \quad \text{(A.24 q)}$$

$$G_z = \frac{\omega_{ce}\Delta t}{2B_0\omega_{pe}^2}\tilde{B}_x\xi^0_{zz^2} \quad \text{(A.24 r)}$$

$$h_z = \frac{\Delta t}{\varepsilon_0}\left(\nabla \times \boldsymbol{H}^{n-1/2}\right)_z \quad \text{(A.24 s)}$$

$$I_z = -\Phi^{n-1}_{zz} - \frac{\omega_{ce}\Delta t}{2B_0\omega_{pe}^2}\left(-\tilde{B}_y R_1^{n-1} - \tilde{B}_z R_2^{n-1}\right) + \frac{\Delta t}{2\varepsilon_0} J_z^{n-1}. \quad \text{(A.24 t)}$$

Finally, temporal formulation has been made by solving Eq. (A.23) for the electric fields at the present time step as follows.

$$E_x^n = \frac{1}{-A_xA_yA_z + A_zC_xC_y + A_yC_zF_x - C_xC_zF_y - C_yF_xF_z + A_xF_yF_z} \times$$

$$\left\{\begin{array}{l}
\left(A_yA_zB_x - A_zC_xD_y - A_yD_zF_x + C_xD_zF_y + D_yF_xF_z - B_xF_yF_z\right)E_x^{n-1} + \\
\left(-A_zB_yC_x + A_yA_zD_x + B_yF_xF_z - D_xF_yF_z - A_yF_xG_z + C_xF_yG_z\right)E_y^{n-1} - \\
\left(-A_yB_zF_x + B_zC_xF_y + A_yA_zG_x - F_yF_zG_x - A_zC_xG_y + F_xF_zG_y\right)E_z^{n-1} - \\
A_yA_zh_x + F_yF_zh_x + A_zC_xh_y - F_xF_zh_y + A_yF_xh_z - C_xF_yh_z + \\
A_yA_zI_x - F_yF_zI_x - A_zC_xI_y + F_xF_zI_y - A_yF_xI_z + C_xF_yI_z
\end{array}\right\} \quad \text{(A.25 a)}$$

$$E_y^n = \frac{1}{A_xA_yA_z - A_zC_xC_y - A_yC_zF_x + C_xC_zF_y + C_yF_xF_z - A_xF_yF_z} \times$$

$$\left\{\begin{array}{l}
\left(A_zB_xC_y - A_xA_zD_y + C_zD_yF_x - C_yD_zF_x - B_xC_zF_y + A_xD_zF_y\right)E_x^{n-1} + \\
\left(-A_xA_zB_y + A_zC_yD_x + B_yC_zF_x - C_zD_xF_y - C_yF_xG_z + A_xF_yG_z\right)E_y^{n-1} + \\
\left(-B_zC_yF_x + A_xB_zF_y + A_zC_yG_x - C_zF_yG_x - A_xA_zG_y + C_zF_xG_y\right)E_z^{n-1} + \\
-A_zC_yh_x + C_zF_yh_x + A_xA_zh_y - C_zF_xh_y + C_yF_xh_z - A_xF_yh_z + \\
A_zC_yI_x - C_zF_yI_x - A_xA_zI_y + C_zF_xI_y - C_yF_xI_z + A_xF_yI_z
\end{array}\right\} \quad \text{(A.25 b)}$$

$$E_z^n = \frac{1}{-A_xA_yA_z + A_zC_xC_y + A_yC_zF_x - C_xC_zF_y - C_yF_xF_z + A_xF_yF_z} \times$$

$$\left\{\begin{array}{l}
\left(-A_yB_xC_z + C_xC_zD_y + A_xA_yD_z - C_xCyD_z + B_xC_yF_z - A_xD_yF_z\right)_y E_x^{n-1} + \\
\left(B_yC_xC_z - A_yC_zD_x - A_xB_yF_z + C_yD_xF_z + A_xA_yG_z - C_xC_yG_z\right)E_y^{n-1} + \\
\left(A_xA_yB_z - B_zC_xC_y - A_yC_zG_x + C_yF_zG_x + C_xC_zG_y - A_xF_zG_y\right)E_z^{n-1} + \\
A_yC_zh_x - C_yF_zh_x - C_xC_zh_y + A_xF_zh_y - A_xA_yh_z + C_xC_yh_z - \\
A_yC_zI_x + C_yF_zI_x + C_xC_zI_y - A_xF_xI_y + A_xA_yI_z - C_xC_yI_z
\end{array}\right\} \quad \text{(A.25 c)}$$

Spatial Formulation of Faraday's Law

For example of Eq. (A.25 a), the terms of E_y^{n-1} and E_z^{n-1} are included, however, these electric fields do not exist where E_x exists as shown in Fig. A.1 (a). For preventing this inconvenience, some spatial average has been made to E_y^{n-1} and E_z^{n-1} as

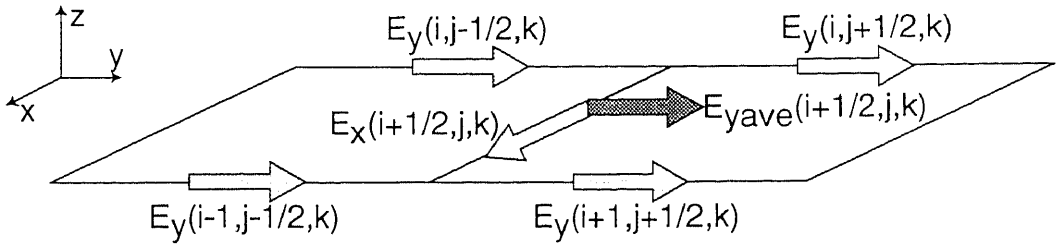

Figure A.2 Arrangement of the each component of the electric fields

$$E_{yave}^{n-1}(i+1/2,j,k)=\frac{1}{4}\begin{Bmatrix}E_y^{n-1}(i,j-1/2,k)+E_y^{n-1}(i,j+1/2,k)\\+E_y^{n-1}(i+1,j-1/2,k)+E_y^{n-1}(i+1,j+1/2,k)\end{Bmatrix} \quad \text{(A.26 a)}$$

$$E_{zave}^{n-1}(i+1/2,j,k)=\frac{1}{4}\begin{Bmatrix}E_z^{n-1}(i,j,k-1/2)+E_z^{n-1}(i,j,k+1/2)\\+E_z^{n-1}(i,+1j,k-1/2)+E_z^{n-1}(i+1,j,k+1/2)\end{Bmatrix} \quad \text{(A.26 b)}$$

Here, the coordinates of the left hand of Eq. (A.26) correspond to that of E_x, and those of the right hand of Eq. (A.26) denote the coordinates where the E_y or E_z exist as shown in Fig. A.2.

And the terms of h are also averaged by the same way as,

$$h_{xave}^{n-1/2}(i+1/2,j,k)$$
$$=\frac{\Delta t}{\varepsilon_0}\begin{bmatrix}\frac{1}{\Delta y}\left\{H_z^{n-1/2}(i+1/2,j+1/2,k)-H_z^{n-1/2}(i+1/2,j-1/2,k)\right\}\\-\frac{1}{\Delta z}\left\{H_y^{n-1/2}(i+1/2,j,k+1/2)+H_y^{n-1/2}(i+1/2,j,k-1/2)\right\}\end{bmatrix} \quad \text{(A.26 c)}$$

$$h_{yave}^{n-1/2}(i+1/2,j,k)$$
$$=\frac{\Delta t}{4\varepsilon_0}\begin{bmatrix}\frac{1}{\Delta z}\begin{Bmatrix}H_x^{n-1/2}(i+1,j-1/2,k+1/2)+H_x^{n-1/2}(i,j-1/2,k+1/2)\\+H_x^{n-1/2}(i+1,j+1/2,k+1/2)+H_x^{n-1/2}(i,j+1/2,k+1/2)\\-H_x^{n-1/2}(i+1,j-1/2,k-1/2)+H_x^{n-1/2}(i,j-1/2,k-1/2)\\+H_x^{n-1/2}(i+1,j+1/2,k-1/2)+H_x^{n-1/2}(i,j+1/2,k-1/2)\end{Bmatrix}\\-\frac{1}{\Delta x}\begin{Bmatrix}H_z^{n-1/2}(i+3/2,j-1/2,k)+H_z^{n-1/2}(i+3/2,j+1/2,k)\\-H_z^{n-1/2}(i-1/2\,j-1/2,k)-H_z^{n-1/2}(i-1/2\,j+1/2,k)\end{Bmatrix}\end{bmatrix} \quad \text{(A.26 d)}$$

$$h_{zave}^{n-1/2}(i+1/2,j,k)$$

$$=\frac{\Delta t}{4\varepsilon_0}\left[\begin{array}{l}\dfrac{1}{\Delta x}\left\{\begin{array}{l}H_y^{n-1/2}(i+3/2,j,k+1/2)+H_y^{n-1/2}(i+3/2,j,k-1/2)\\-H_y^{n-1/2}(i-1/2,j,k+1/2)-H_y^{n-1/2}(i-1/2,j,k-1/2)\end{array}\right\}\\-\dfrac{1}{\Delta y}\left\{\begin{array}{l}H_x^{n-1/2}(i,j+1/2,k+1/2)+H_x^{n-1/2}(i+1,j+1/2,k+1/2)\\+H_x^{n-1/2}(i,j+1/2,k-1/2)+H_x^{n-1/2}(i+1,j+1/2,k-1/2)\\-H_x^{n-1/2}(i,j-1/2,k+1/2)-H_x^{n-1/2}(i+1,j-1/2,k+1/2)\\-H_x^{n-1/2}(i,j-1/2,k-1/2)-H_x^{n-1/2}(i+1,j-1/2,k-1/2)\end{array}\right\}\end{array}\right] \quad \text{(A.26 e)}$$

The terms of E_x^{n-1}, E_z^{n-1}, h_x, h_y and h_z in Eq. (A.25 b) are also averaged spatially as,

$$E_{xave}^{n-1}(i,j+1/2,k)=\frac{1}{4}\left\{\begin{array}{l}E_x^{n-1}(i-1/2,j,k)+E_x^{n-1}(i+1/2,j,k)\\+E_x^{n-1}(i-1/2,j+1,k)+E_x^{n-1}(i+1/2,j+1,k)\end{array}\right\} \quad \text{(A.27 a)}$$

$$E_{zave}^{n-1}(i,j+1/2,k)=\frac{1}{4}\left\{\begin{array}{l}E_z^{n-1}(i,j,k-1/2)+E_z^{n-1}(i,j,k+1/2)\\+E_z^{n-1}(i,j+1,k-1/2)+E_z^{n-1}(i,j+1,k+1/2)\end{array}\right\} \quad \text{(A.27 b)}$$

$$h_{xave}^{n-1/2}(i,j+1/2,k)$$

$$=\frac{\Delta t}{4\varepsilon_0}\left[\begin{array}{l}\dfrac{1}{\Delta y}\left\{\begin{array}{l}H_z^{n-1/2}(i-1/2,j+3/2,k)+H_z^{n-1/2}(i+1/2,j+3/2,k)\\-H_z^{n-1/2}(i-1/2\,j-1/2,k)-H_z^{n-1/2}(i+1/2\,j-1/2,k)\end{array}\right\}\\-\dfrac{1}{\Delta z}\left\{\begin{array}{l}H_y^{n-1/2}(i-1/2,j,k+1/2)+H_y^{n-1/2}(i+1/2,j,k+1/2)\\+H_y^{n-1/2}(i-1/2,j+1,k+1/2)\\+H_y^{n-1/2}(i+1/2,j+1,k+1/2)\\-H_y^{n-1/2}(i-1/2,j,k-1/2)\\-H_y^{n-1/2}(i+1/2,j,k-1/2)\\-H_y^{n-1/2}(i-1/2,j+1,k-1/2)\\-H_y^{n-1/2}(i+1/2,j+1,k-1/2)\end{array}\right\}\end{array}\right] \quad \text{(A.27 c)}$$

$$h_{yave}^{n-1/2}(i,j+1/2,k)$$

$$=\frac{\Delta t}{\varepsilon_0}\left[\begin{array}{l}\dfrac{1}{\Delta z}\left\{H_x^{n-1/2}(i,j+1/2,k+1/2)-H_x^{n-1/2}(i,j+1/2,k-1/2)\right\}\\-\dfrac{1}{\Delta x}\left\{H_z^{n-1/2}(i+1/2\,j+1/2,k)-H_z^{n-1/2}(i-1/2\,j+1/2,k)\right\}\end{array}\right] \quad \text{(A.27 d)}$$

$$h_{zave}^{n-1/2}(i,j+1/2,k)$$

$$= \frac{\Delta t}{4\varepsilon_0}\left[\begin{array}{l} \frac{1}{\Delta x}\left\{\begin{array}{l} H_y^{n-1/2}(i+1/2,j,k-1/2)+H_y^{n-1/2}(i+1/2,j,k+1/2) \\ +H_y^{n-1/2}(i+1/2,j+1,k-1/2) \\ +H_y^{n-1/2}(i+1/2,j+1,k+1/2) \\ -H_y^{n-1/2}(i-1/2,j,k-1/2)-H_y^{n-1/2}(i-1/2,j,k+1/2) \\ -H_y^{n-1/2}(i-1/2,j+1,k-1/2) \\ -H_y^{n-1/2}(i-1/2,j+1,k+1/2) \end{array}\right\} \\ -\frac{1}{\Delta y}\left\{\begin{array}{l} H_x^{n-1/2}(i,j+3/2,k-1/2) \\ +H_x^{n-1/2}(i+1,j+3/2,k+1/2) \\ -H_x^{n-1/2}(i,j-1/2,k-1/2) \\ -H_x^{n-1/2}(i+1,j-1/2,k+1/2) \end{array}\right\} \end{array}\right]. \qquad \text{(A.27 e)}$$

The terms of E_x^{n-1}, E_y^{n-1}, h_x, h_y and h_z in Eq. (A.25 c) are also averaged spatially as,

$$E_{xave}^{n-1}(i,j,k+1/2) = \frac{1}{4}\left\{\begin{array}{l} E_x^{n-1}(i+1/2,j,k)+E_x^{n-1}(i+1/2,j,k+1) \\ +E_x^{n-1}(i-1/2,j,k)+E_x^{n-1}(i-1/2,j,k+1) \end{array}\right\} \qquad \text{(A.28 a)}$$

$$E_{yave}^{n-1}(i,j,k+1/2) = \frac{1}{4}\left\{\begin{array}{l} E_y^{n-1}(i,j+1/2,k)+E_y^{n-1}(i,j+1/2,k+1) \\ +E_y^{n-1}(i,j-1/2,k)+E_y^{n-1}(i,j-1/2\,k+1) \end{array}\right\} \qquad \text{(A.28 b)}$$

$$h_{xave}^{n-1/2}(i,j,k+1/2)$$

$$= \frac{\Delta t}{4\varepsilon_0}\left[\begin{array}{l} \frac{1}{\Delta y}\left\{\begin{array}{l} H_z^{n-1/2}(i-1/2,j+1/2,k)+H_z^{n-1/2}(i-1/2,j+1/2,k+1) \\ +H_z^{n-1/2}(i+1/2\,j+1/2,k)+H_z^{n-1/2}(i+1/2\,j+1/2,k+1) \\ -H_z^{n-1/2}(i-1/2,j-1/2,k)-H_z^{n-1/2}(i-1/2,j-1/2,k+1) \\ -H_z^{n-1/2}(i+1/2\,j-1/2,k)-H_z^{n-1/2}(i+1/2\,j-1/2,k+1) \end{array}\right\} \\ -\frac{1}{\Delta z}\left\{\begin{array}{l} H_y^{n-1/2}(i-1/2,j,k+3/2)+H_y^{n-1/2}(i+1/2,j,k+3/2) \\ -H_y^{n-1/2}(i-1/2,j,k-1/2)+H_y^{n-1/2}(i+1/2,j,k-1/2) \end{array}\right\} \end{array}\right] \qquad \text{(A.28 c)}$$

$$h_{yave}^{n-1/2}(i,j,k+1/2)$$

$$= \frac{\Delta t}{4\varepsilon_0}\left[\begin{array}{l} \dfrac{1}{\Delta z}\left\{\begin{array}{l} H_x^{n-1/2}(i,j-1/2,k+3/2)+H_x^{n-1/2}(i,j+1/2,k+3/2) \\ -H_x^{n-1/2}(i,j-1/2,k-1/2)+H_x^{n-1/2}(i,j+1/2,k-1/2) \end{array}\right\} \\ -\dfrac{1}{\Delta x}\left\{\begin{array}{l} H_z^{n-1/2}(i+1/2\,j-1/2,k)+H_z^{n-1/2}(i+1/2\,j-1/2,k+1) \\ +H_z^{n-1/2}(i+1/2\,j+1/2,k)+H_z^{n-1/2}(i+1/2\,j+1/2,k+1) \\ -H_z^{n-1/2}(i-1/2\,j-1/2,k)-H_z^{n-1/2}(i-1/2\,j-1/2,k+1) \\ -H_z^{n-1/2}(i-1/2\,j+1/2,k)-H_z^{n-1/2}(i-1/2\,j+1/2,k+1) \end{array}\right\} \end{array}\right] \quad \text{(A.28 d)}$$

$$h_{zave}^{n-1/2}(i,j,k+1/2)$$

$$= \frac{\Delta t}{\varepsilon_0}\left[\begin{array}{l} \dfrac{1}{\Delta x}\left\{H_y^{n-1/2}(i+1/2,j,k+1/2)-H_y^{n-1/2}(i-1/2,j,k+1/2)\right\} \\ -\dfrac{1}{\Delta y}\left\{H_x^{n-1/2}(i,j+1/2,k+1/2)-H_x^{n-1/2}(i,j-1/2,k+1/2)\right\} \end{array}\right]. \quad \text{(A.28 e)}$$

Finally, spatial formulation of the Faraday's law is made by substituting these averaged electromagnetic fields into Eq. (A.25).

References

[1] G. I. Dimov *et al.*, Sov. J. Plasma. Phys. **2**, 326 (1976).

[2] T. K. Fowler *et al.*, Comments Plasma Phys. Control. Fusion **2**, 167 (1977).

[3] I. Katanuma *et al.*, Phys. Plasmas **3**, 2218 (1996).

[4] J. A. Byers, Nucl. Fusion **22**, 49 (1982).

[5] R.F. Post, Nucl. Fusion **27**, 1577 (1987).

[6] I. Katanuma, J. Plasma Fusion Res. **75**, 934 (1999).

[7] P. C. Liewer, Nucl. Fusion **25**, 543 (1985).

[8] T. Lehner *et al.*, Europhys. Lett. **8**, 759 (1989).

[9] X. L. Zou *et al.*, Plasma Phys. Contr. Fusion **33**, 903 (1991).

[10] L. G. Bruskin *et al.*, Plasma Phys. Contr. Fusion **36**, 681 (1994).

[11] X. L. Zou *et al.*, in Proc. of 20th Europ. Conf. on Contr. Fusion and Plasma phys. Lisbon Vol. III 1091 (1993).

[12] A. Mase *et al.*, Jpn. J. Appl. Phys. **34**, 1494 (1995).

[13] Y. Kogi *et al.*, Jpn. J. Appl. Phys. **36**, 587 (1997).

[14] L. Vahala *et al.*, Phys. Fluids **4**, 619 (1992).

[15] L. G. Bruskin *et al.*, Plasma Phys. Contr. Fusion **37**, 255 (1995).

[16] T. H. Stix, "Waves in Plasmas" AIP, New York.

[17] V. L. Ginzburg, "THE PROPAGATION OF ELECTROMAGNETIC WAVES IN PLASMAS", PERGAMON PRESS.

[18] J. Sheffield, "Plasma Scattering of Electromagnetic Radiation", ACADEMIC PRESS (1975).

[19] J. D. Jackson, "Classical Electrodynamics", 2nd Edition, JOHN WILEY& SONS (1975).

[20] C. M. Surko *et al.*, Phys. Fluids **23**, 2425 (1980).

[21] D. L. Brower *et al.*, Nucl. Fusion **27**, 2055 (1987).

[22] D. E. Evans *et al.*, Plasma Phys. **25**, 617 (1983).

[23] Y. Sonoda *et al.*, Plasma Phys. **25**, 1113 (1983).

[24] A. Mase *et al.*, Rev. Sci. Instrum. **61**, 1247 (1990)

[25] T. Estrada *et al.*, Rev. Sci. Instrum. **61**, 3034 (1990).

[26] T. Tokuzawa *et al.*, Jpn. J. Appl. Phys. **34**, 76 (1995).

[27] A. Mase *et al.*, Phys. Fluids **5**, 1677 (1993).

[28] A. Mase *et al.*, Rev. Sci. Instrum. **66**, 821 (1995).

[29] Y. Kiwamoto *et al.*, Phys. Plasmas **3**, 578 (1996).

[30] M . Inutake *et al.*, Phys. Rev. Lett. **65**, 3397 (1990).

[31] M. Ichimura *et al.*, Fusion Eng. Des. **26**, 251 (1995).

[32] T. Saito *et al.*, in Fusion Energy: Proceedings of the 16th International Fusion Energy Conference, Montreal (International Atomic Energy Agency, Vienna, 1997), Vol 2, P. 105.

[33] T. Cho *et al.*, Phys. Rev. **45**, 2532 (1992).

[34] K. Ishii *et al.*, Nucl. Fusion **30**, 1051 (1990).

[35] M. Shoji *et al.*, J. Phys. Soc. Jpn. **65**, 2846 (1996).

[36] F. F. Chen, "Introduction of Plasma Physics and Controlled Fusion", 2nd Edition, PLENUM PRESS (1984).

[37] B. B. Kadomtsev, "PLASMA TURBULENCE", ACADEMIC PRESS (1965).

[38] G. R. Smith, Phys. Fluids 27,1499 (1984).

[39] H. Hojo *et al.*, J. Plasma Fusion Res. **69**, 1043 (1993).

[40] M. Nakamura *et al.*, Jpn. J. Appl. Phys. **37**, 342 (1998).

[41] S. J. Camargo *et al.*, Phys. Plasmas **3**, 3912 (1996).

[42] C. W. Domier *et al.*, Rev. Sci. Instum. **66**, 399 (1995).

[43] S. Kubota *et al.*, Rev. Sci. Instrum. **70**, 1042 (1999).

[44] R. Luebbers *et al.*, IEEE Trans. Electromagn. Compat. **32**, 222 (1990).

[45] R. Luebbers *et al.*, IEEE Trans. Antennas Propag. **39**, 29 (1991).

[46] K. S. Yee, IEEE Trans. Antennas Propagat. **14**, 302 (1966).

[47] Z. P. Liao *et al.*, Trans. Boundary Trans. Anal. **27**, 1063 (1984).

[48] M. D. Bui *et al.*, IEEE Trans. Microwave Theory Tech. **39**, 1165 (1991)

[49] R. Luebbers *et al.*, IEEE Trans. Antennas Propag. **40**, 1297 (1992).

[50] A. Taflove, "Computational Electrodynamics: The Finite-Difference Time-Domain Method", Norwood, MA, Artech House (1995).

[51] D. F. Kelley *et al.*, IEEE Trans. Antennas Propag. **44**, 792 (1996).

Acknowledgments

The author would like to express his gratitude to Prof. A. Mase, his academic advisor, for significant discussion and suggestion throughout his graduate study. He wishes to thank Prof. S. Aoki at the Institute of Applied Physics and Prof. K. Yatsu, director at the Plasma Research Center, for their continuous encouragement. He also wishes to thank Prof. M. Ichimura, Prof. I. Katanuma, Prof. A. Itakura and Prof. T. Tamano for helpful advise. He is very grateful to Dr. L. G. Bruskin, Dr. S. Kubota, Dr. T. Tokuzawa and Dr. N. Oyama for fruitful discussion and suggestion. He would like to thank Ms. Y. Shima for engineering support. He also thanks Mr. M. Yokoi, Mr. M. Imamura, Mr. H. Inutake, Mr. T. Onuma, Mr. N. Goto, Mr. H. Negishi, Mr. T. Uemura, Miss. H. Matsui, Mr. K. Okui, Mr. T. Hirai, and all members of GAMMA10 group for carrying out the experiments and for helpful suggestions.

He also expresses his gratitude for the support provided by Research Fellowships of the Japan Society for the Promotion of Science for Young Scientists. This work was partly supported by a Grant-in-Aid for Scientific Research from the Japanese Ministry of Education, Science, Sports, and Culture.

Finally, he wishes to thank his parents and brother for various supports.

List of Papers

Published

Yuichiro KOGI, Atsushi MASE, Leonid G. BRUSKIN, Naoyuki OYAMA, Tokihiko TOKUZAWA, Akiyosi ITAKURA, Hitoshi HOJO and Teruo TAMANO
"Cross-Polarization Scattering from Low-Frequency Waves in a Tandem Mirror Plasma"
Japanese Journal of Applied Physics, Vol. 36, Part 2, No. 5A, pp. L587-L589 1 May 1997

Yuichiro KOGI, Atsushi MASE, Leonid G. BRUSKIN, Naoyuki OYAMA, Tokihiko TOKUZAWA, Shigeyuki KUBOTA, Akiyosi ITAKURA, Makoto ICHIMURA, Hitoshi HOJO, Teruo TAMANO and Kiyoshi YATSU
"Cross-polarization scattering from low-frequency electromagnetic waves in the GAMMA10 tandem mirror"
Review of Scientific Instruments, Vol. 70, Issue 1, pp. 991-994 January 1999

Y. Kogi, A. Mase, H. Hojo, A. Itakura, M. Ichimura, and T. Tamano
"Measurement of Cross-Polarization Scattering Using Ultrashort Pulse Microwaves"
Review of Scientific Instruments, Vol. 72, Issue 1, pp. 355-358 January 2001

MASE Atsushi, TOKUZAWA Tokihiko, BRUSKIN Leonid G., KOGI Yuichiro, KUBOTA Shigeyuki, OYAMA Naoyuki,ONUMA Tsuyoshi, GOTO Naoki, ITAKURA Akiyosi, ICHIMURA Makoto, HOJO Hitoshi, TAMANO Teruo and YATSU Kiyoshi
"Density Profile and Fluctuation Measurements Using Microwave Reflectometry"
Journal of Plasma and Fusion Reserch, Vol. 74, No. 10 (1998), pp. 1189-1200

Tokihiko TOKUZAWA, Atsushi MASE, Naoyuki OYAMA, Yuichiro KOGI, Naoki GOTO, Leonid G. BRUSKIN ,Shigeyuki KUBOTA, Akiyosi ITAKURA and Kiyoshi YATSU
"The effects of density fluctuation on density profile measurements using a broadband

frequency modulated reflectometer"

Review of Scientific Instruments, Vol. 70, Issue 1, pp. 1068-1071 January 1999

Teruo SAITO, Makoto ICHIMURA, Yasuhito KIWAMOTO, Atsushi MASE, Yoshinori TATEMATSU, Hiraku ABE ,Ken KAJIWARA, Yuichiro KOGI, Motoyuki NAKAMURA, Shigenori UMEHARA, Yasuo YOSHIMURA and Kiyoshi YATSU

"Enhanced Axial Loss of Electrons from a Tandem Mirror Induced by an Alfven Ion Cyclotron Wave"

Physical Review Letters, Vol. 82, No. 6, pp. 1169-1172 February 1999

M. Nakamura, M. Ichimura, Y. Ohta, M. Oikawa, S. Tanaka, Y. Kogi, Y. Shima, S. Saosaki, K. Kadoya, T. Kawabata, H. Kano, A. Itakura, H. Hojo, A. Mase, and K. Yatsu

"Axial Profile Measurement of Alfven Ion Cyclotron Eigenmodes"

Review of Scientific Instruments, Vol. 72, Issue 1, pp. 394-397 January 2001

To be publised

Akiyosi Itakura, Naoki Goto, Masayuki Katoh, Yuicihro Kogi, Yoriko Shima, Hitoshi Hojo, Kiyoshi Yatsu, Shigeyuki Kubota, Atsushi Mase, and Tsuyoshi Onuma

"MICROWAVE REFLECTOMETRY IN THE GAMMA!0 DEVICE"

ANS Transaction of Fusion Technology